Wavelets and Filter Banks: Novel Approaches for Real and Complex-valued Transform Designs

by

GAJBHAR SHRISHAIL SHARAD
201121016

A Thesis Submitted in Partial Fulfilment of the Requirements for the Degree of

DOCTOR OF PHILOSOPHY

in

INFORMATION AND COMMUNICATION TECHNOLOGY

to

DHIRUBHAI AMBANI INSTITUTE OF INFORMATION AND COMMUNICATION TECHNOLOGY

December, 2017

Declaration

I hereby declare that

i) the thesis comprises of my original work towards the degree of Doctor of Philosophy in Information and Communication Technology at Dhirubhai Ambani Institute of Information and Communication Technology and has not been submitted elsewhere for a degree,

ii) due acknowledgment has been made in the text to all the reference material used.

<div align="right">

_____

Gajbhar Shrishail Sharad

</div>

Certificate

This is to certify that the thesis work entitled WAVELETS AND FILTER BANKS: NOVEL APPROACHES FOR REAL AND COMPLEX-VALUED TRANSFORM DESIGNS has been carried out by GAJBHAR SHRISHAIL SHARAD for the degree of Doctor of Philosophy in Information and Communication Technology at *Dhirubhai Ambani Institute of Information and Communication Technology* under my supervision.

<div align="right">

_____

Prof. Manjunath V. Joshi
Thesis Supervisor

</div>

Acknowledgments

Finally and most of all, I would like to thank my family for their unconditional love and support. I would like to thank my grandmother Sunita who has always blessed me for my progress. I would also like to thank my uncle Satish, aunt Madhuri, brother Kedar and his wife Deepali, cousins Renuka, Revati, Satyajeet and youngest member of the family i.e., my niece Aditi. Their constant support and encouragement has been a comfort in life. I will always be indebted to my parents Sharad and Suchita and my wife Yashashri for their unswerving love, care and support. I owe them everything. Finally, I would like to express my profound reverence to my spiritual guru Shri Chandrashekhar Shivacharya Maharaj and God almighty for providing me the strength to lead on a path of obstacles.

Contents

Abstract

Processing of natural images stored as 2-D discrete signals is an inevitable task in almost all areas of image processing. In order to have the desired processing results, directional image representation can be considered as an indispensable step which is similar to what the human visual system (HVS) does. Research in the HVS has confirmed the importance of *directional selectivity* as a constituent that forms a vital role in visual information processing and its perception. Since, the directional information is often present at various spatial resolutions of an image, one has to capture multiresolution property for its *efficient* representation. The problem of designing multiresolution transform based image representations having directional selectivity has been a topic of wide interest over many years.

In this thesis, using the concepts of wavelets and filter banks, we propose several novel multiresolution transform designs that have finer directional selectivity. We have classified them accordingly, based on, whether the directional decomposition of an input image has real or complex-valued representation.

Regarding the real-valued transform representation, we present designs for three transforms with higher directionality by using additional filter bank stages in conjunction with the traditional decimated (subsampled) and undecimated (nonsubsampled) wavelet transforms. All three designs have better adaptability to the oriented features in the underlying image, since the filter bank construction enables us to design the filters with better frequency selectivity. In our next work, we propose two nonsubsampled transform designs belonging to a class of multiresolution directional filter banks. The proposed designs have simple structure but nonuniform frequency partitions which effectively model the directional frequency distribution of natural images. Also, our designs need reduced compu-

tational requirements than the nonsubsampled counterparts obtained using their original subsampled approaches. All the proposed designs are tested for image denoising application using simple thresholding method.

In the next part of the thesis, we consider design of complex-valued transforms which offer various advantages over the real-valued transforms. One can have approximate shift-invariance, higher directionality and phase information along with controllable redundancy by using complex-valued representation. In our first work here, we contribute to 1-D filter design aspect of an important complex-valued transform namely dual-tree complex wavelet transform (DTCWT). 2-D DTCWT is obtained using two trees of 2-channel perfect reconstruction filter bank (PRFB) and separable filtering approach similar to discrete wavelet transform (DWT). It offers six directions with redundancy factor of just 4. However, design of 1-D filters used in the DTCWT construction is quite involved. In this work, we propose two new approaches to design the 1-D biorthogonal wavelet filters of DTCWT having near-orthogonal filter response characteristics to get almost tight-frame dual-tree complex wavelet transform (DTCWT). The proposed approaches are based on optimization of free variables obtained through factorization of generalized halfband polynomial. Use of unconstrained optimization makes these approaches simple and computationally less taxing. Associated wavelets of the filters obtained using the proposed approaches have better analytic properties leading to improved shift invariance. Also, the wavelets have near-exact symmetry resulting in improved directional feature selectivity for the multidimensional DTCWT extensions which is verified using the image denoising application. Our next work involves design of complex wavelet transform (CWT) which has better directionality and redundancy factor than the 2-D DTCWT. This is achieved by filtering the real-valued subbands of the finer directional wavelet transform using novel complex-valued filter bank stages. Proposed CWT has twelve directional subbands with redundancy factor of just 2. Its undecimated counterpart is also discussed. The *generalized* separable implementations of the proposed transforms makes them practically tractable. Image denoising using proposed CWTs show promising results for simple subband thresholding approach. In the last work,

we propose a simple yet effective multiresolution DFB design that represents the dominant directions present in the input image adaptively. The design involves two stages, where a novel partition filter bank stage is used to obtain the adaptive directional selectivity out of the eight one-sided wedge-shaped subbands of 2-D frequency spectrum. We also design Laplacian pyramid (LP) multiresolution stage with filters having high vanishing moments and better frequency selectivity. Performance of the proposed design is tested for the pansharpening application. The experiments validate the use of proposed transform-based approach for pansharpening.

Nomenclature

Abbreviations

CDF	Biorthogonal filters proposed by Cohen, Daubechies and Feauveau
DFB	Directional Filter Bank
DWT	Discrete Wavelet Transform
FIR	Finite Impulse Response
IIR	Infinite Impulse Response
LP	Laplacian Pyramid
PR	Perfect Reconstruction
FB	Filter Bank
VM	Vanishing Moments
QMF	Quadrature Mirror Filter
nuDFB	nonuniform Directional Filter Bank
FiDWT	Finer Directional Wavelet Transform
CT	Contourlet Transform
NSCT	Nonsubsampled Contourlet Transform
JPEG	Joint Photographic Experts Group
HDTV	High Definition Television
1-D	One Dimensional
2-D	Two Dimensional
m-D	Multi Dimensional
LHBP	Lagrange Halfband Polynomial
THFB	Triplet Halfband Filter Bank

2-ch	Two Channel
PRFB	Perfect Reconstruction Filter Bank
BWF	Biorthogonal Wavelet Filters
TROV	Transformations of Variables
WT	Wavelet Transform
UWT	Undecimated Wavelet Transform
CWT	Complex Wavelet Transform
MR	Multiresolution
CSFB	Checkerboard-shaped Filter Bank
HVS	Human Visual System
BLS-GSM	Bayes Least Squares-Gaussian Scale Mixture
PSNR	Peak Signal-to-Noise Ratio
SSIM	Structural Similarity Index Measure
FSIM	Feature Similarity Index Measure
RFiDWT	Redundant Finer Directional Wavelet Transform
RUFiDWT	Redundant Undecimated Finer Directional Wavelet Transform
EFiDWT	Extrafine Directional Wavelet Transform
NSMDFB	Nonsubsampled Multiresolution Directional Filter Bank
MGT	Multiscale Geometric Transform
DTCWT	Dual Tree Complex Wavelet Transform
EFiCDWT	Extrafine Complex Directional Wavelet Transform
CDFB	Complex Direction Filter Bank
CAMDFB	Complex Adaptive Multiresolution Directional Filter Bank
GT	Ground Truth
Pan	Panchromatic Image
MS	Multispectral Image

Notations

$\mathbf{A}$	Matrices are denoted using upper case bold font
$\mathbf{a}$	Vectors are denoted using lower case bold font
a	Scalars are denoted using lower case
$\mathbf{A}^T$	The transpose of matrix
$\mathrm{diag}(m, n)$	$\begin{bmatrix} m & 0 \\ 0 & n \end{bmatrix}$
$\mathbf{I}$	A 2×2 identity matrix
$\mathbf{Q}$	A 2-D Quincunx sampling matrix
$\mathbb{Z}^2$	A 2-D integer coordinate space
$\mathbb{Z}$	Set of integer numbers
l^2	Set of all square summable sequences
$x(\mathbf{n})$	A 2-D discrete sequence such as image
$\mathbf{n}$	The pixel index vector $\mathbf{n} = [n_1, n_2]^T$
$X(\mathbf{z})$	The z-transform of $x(\mathbf{n})$
$\mathbf{z}$	The index vector in the z-domain $\mathbf{z} = [z_1, z_2]^T$
$\mathbf{z}^{\mathbf{n}}$	$z_1^{n_1} z_2^{n_2}$
$\mathbf{z}^{\mathbf{A}}$	$[\mathbf{z}^{\mathbf{c_1}}, \mathbf{z}^{\mathbf{c_2}}]$, where $\mathbf{c_1}$ and $\mathbf{c_2}$ are columns of $\mathbf{A}$
$X(\mathbf{z}^{\mathbf{M}})$	Upsampling of $x(\mathbf{n})$ using matrix $\mathbf{M}$ in z-transform domain
L_w	Length of the 1-D Kaiser window used in TROV technique
β	Shape parameter used in TROV technique
$h_i^{1D}(z)$	Analysis lowpass ($i = 0$) and highpass ($i = 1$) 1-D wavelet filters of 2-ch PRFB
$f_i^{1D}(z)$	Synthesis lowpass ($i = 0$) and highpass ($i = 1$) 1-D wavelet filters of 2-ch PRFB
$r(\mathbf{n})$	2-D ideal impulse response of the filter used in TROV technique
$H_i(\mathbf{z})$	Analysis lowpass ($i = 0$) and highpass ($i = 1$) filters designed using TROV
$F_i(\mathbf{z})$	Synthesis lowpass ($i = 0$) and highpass ($i = 1$) filters designed using TROV
$X(\omega)$	Reduced notation for $X(e^{j\omega})$ i.e., Fourier transform of $x(n)$

List of Tables

List of Figures

CHAPTER 1

Introduction and Literature Survey

Over many decades, processing of natural images stored as 2-D discrete signals has been used in various applications such as denoising, compression, feature extraction, fusion etc. Transform domain image representation has been a popular way to handle the images in such tasks. Since natural images often contain directional information at various spatial resolutions, *efficient* representation of the same is necessary while processing these images. The key features in these images correspond to *oriented geometrical structures* and their representation tool should capture their orientations. Research on human visual system also shows the importance of *directional selectivity* as a constituent which forms a vital role in visual information processing and its perception [116],[44].

Research in the field of wavelets and filter banks has provided many useful multiscale and multidirectional transform representations for feature direction selectivity in images. Initially, separable multidimensional extensions of the 1-D wavelet transforms were applied successfully [46],[59],[75]. However they suffer from shift sensitivity and poor directionality. Shift sensitivity also called as shift variance is highly undesirable and is caused by aliasing due to the downsampling operations. Shift sensitivity may cause large variations in energy distribution across the inter-scale discrete wavelet transform (DWT) coefficients for small shifts in the input image [53] leading to erratic output behavior. Also, DWT is good only at isolating the point singularities and image edges in horizontal and vertical directions only. It also suffers from poor diagonal orientation selectivity due to *subband mixing* problem i.e., image features oriented at 45° and 135° are mixed in diagonal subbands of each scale. However, *edges* are often present along

1

the smooth contours and have *arbitrary* orientations. Hence DWT fails to better capture the *smoothness along the contour*.

Study of human visual perception in the context of subband image coding suggested the use of filterbanks with diamond-shaped (nonrectangular) frequency partitions rather than rectangular partitions obtained for DWT decompositions. Pioneering and earliest contributions in this context were made by Rashid Ansari and his team in [11][10][45][50].

Efficient directional selectivity offered by the use of nonseparable filterbanks has encouraged researchers to propose various 2-D nonseparable *multiresolution directional filter bank* (MDFB) designs. These MDFB designs provide multiple *directional* and *anisotropic* basis for representing image discontinuities at various resolutions. Anisotropic bases which are the bases of different shapes and sizes offer better adaptability to the image features. Contourlet transform proposed by Do and Vetterli [29] is one such MDFB design that captures the 2-D geometrical features of the images effectively and has been used in various image processing applications. Countourlet transform is constructed by using Laplacian pyramid cascaded with the directional filter bank (DFB) to have multiscale and multidirectional representation of input images. DFBs were first introduced by Bamberger and Smith in [14] and they have been used to develop several multiscale directional transforms [28, 34, 64]. However, Bamberger's DFBs have limited directional flexibility of 2^l in their *l*-level tree-structure realization. A class of nonredundant MDFBs proposed in [71, 72] offers flexible number of directional subbands, however in this case the design of required filters is quite involved [71]. Maximal decimation in these limits their directionality and also leads to shift-variant representation unsuitable for many specific image processing applications such as denoising and enhancement [23].

Attempts have been made to achieve near shift-invariance and improved directionality using the idea of *near-analytic* transform designs such as *complex wavelet transforms* (CWTs) [37, 38, 92] with small redundancy. Salient features of these complex transform designs include *shiftability* i.e., near shift-invariance, *increased directionality* and the availability of *phase information*. We refer [92] as an excel-

lent comprehensive tutorial on CWTs. The most popular CWT is 2-D dual-tree complex wavelet transform (DTCWT) [92] having redundancy factor of 4. It is obtained using two branches of DWT referred to as primal and dual tree and outputs of these are considered as the real and imaginary parts of the complex coefficient representation of an input image. Although, DTCWT output is complex-valued, 1-D real-valued filter coefficients are used in the construction and no complex arithmetic is required which is very much advantageous. However, design of DTCWT filters is quite challenging since the filters of the two trees need to satisfy various constraints [109]. This is due to the *approximate* Hilbert pair condition that must be satisfied by the wavelet functions generated by the two trees in order to have the *near-analytic* transform representation. A generalization of 2-D DTCWT to M-band is proposed in [20]. The 2-D CWTs can also be obtained using post/pre filtering stages to the DWT [92]. In [37], Fernandes *et. al* proposed a new framework for 2-D CWT with redundancy factor of 2.67 by projecting input image to Hardy space *approximation* using 1-D quasi-analytic projection filters and two DWT stages. The 2-D CWTs, both dual-tree and projection-based can only have one lowpass and six complex directional subbands oriented at $15°, 45°, 75°, -75°$ (or $105°$), $-45°$ (or $135°$) and $-15°$ (or $165°$) only. Few complex-valued directional filter bank designs have also been reported. In [73], Nguyen and Oraintara proposed a shiftable complex directional transform by combining Laplacian pyramid and complex directional filter bank. Here in order to obtain the analyticity, dual-tree structure of real DFBs is constructed where the fan filters used in the trees are constrained to satisfy the Hilbert pair criteria and certain conditions on phase responses. In [74], the same authors addressed the implementation issues such as border artifacts and the constraints on the designed FIR filters. However these filters correspond to truncated versions of infinite impulse response (IIR) filters and the transform is approximately shift-invariant. Applications using shiftable complex directional transform are given in [123] and [122] for texture image retrieval and texture segmentation, respectively. In [80], authors proposed complex-valued steerable filterbank for texture synthesis application by utilizing the features based on local phase and energy of transform coefficients.

Although *subsampled* transform designs (real or complex-valued) need lower computational requirements, downsampling stages used in these designs lead to *suboptimal* performance in many image processing applications and hence limits their applicability. Downsampling in these transforms causes *aliasing* effect leading to large reconstruction error, reduced directional flexibility, difficulty in filter design etc. Also it is not possible to build a subsampled transform having *arbitrary* frequency partitions [61], which is a key requirement for designing a direction-adaptive transform.

In recent years, nonsubsampled multiresolution transforms have attained preference in many applications such as image denoising [23][47], enhancement [60], image fusion [25],[17], etc. due to their superior performance. The multiresolution directional filter banks (MDFBs) along with the notion of *nonsubsampledness* allow flexibility in directional feature selection [61] and one can achieve increased directionality and better frequency selectivity [23]. Efficient and fast algorithms such as "*algorithme à trous*" exist for implementing nonsubsampled designs. Decimation free operations lead to a completely *shift invariant* representation useful for many image processing operations. In [23] authors proposed nonsubsampled contourlet transform using the DFBs and Laplacian pyramid without decimation. They discuss the frame theoretic designs of the nonsubsampled pyramid and fanshaped filters used in the implementation of the transform. Other notable nonsubsampled transform designs can be found in [32, 61, 65].

The transforms discussed until now are built without considering the input image characteristics and hence are *nonadaptive* in nature. Over the past one decade, different adaptive directional lifting-based wavelet transforms have been proposed for image coding with the initial contribution from Taubman [101]. Lifting scheme was proposed by Wim Sweldens in [99] for implementing the standard DWT and since then has been used extensively due to its in place computations, perfect reconstruction and lower computational cost. In [27], Ding *et. al.* proposed adaptive directional lifting (ADL) based wavelet transform for image coding. Here, the subband decomposition is similar to the standard-lifting based wavelet implementation but the prediction step is performed in the direction of

strongest pixel correlation in contrast to the horizontal and vertical directions in the latter. Few other related lifting-based adaptive wavelet transforms in this context can be found in [19, 42, 100, 129]. In [96], a nonsubsampled directional lifting transform is proposed for image denoising where the local orientation information is obtained using Gabor filters. For various other adaptive image representations one can refer to [79] as an excellent review paper. Also, comprehensive coverage of numerous other transforms can be found in [28, 49].

1.1   Problem Statement

As discussed in the previous section, for transform-based image processing applications, shift-invariance is a desirable property along with the directional selectivity. Hence, by compromising the maximally decimation criteria which is desirable for the coding applications, flexibility can be achieved to incorporate both direction selectivity as well as shift-invariance. This provides strong motivation to build such transforms for applications such as image denoising, fusion etc.

The aim of this thesis is to design new *discrete* and *efficient* redundant representations for images with following desirable properties: multiresolution, multiple directional selectivity, near/complete shift-invariance, perfect reconstruction, sparsity, anisotropic directional bases. We investigate the problem of designing novel transforms for image representation using the following two approaches.

- **By extending the directionality of traditional separable transforms namely** *discrete wavelet transform* **(DWT) and** *undecimated wavelet transform* **(UWT) using nonseparable filtering approaches:** Plethora of literature is available for wavelet transform (WT) based image applications. Since WT is inherently fast (due to separable implementation), new designs constructed using them will also inherit the same with proper care. These new designs can be easily made adaptable to the various algorithms proposed using the WT.

- **By obtaining** *bases* **that better approximate the directional image features using nonseparable filtering based multiresolution and filter bank stages:** Although faster, WT and WT-based transforms offer *suboptimal* directional

representation since study of HVS emphasize that directional features in the images usually correspond to wedge-shaped partitions in the 2-D frequency spectrum [14]. The use of nonseparable filtering based multiresolution and filter bank stages allow such flexibility to have directional bases that are better adapted to underlying geometric image features and hence are *optimal* in this sense. They also offer better performance than separable transforms in many applications. For some specific applications, nonseparable operations are required such as High Definition Television HDTV [119].

We verify the efficacy of the proposed designs using two applications namely image denoising and fusion in which perfect reconstruction property of the image representation tool is necessary.

Proposed transform designs in this thesis are divided in two categories as:

- Real-valued Transform Designs

  1. New Finer Directional Wavelet Transforms.

  2. Novel Designs for Nonsubsampled Multiresolution Directional Filter Banks.

- Complex-valued Transform Designs

  1. Design of Almost Tight Frame Dual-Tree Complex Wavelet Transform.

  2. Design of Extrafine Complex Directional Wavelet Transform.

  3. Design of Complex Adaptive Multiresolution Directional Filter Bank.

An overview figure indicating the contributions made to the 2-D filterbank-based multiresolution transforms is shown in Fig. 1.1.

1.2   Transform Terminology

In this section, we define the common terms used in this thesis from the viewpoint of transforms in general. Figure 1.2 shows the general block diagram of the transform used in signal processing applications. The transform design consists
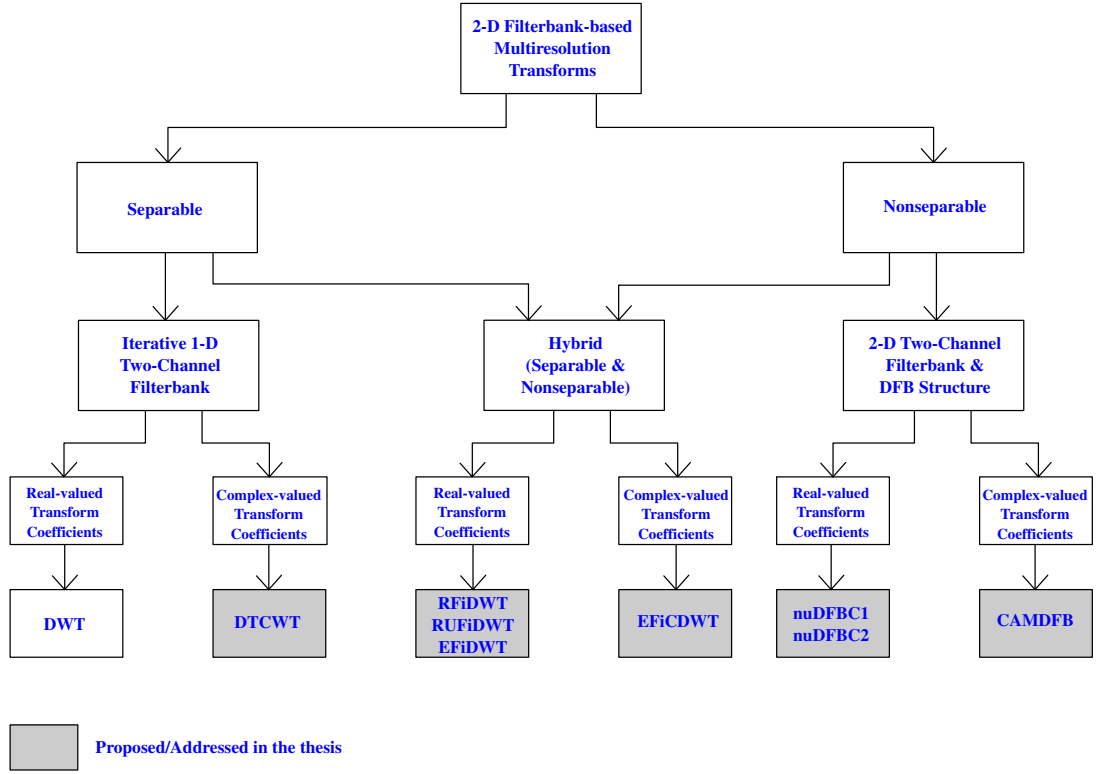
Figure 1.1: Transform designs proposed/addressed in this thesis in the context of 2-D filterbank-based multiresolution transforms.
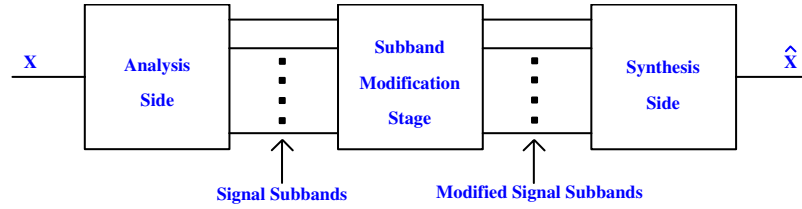
Figure 1.2: General block diagram of transform.

of two main stages namely *analysis side* and *synthesis side* used for signal decomposition and reconstruction, respectively. Using analysis side, input signal X is decomposed into subbands which are then modified accordingly as per the application at hand. Finally, the synthesis side combines these modified subbands to give an approximation to the input or reconstructed signal $\hat{X}$. Using Figure 1.2, we define the transform terminology used in this thesis as follows:

Perfect reconstruction: the transform has perfect reconstruction if and only if $\hat{X}$ represents a *delayed* version of X i.e., $\hat{X} = X$ within an allowable delay.

Critically sampled/maximally decimated/nonredundant representation: in this case, number of samples of the input signal (N_X) and total number of samples of

the signal subbands (N_{SS}) are equal i.e., $N_X = N_{SS}$.

Redundant/undecimated/nonsubsampled representation: here, $N_{SS} >> N_X$.

Multiresolution: the transform has multiresolution property if it represents the input signal at various scales or resolutions.

Directional selectivity: let X be an input image, then the transform has directional selectivity if it represents the multiscale directional image features into separate subbands.

Sparsity: the transform has sparse representation if it represents the input signal in terms of few significant transform coefficients.

Shift sensitivity/shift-variance: the transform is shift sensitive if shifts in the input signal cause dubious changes in the transform coefficients. Another definition in terms of energy can be given as, the transform is shift variant if subband energy is altered for shifts in the input signal.

Shift-invariance: the transform is shift-invariant if its coefficients are able to distinguish between input signal shifts or alternatively subband energy is unaffected for shifts in the input signal.

1.3   Thesis Outline

The thesis is organized in two parts, the first part contains two chapters in which we discuss the proposed real-valued transform designs. In the second part, we discuss the proposed complex-valued transforms.

In **Chapter 2**, we consider the problem of extending the directionality of DWT and UWT along with improved shift-invariance properties. We propose three real-valued redundant transform designs where we use pre/post nonseparable filtering stages to obtain the finer directionality. We verify the transform designs by conducting experiments on image denoising.

In order to have better approximation of the directional image features, we consider the problem of designing anisotropic directional bases using completely nonseparable filtering based approach in **Chapter 3**. We present two real-valued novel multirate tree-structure designs for a class of nonsubsampled, perfect re-

construction (PR) multiresolution directional filter banks (MDFBs). The proposed designs are simple and efficiently obtained from a combination of 2-D nonseparable filters and 2 by 2 upsampling matrices. We also discuss the design of required 2-D FIR filters. The proposed designs are finally tested for image denoising using hard-thresholding method.

In **Chapter 4**, we consider the problem of designing a prominent complex-valued alternative to replace the DWT and UWT namely dual-tree complex wavelet transform (DTCWT) which is based on approximate Hilbert transform relationship between wavelet functions of the two parallel real-valued DWT trees. We particularly propose a tight frame DTCWT generating nearly symmetric wavelet functions. In order to do this, we propose a set of biorthogonal wavelet filters used in two trees of DTCWT having near orthogonal frequency response characteristics. We propose two new approaches to obtain the same. We start by reviewing the basic preliminaries to understand the DTCWT construction and constraints required to be satisfied by the filters in both the trees. We then explain the methodologies of both the approaches. Several design examples are provided in the end with qualitative and quantitative evaluations. Finally, image noise removal performance of one the proposed filter set is evaluated by utilizing them to construct 2-D DTCWT and using subband thresholding approach.

In order to have better directionality than 2-D DTCWT with less redundancy factor, we propose a new 2-D complex wavelet transform design by applying post-filtering stages on the directional subbands of the real-valued transform in **Chapter 5**. The design scheme combines mapping of finer directional wavelet transform (FiDWT) subbands to quasi-analytic domain and partition filter bank stages to obtain the twelve directions. Both decimated and undecimated versions of the transform are discussed with necessary details. We also verify the shift-invariance of the proposed designs for image denoising application.

We consider the problem of adaptive directional selectivity in **Chapter 6**. A design for an adaptive transform which selects *noteworthy* directional features present in the input image is presented. In other words our design is adaptive to number of dominant directions of the input image. Unlike the transforms dis-

cussed in Chapter 4 and 5 which use separable wavelet transforms at their core, we use nonsubampled and nonseparable filtering stages for better flexibility in direction selectivity. We first propose our eight directional complex-valued directional filter bank (CDFB). We then discuss the procedure to estimate the dominant directions and number of required partitions needed to partition the CDFB subbands to have the adaptive directional selectivity. We consider the pansharpening or multispectral image fusion application to testify the efficacy of the proposed design. With regard to the selected application the multiresolution stage is modified and the procedure for pansharpening is given. In the end, we discuss the experimental results.

Finally, we conclude in **Chapter 7** and give directions for future research.

CHAPTER 2

New Designs of Finer Directional Wavelet Transform

2.1 Introduction

Discrete wavelet transform (DWT) has proven to be successful in applications such as image denoising under orthogonality of wavelet bases and additive white Gaussian noise (AWGN) assumption [67]. This success can be attributed to its multiscale sparse representation of signal along with the decorrelation property i.e., separating noise and the signal. However, performance of the DWT-based image denoising methods gets limited by its *shift sensitivity* and *poor directional selectivity*. Shift sensitivity is caused by inherent aliasing due to the downsampling operations in the analysis branches. Shift sensitivity causes variations in energy distribution across the inter-scale DWT coefficients [53]. Traditional separable way of obtaining 2-D DWT makes it suitable to represent image features in horizontal and vertical directions only. It also suffers from poor diagonal orientation selectivity due to *subband mixing* problem i.e., image features oriented at $45°$ and $135°$ are mixed in diagonal (HH) subband at each scale. Although DWT is a powerful tool for representing point-wise singularities in images it fails to differentiate geometric features in images oriented at arbitrary direction.

The problem of shift sensitivity/translation variance is completely removed by undecimated wavelet transform (UWT) which can be implemented efficiently using "*algorithme à trous*" [67]. Although redundancy of the transform is increased *significantly*, it minimizes pseudo-Gibbs phenomena at edges providing consider-

able improvement in PSNR as well as visual quality in case of image denoising [97]. To improve the directionality, several redundant and non-redundant multiscale geometric transforms (MGTs) have been proposed in the literature. In [14], authors represent directional image features using directional filter banks (DFBs) by dividing the 2-D frequency spectra with wedge-shaped partitions. Although DFBs do not provide multiscale representation, they have been key in widely recognized *contourlet* family [28] and *hybrid wavelets and directional filter banks (HWD)* transform in [34]. A comprehensive coverage of previously proposed MGTs is given in [28, 49].

Apart from the numerous families of MGTs using completely different basis from wavelets, traditional DWT and UWT are still attractive for image processing. Along with the fast and efficient implementations of these transforms, numerous algorithms are proposed on their basis, so the new designs using them can benefit from these algorithms [34].

The proposed work in this chapter has been motivated by the works in [23, 63, 69] to design new redundant finer directional wavelet transforms suitable for image denoising application. In [63], Lu and Do proposed the critically sampled finer directional wavelet transform (FiDWT) using an additional stage of analysis checkerboard-shaped filter bank (CSFB) on the 3 highpass subbands of DWT (LH, HL and HH) to get one lowpass and 6 highpass directional subbands ($75°$, $105°$, $15°$, $165°$, $45°$ and $135°$). In [69], aliasing phenomena inherent in FiDWT is explained and undecimated FiDWT (UFiDWT) is proposed. In [23], shift invariant nonsubsampled contourlet transform (NSCT) is proposed using undecimated, 2-channel, 2-D, nonseparable filter bank structure at its core. Such a structure is useful for constructing shift-invariant transforms providing flexibility to design frequency selective nonseparable filters with ease.

Since, NSCT is constructed using completely nonseparable multiresolution (MR) and DFB stages, it is computationally intensive. FiDWT and UFiDWT are constructed by combining the 1-D and 2-D filter bank stages. Although nonredundant, FiDWT suffers from significant aliasing due to the downsampling stages and is highly shift-variant making it unsuitable for image denoising application.

UFiDWT is simply the undecimated version of FiDWT and is obtained by using 2-channel nonsubsampled CSFB stages on the directional subbands of the undecimated wavelet transform (UWT). However, higher order checkerboard-shaped filters have to be used in this construction to reduce the inherent aliasing occurring due to their non-ideal passband characteristics. UFiDWT thus has higher computational load due to three CSFB stages with higher order filters.

In this chapter, we address these disadvantages. We propose three new transform designs having better directionality than DWT and UWT by using them with pre/post nonseparable filtering stages. The first design improves the directionality of DWT and is referred as redundant finer directional wavelet transform (RFiDWT). This design having a redundancy factor (RF) of 2 is less shift-variant than DWT and FiDWT. The transform has two wavelet coefficient images, each having one lowpass and three highpass directional subabands similar to DWT representation, hence adaptive to DWT-based algorithms. The second and third designs extend the directionality of UWT and are completely shift-invariant. The second design, redundant undecimated finer directional wavelet transform (RU-FiDWT) has redundancy factor of $2(3J + 1)$, where J is number of decomposition levels whereas the third design referred as extra finer directional wavelet transform (EFiDWT) has RF of $12J + 1$. RFiDWT and RUFiDWT have two lowpass and six directional subband representation at each scale while the EFiDWT has one lowpass and twelve directional subband representation. Traditional transforms DWT and UWT have one lowpass and three directional subband representation at each scale.

The chapter is organized as follows, design procedures for RFiDWT, RUFiDWT and EFIDWT are discussed in detail in Section 2.2. Experimental results are presented in Section 2.3 for the image denoising application, followed by conclusion in Section 2.4.

2.2 Proposed Designs of Finer Directional WT

In this section, we first explain in detail a 2-channel perfect reconstruction (PR) checkerboard-shaped filter bank (CSFB), a constituent FB stage used in the proposed designs. While, design procedures for RFiDWT, RUFiDWT and EFiDWT are provided in the next subsections.

2.2.1 2-channel PR CSFB

Figure 2.1 shows undecimated (or nonsubsampled) version of 2-channel perfect reconstruction checkerboard-shaped filter bank which is part of all three proposed designs.
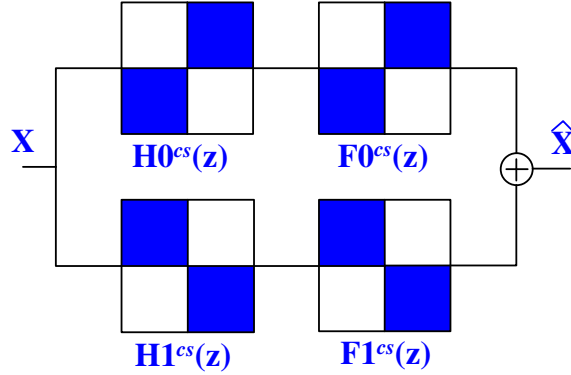
Figure 2.1: Checkerboard-shaped filter bank used in the proposed designs.

The analysis CSFB filters $H_0^{cs}(\mathbf{z})$ and $H_1^{cs}(\mathbf{z})$ split the complete input image spectra X into two diagonally quadrant passbands, giving two output images having directional features depending on passband support of the filters. By using 2-D z-transform, the input/output relations in z-transform domain can be given as,

$$\hat{X}(\mathbf{z}) = \left[\sum_{i=0}^{1} H_i^{cs}(\mathbf{z}) F_i^{cs}(\mathbf{z}) \right] X(\mathbf{z}) = T(\mathbf{z}) X(\mathbf{z}) \tag{2.1}$$

For perfect reconstruction, $T(\mathbf{z})$ should be 1 i.e., it should satisfy the *Bezout identity* [23]. Analysis and synthesis checkerboard-shaped filter responses satisfying Bezout identity are obtained from 2-D nonseparable finite impulse response (FIR) filters designed using transformation of variables (TROV) technique given

14

in [111]. It is a simple and flexible *mapping* technique equivalent to the generalized McClellan transformation that designs filter responses of different shapes and sampling lattices. The responses used here are designed with 1-D Cohen-Daubechies-Feauveau *CDF 9-7* filter. A 2-D transformation kernel is designed by truncating the 2-D ideal impulse response by multiplying it with the 2-D window obtained from 1-D Kaiser window having parameters $L_w = 7$ and $\beta = 4.5$. Figure 2.2 shows the analysis lowpass and highpass checkerboard-shaped filters designed with these parameters. The 2-D ideal impulse response for obtaining the CSFB filters is given by [111],

$$r^{cs}(\mathbf{n}) = sinc\left[\frac{n_1 \pi}{2}\right] sinc\left[\frac{n_2 \pi}{2}\right] cos\left[\frac{(n_1 + n_2)\pi}{2}\right]. \qquad (2.2)$$

(a)   (b)
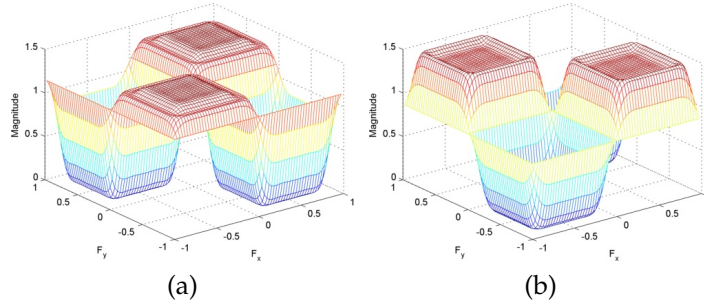
Figure 2.2: Checkerboard-shaped filter responses (a) analysis lowpass $H_0^{cs}(\mathbf{z})$ (b) analysis highpass $H_1^{cs}(\mathbf{z})$.

The 2-D impulse response coefficients of $H_i^{cs}(\mathbf{z})$ and $F_i^{cs}(\mathbf{z})$ where $i = 0, 1$ should be divided by $\sqrt{2}$ to get perfect reconstruction in filter bank structure shown in Figure 2.1.

2.2.2 Design of RFiDWT

Figure 2.3 shows, the analysis side of the proposed redundant finer directional wavelet transform (RFiDWT) with the redundancy factor of 2.

In RFiDWT, the analysis part of the CSFB is followed by critically sampled DWT hence the overall redundancy of the transform is 2. The transform has 2 lowpass subbands and 6 highpass directional subbands having orientation selectivity of $15°$, $45°$, $75°$, $105°$, $135°$ and $165°$.
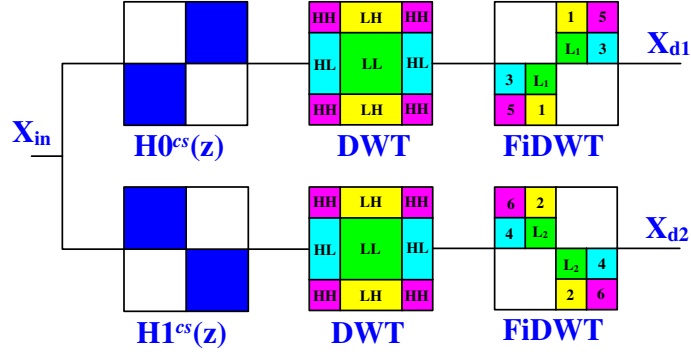
Figure 2.3: Proposed 2X redundant FiDWT design.

In our case, we consider 2-D DWT implemented using 2-channel biorthogonal PRFB with 1-D filters $H_i^{1D}(z_1)$ and $H_i^{1D}(z_2)$ ($i = 0, 1$) used for row-wise and column-wise filtering of the input, respectively. Hence, for the single level DWT decomposition, 2-D z-transforms of the resulting four subbands can be written as,

$$
\begin{aligned}
LL(\mathbf{z}) &= H_0^{1D}(z_1)H_0^{1D}(z_2) \\
LH(\mathbf{z}) &= H_0^{1D}(z_1)H_1^{1D}(z_2) \\
HL(\mathbf{z}) &= H_1^{1D}(z_1)H_0^{1D}(z_2) \\
HH(\mathbf{z}) &= H_1^{1D}(z_1)H_1^{1D}(z_2).
\end{aligned}
\tag{2.3}
$$

Thus, resultant lowpass and directional subbands of the proposed RFiDWT can be obtained as,

$$
\begin{aligned}
L_1(\mathbf{z}) &= H_0^{cs}(\mathbf{z})LL(\mathbf{z}), & L_2(\mathbf{z}) &= H_1^{cs}(\mathbf{z})LL(\mathbf{z}), \\
D_1(\mathbf{z}) &= H_0^{cs}(\mathbf{z})LH(\mathbf{z}), & D_2(\mathbf{z}) &= H_1^{cs}(\mathbf{z})LH(\mathbf{z}), \\
D_3(\mathbf{z}) &= H_0^{cs}(\mathbf{z})HL(\mathbf{z}), & D_4(\mathbf{z}) &= H_1^{cs}(\mathbf{z})HL(\mathbf{z}), \\
D_5(\mathbf{z}) &= H_0^{cs}(\mathbf{z})HH(\mathbf{z}), & D_6(\mathbf{z}) &= H_1^{cs}(\mathbf{z})HH(\mathbf{z}).
\end{aligned}
\tag{2.4}
$$

Figure 2.4(a) shows analysis side frequency responses of the resulting lowpass and directional subbands of DWT while Figure 2.4(b) shows the same for proposed RFiDWT. Figure 2.5 displays the single level decomposition of the *cameraman* image using DWT and proposed RFiDWT.

RFiDWT has standard DWT representation with each wavelet coefficient image having one lowpass subband and 3 directional highpass subbands such as
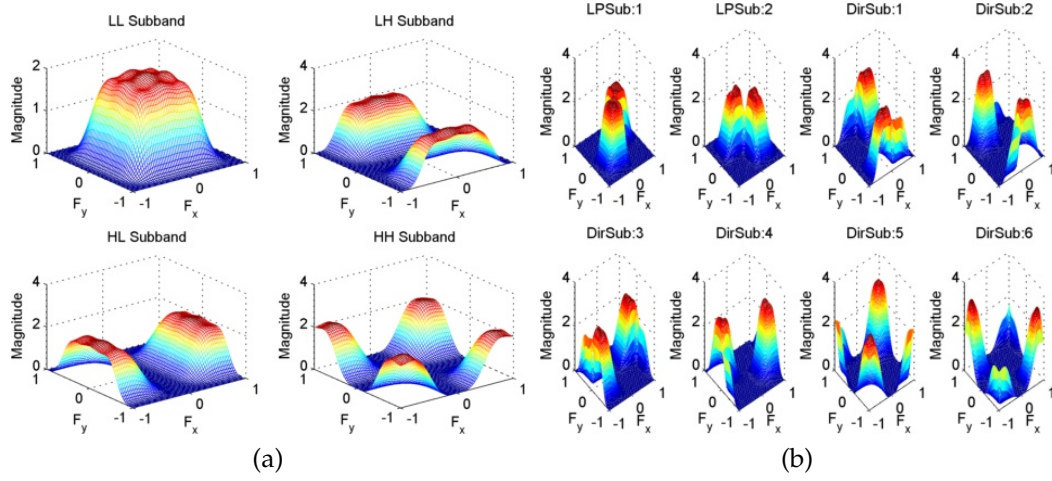
Figure 2.4: Frequency responses of (a) LL, LH, HL and HH subbands of DWT (b) two lowpass and 6 directional subbands of RFiDWT.
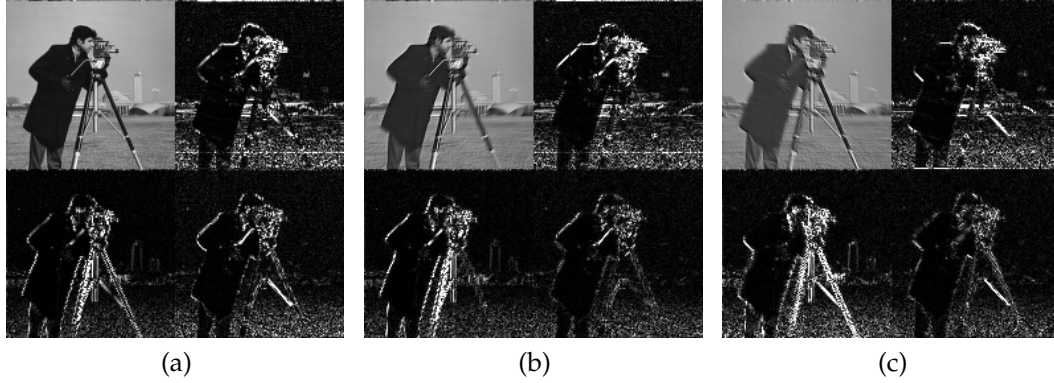
Figure 2.5: Single level decomposition of *cameraman* image using (a) DWT (b) RFiDWT: X_{d1} (c) RFiDWT: X_{d2}.

shown in Figures 2.5(b) and 2.5(c). Such representation is advantageous since many sophisticated image processing algorithms that are proposed with standard DWT can be easily adapted for the proposed transform. One such example for image denoising application using the proposed RFiDWT is given in section 2.3.2.

2.2.3 Design of RUFiDWT

Similar to the RFiDWT construction, a complete shift-invariant design can be obtained by replacing DWT in Figure 2.3 by UWT. With this, we get the redundant undecimated finer directional wavelet transform i.e., RUFiDWT. It has same directionality as in the case of RFiDWT, while each subband image size is same as that

of original image. The redundancy of this transform can be given as $2 \times (3J + 1)$, where J is the number of levels of decomposition.

Unlike UFiDWT, the proposed transform uses only one nonseparable 2-channel checkerboard-shaped filter bank stage. Here, filters can be easily designed to have better frequency selectivity without much increase in the computational cost. Also, due to availability of the *efficient* implementations for the UWT, proposed RUFiDWT has less computational requirements than UFiDWT.

2.2.4 Design of EFiDWT

Figure 2.7 shows the proposed design of an *extra* finer directional wavelet transform (EFiDWT) which has one lowpass and 12 directional subband representation at each scale. The 2-D frequency partition of the proposed EFiDWT is as shown in Figure 2.8(a). Before describing the transform design, we discuss the procedure to obtain the nonseparable filters used in its construction.

Design of required filter responses:

Proposed design only requires two types of filter responses other than checkerboard-shaped filters. They correspond to 2-D, nonseparable FIR fan filters and rectangular filters which are obtained using TROV technique [111]. The ideal impulse response for designing fan filters can be obtained by from the ideal impulse response of diamond-shaped filter $(r^{ds}(\mathbf{n}))$ as $r^{fan}(\mathbf{n}) = (-1)^{n_2} \times r^{ds}(\mathbf{n})$, where $r^{ds}(\mathbf{n}) = sinc\left[\frac{(n_1+n_2)\pi}{2}\right] sinc\left[\frac{(n_1-n_2)\pi}{2}\right]$. Ideal impulse responses to design the rectangular filters are:

$$
\begin{aligned}
r^{R1}(\mathbf{n}) &= sinc\left[\frac{n_1\pi}{2}\right] sinc\left[n_2\pi\right] \\
r^{R2}(\mathbf{n}) &= sinc\left[n_1\pi\right] sinc\left[\frac{n_2\pi}{2}\right].
\end{aligned}
\tag{2.5}
$$

The required CSFB responses can be obtained using the procedure given in section 2.2.1 or by quincunx upsampling of the fan filters [23]. Figure 3.2 shows designed analysis lowpass fan $(H_0^{fan}(\mathbf{z}))$, rectangular filter 1 $(H_0^{R1}(\mathbf{z}))$, rectangular filter 2 $(H_0^{R2}(\mathbf{z}))$ and checkerboard-shaped $(H_0^{cs}(\mathbf{z}))$ filter responses obtained using CDF

9/7 filters and 1-D Kaiser window parameters $L_w = 27$ and $\beta = 4.5$.

Figure 2.6: Magnitude responses of analysis lowpass filters designed using TROV. Starting from upper-left corner $H_0^{R1}(\mathbf{z})$, $H_0^{R2}(\mathbf{z})$, $H_0^{fan}(\mathbf{z})$ and $H_0^{cs}(\mathbf{z})$.

Transform design procedure:

We start by obtaining the nonsubsampled design of critically sampled FiDWT proposed in [63]. In order to do this, we replace DWT by UWT and append a nonubsampled 2-channel CSFB stage to the LH, HL and HH subbands to get six directional subbands. Here, to obtain *extra directionality*, we add one more stage to these directional subbands obtaining 2 extra directions from each subband. Two directional subbands obtained from the LH subband are further decomposed into two subbands by $H_i^{R1}(\mathbf{z}^{\mathbf{D_{12}}})$, while two directions from the HL subband are followed by $H_i^{R2}(\mathbf{z}^{\mathbf{D_{21}}})$. Here, $\mathbf{D_{12}} = diag(1, 2)$ and $\mathbf{D_{21}} = diag(2, 1)$ are two upsampling matrices, where $diag(x, y) = \begin{bmatrix} x & 0 \\ 0 & y \end{bmatrix}$. The separated two diagonal subbands of the UWT give two highpass directional subbands each by using 2-channel fan filters i.e, $H_i^{fan}(\mathbf{z})$, in all cases $i = 0, 1$. The synthesis stage (not shown) can be used to get back the perfectly reconstructed 2-D signal by reverse filtering these directional subbands in all stages with synthesis filters. Figure 2.8(b) shows frequency responses of the 12 highpass directional subbands of the proposed EFiDWT.
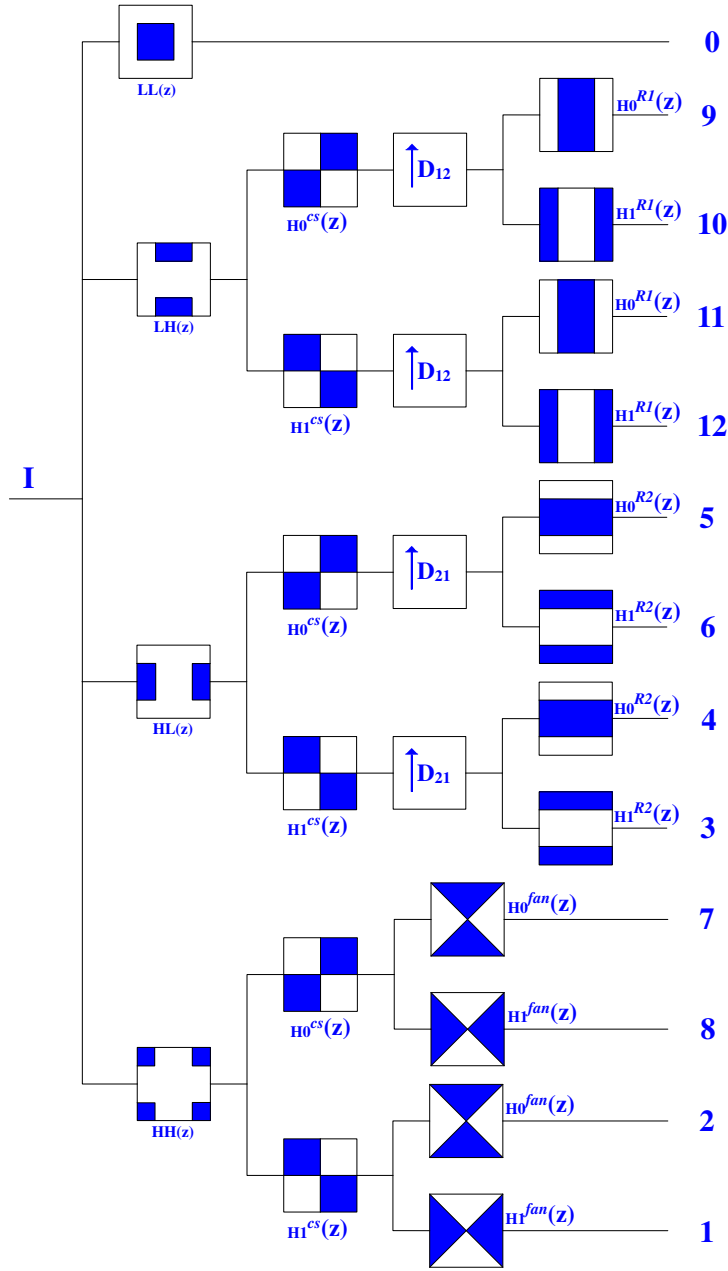
Figure 2.7: Analysis filter bank of the proposed nonsubsampled design for EFiDWT.

2.3 Application to Image Denoising

In this section, we test performance of the proposed designs for image denoising application. Note that, in all experiments, we have used the checkerboard-shaped filters designed with procedure and parameters given in section 2.2.1. The size of the analysis and synthesis lowpass CSFB filters is 57×57 and 43×43, respectively. Due to this high order of the filters and sharp frequency roll-off characteristics
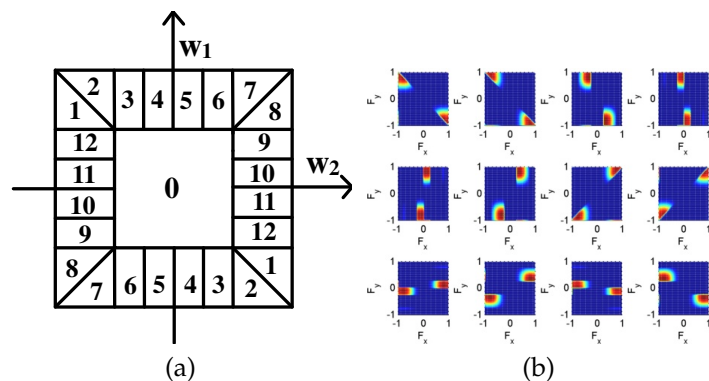
Figure 2.8: Proposed EFiDWT design (a) ideal 2-D frequency partition (b) frequency responses of the 12 directional subbands.

the aliasing phenomena is suppressed to some extent in the transforms involving downsamplers such as RFiDWT. Three levels of decomposition of all transforms is used. *Sym8* wavelet filter is used for all DWT and UWT decompositions. Additive white Gaussian noise (AWGN) of standard deviation σ is added to the original image in order to test the performance of our proposed designs on noisy images.

2.3.1 Image denoising using hard thresholding

To verify the denoising ability of the proposed design, we compare the image denoising results using *hard thresholding* method [30] using the transforms DWT, UWT, FiDWT, UFiDWT, RFiDWT, RUFiDWT and EFiDWT. A value of $T = 3\sigma$ is used for thresholding, while σ is estimated from the Donoho's robust MAD (median absolute deviation) estimator from the first scale HH subband of DWT.

Figure 2.9 shows hard thresholding results on the part of Barbara image containing oriented texture for AWGN of standard deviation $\sigma = 30$. Figure 2.10 shows Peak Signal-to-Noise Ratio (PSNR) comparison of the mentioned transforms for different noise levels.

Proposed design RFiDWT shows improvement in denoising performance over DWT, UWT and FiDWT, while EFiDWT gives the best result. It has better PSNR value and less visual artifacts in the denoised image while preserving the oriented textural features. Table 2.1 shows comparison of Peak Signal-to-Noise Ratio (PSNR), Structural Similarity Index Measure (SSIM) [131] and Feature Similarity Index Measure (FSIM) [135] values of the hard-thresholded denoised images us-
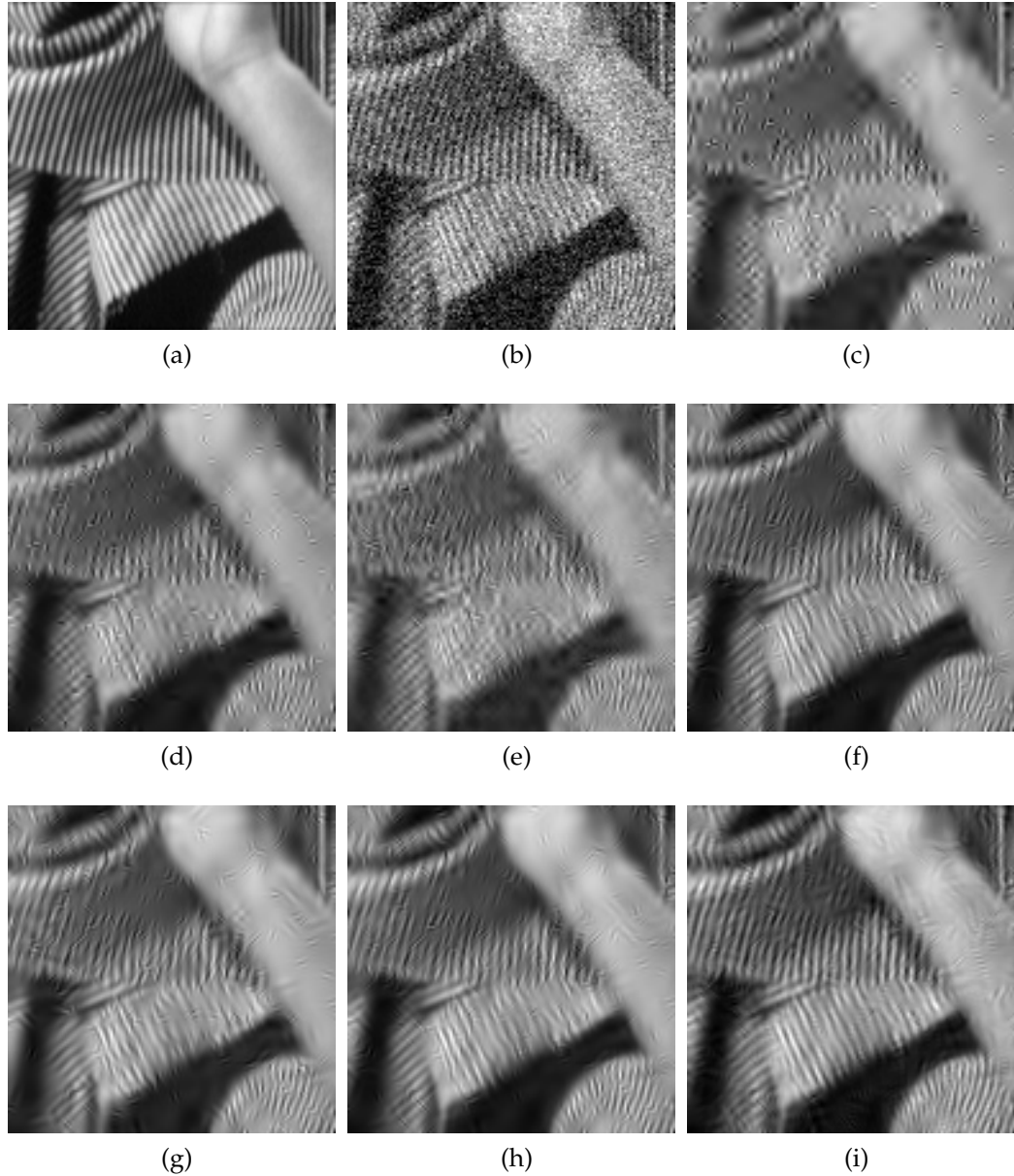
Figure 2.9: Image denoising using hard-thresholding (a) Original image (b) noisy image with $\sigma = 30$, PSNR = 18.72 dB (c) DWT, PSNR = 22.05 dB (d) UWT, PSNR = 23.51 dB (e) FiDWT, PSNR = 22.15 dB (f) UFiDWT, PSNR = 24.18 dB (g) proposed RFiDWT, PSNR = 23.95 dB (h) proposed RUFiDWT, PSNR = 24.67 dB. (i) proposed EFiDWT, PSNR = 25.85 dB

ing mentioned transforms on two widely used images. For both of the images, proposed designs maintain PSNR improvement while preserving geometrical features from the original image as evident from the better SSIM and FSIM values. From Figures 2.9, 2.10 and Table 2.1, it is validated that, increased *redundancy*, *directionality* and *frequency selectivity* of the filters in the transform designs leads to
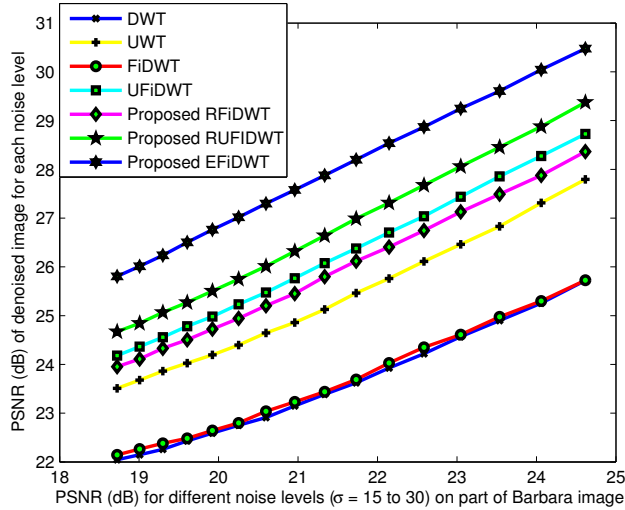
Figure 2.10: PSNR (dB) comparison of mentioned transforms under different noisy levels on the image shown in 2.9(a).

improvement in image denoising performance in terms of PSNR as well as visual quality.

2.3.2 Image denoising using RFiDWT and BLS-GSM

As stated in section 2.2.2, we apply the proposed RFiDWT with sophisticated wavelet-based image denoising algorithm namely Bayes least squares-Gaussian scale mixture (BLS-GSM) to verify its *efficacy*. BLS-GSM [81] is a state-of-the-art wavelet-based image denoising technique. MATLAB code for the same is available on authors website (*decsai.ugr.es/javier/denoise*), providing functionality to use different wavelets in orthogonal, undecimated and fully steerable pyramid mode. Best denoising results are obtained with the fully steerable pyramid which has 8 directions with redundancy factor of 18.6. In our case, we have used this method in orthogonal decomposition mode separately on the two RFiDWT transformed images (e.g., Figures 2.5(b) and 2.5(c)). Figure 2.11 shows comparison between denoised images using fully steerable pyramid and RFiDWT using BLS-GSM denoising method. It is clear that, the proposed RFiDWT has slightly better results than full steerable pyramids using BLS-GSM for textural part of the image, due to better frequency selectivity of the filters. The lines on the cloth are more clearly visible in proposed approach when compared to the other method. The direc-

Table 2.1: PSNR/SSIM/FSIM comparison of image denoising performance of mentioned transforms using hard thresholding method

σ	10			30			50		
Input PSNR/SSIM/FSIM	28.13	0.72	0.96	18.59	0.35	0.81	14.15	0.21	0.70
Transform	Barbara 512×512								
DWT	29.83	0.86	0.96	23.97	0.65	0.89	21.81	0.54	0.85
UWT	31.96	0.90	0.98	25.47	0.71	0.92	22.92	0.58	0.88
FiDWT [63]	29.71	0.85	0.95	24.34	0.65	0.88	22.00	0.53	0.84
UFiDWT [69]	32.63	0.91	0.98	26.40	0.74	0.93	23.35	0.59	0.89
Proposed RFiDWT	32.19	0.90	0.97	26.03	0.72	0.92	23.10	0.58	0.87
Proposed RUFiDWT	33.01	0.92	0.98	26.81	0.76	0.93	23.79	0.62	0.89
Proposed EFiDWT	**33.52**	**0.92**	**0.98**	**27.26**	**0.78**	**0.93**	**24.33**	**0.65**	**0.89**
σ	10			30			50		
Input PSNR/SSIM/FSIM	28.13	0.61	0.95	18.59	0.22	0.79	14.15	0.12	0.67
Transform	Lena 512×512								
DWT	32.40	0.85	0.97	27.03	0.70	0.90	24.52	0.62	0.86
UWT	34.14	0.88	0.98	28.61	0.74	0.93	25.70	0.63	0.89
FiDWT [63]	32.00	0.84	0.96	26.79	0.67	0.89	24.33	0.57	0.85
UFiDWT [69]	34.34	0.88	0.98	28.75	0.73	0.94	25.71	0.60	0.89
Proposed RFiDWT	33.93	0.88	0.98	28.36	0.72	0.92	25.40	0.60	0.87
Proposed RUFiDWT	34.74	0.89	0.98	29.36	0.76	0.94	26.38	0.65	0.90
Proposed EFiDWT	**34.93**	**0.90**	**0.98**	**29.68**	**0.80**	**0.94**	**27.05**	**0.73**	**0.90**

tional texture features in denoised images are better preserved using RFiDWT. For an $N \times N$ image, we have numerical complexity $O(N^2)$ for RFiDWT/BLS-GSM, much less than $O(N^2 \log_2 N)$ as in the case of [81].

2.4 Conclusion

In this chapter, we have presented three redundant transform designs with enriched directionality. The proposed transforms were obtained using additional pre/post nonseparable filter bank stages to the traditional decimated and undecimated wavelet transforms. We also discussed their use for the image denoising application. All three designs have better adaptability to the oriented features in the underlying image, since the filter bank construction enables us to design the filters with better frequency selectivity, thereby maintaining denoising and visual
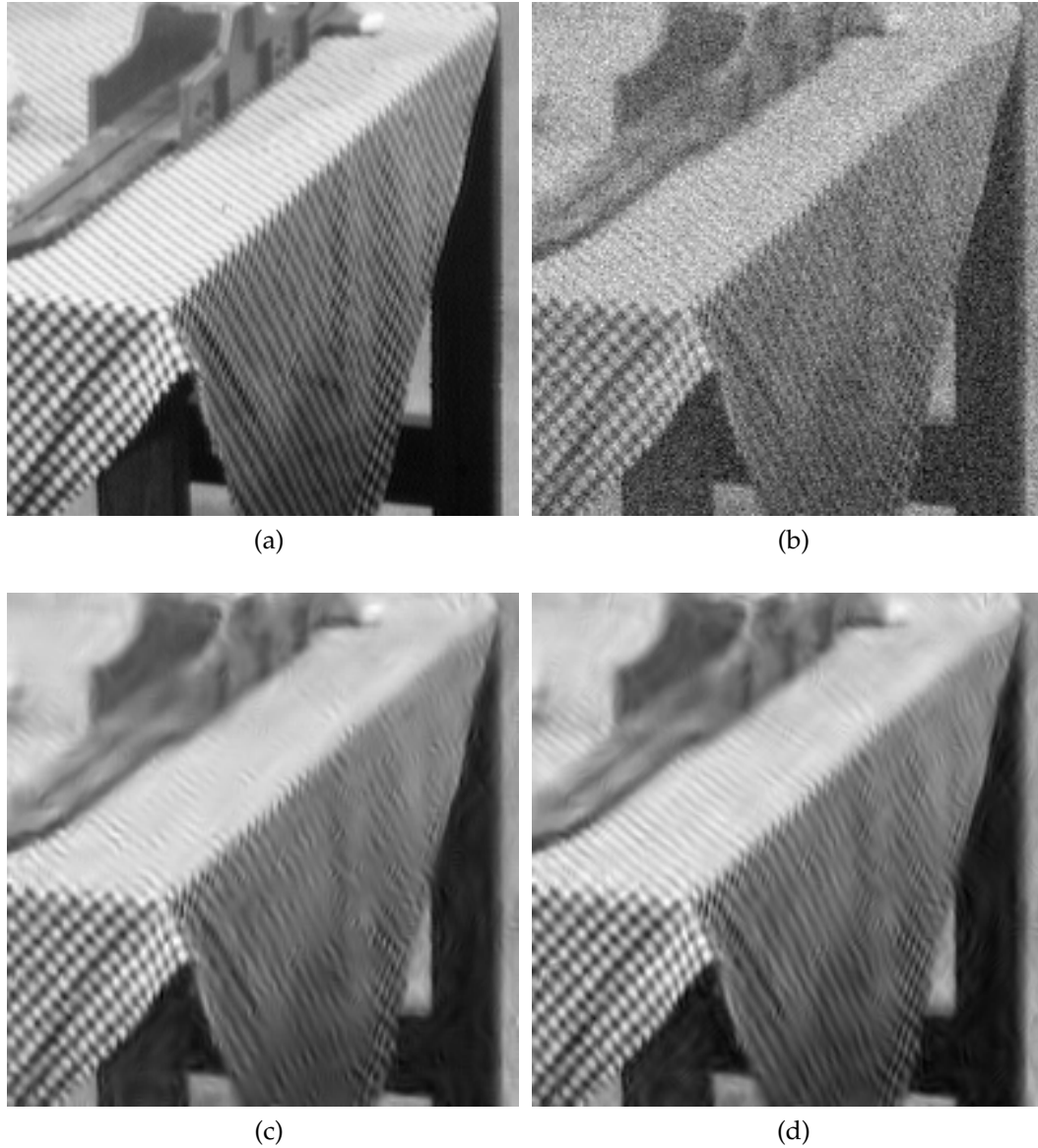
Figure 2.11: Image denoising using BLS-GSM on textural image (a) original image (b) noisy image with σ = 25, PSNR = 20.17 dB. Denoising using (c) full steerable pyramid, PSNR = 28.18 dB, (d) RFiDWT, PSNR = 28.43 dB.

artifacts suppression trade-off. Image denoising using RFiDWT with BLS-GSM, a sophisticated wavelet-based denoising algorithm, shows encouraging results for oriented textural images with much less computational cost.

CHAPTER 3

Novel Designs for Nonsubsampled Multiresolution Directional Filter Banks

In the previous chapter, we designed three new redundant transforms by extending the directionality of the traditional wavelet transforms (WTs) using additional nonseparable FB stages. Although these designs have better directionality than DWT and UWT, their directional bases are not fully *anisotropic* in nature due to rectangular frequency partition (e.g. Fig. 2.8(a)). Hence, they provide *suboptimal* approximation of the image *edges* which are basically smooth contours.

In this chapter, we obtain different types of *anisotropic* directional bases that better adapt the underlying image features using completely nonseparable filtering based approach. We propose two nonsubsampled multiresolution directional filter bank (MDFB) designs which provide *flexibility* in directional selectivity over traditional separable filtering based transforms.

We would like to mention here that we only provide the nonsubsampled designs since our work targets the proposed transforms for applications that require better shift invariance properties such as image denoising, super-resolution etc. In such cases, subsampled designs exhibit inferior performance due to the downsamplers used in the analysis side which leads to *aliasing* phenomena in the resulting directional subband outputs. Subsampled designs are useful in coding applications where the redundancy reduction is a prime concern. In this chapter, we opt to provide nonsubsampled designs that satisfy the desired output performance with simple and efficient design structures.

3.1 Introduction

In recent years, the nonsubsampled multiresolution transforms having enriched directional representations have attained unprecedented preference in specific applications such as image denoising, enhancement due to their superior performance [23, 47, 60]. The multiresolution directional filter banks (MDFBs) along with the notion of *nonsubsampled* design allows extra flexibility for directional feature selection such as transforms having arbitrary frequency partitioning [61]. Using nonsubsampled MDFBs one can achieve increased directionality and better frequency selectivity [23]. The efficient and fast algorithms such as "*algorithme à trous*" exist for their implementation. Decimation free operations lead to a completely *shift invariant* representation useful in many image processing operations.

In [23] authors proposed nonsubsampled contourlet transform (NSCT) using the decimation-free versions of Laplacian-like pyramid decomposition and DFB scheme by Bamberger and Smith [14]. Other notable nonsubsampled transform designs are Shearlet transform [32] which has less computational cost than the NSCT. Both Shearlet and nonsubsampled contourlet transforms have 2-D frequency partitions with *uniform* partition of directional subbands. However, the directional frequency distribution of natural images require *nonuniform* frequency partitions [61] for their efficient representation.

Motivated by the above works, in this chapter, we propose two nonsubampled multiresolution directional filter bank (NSMDFB) designs having fixed nonuniform 2-D frequency partitions with six directional subbands. The rest of the chapter is organized as follows, proposed transform designs are explained in detail in Section 3.2 while denoising capability of them is verified in Section 3.3 using simple subband thresholding method. Section 3.4 concludes the Chapter.

3.2 Proposed Nonsubsampled Designs

In this section, we give detailed description of our proposed MDFB designs with the following outline. In section 3.2.1, we start by explaining the nonuniform

2-D frequency partitions of the proposed designs and explain our approach to achieve the same. In the next section i.e., Section 3.2.2, we discuss the design of required filters of the filter banks used for obtaining the desired directional selectivity. Multiresolution (MR) stage used in both the designs is briefly explained in Section 3.2.3. Finally, proposed nonsubsampled directional filter banks (NSDFBs) are discussed in detail in Section 3.2.4. Proposed NSDFBs when combined with the MR stage finalize the proposed nonsubsampled MDFB designs.

3.2.1   2-D frequency partitions of the proposed designs

Figure 3.1 shows, the 2-D frequency partitions of the proposed nonsubsampled designs. The DFB partitions shown in figures 3.1(a) and 3.1(b) were first proposed in [71, 72] belonging to a class of maximally decimated directional filter banks referred as nonuniform directional filter banks (nuDFBs). We also follow the same naming notations referring to them as both belonging to a class of nonuniform directional filter banks, first design as nuDFBC1 and second design as nuDFBC2.
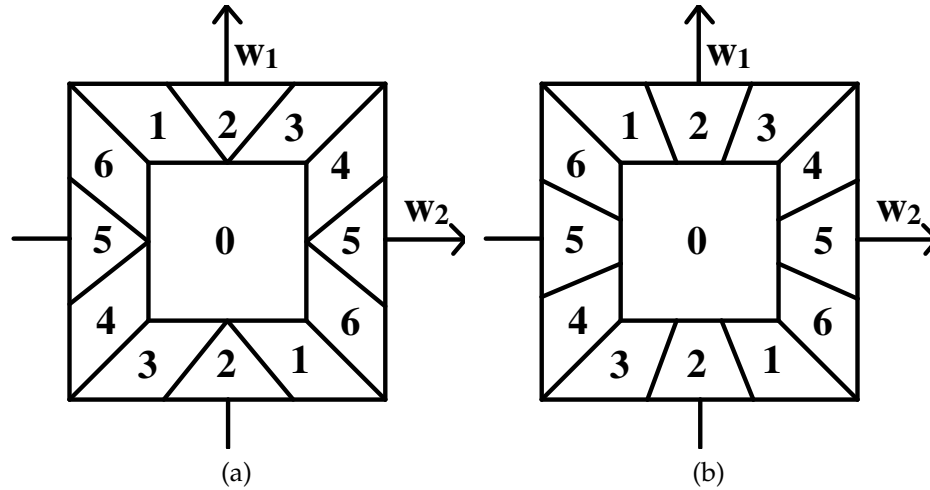
Figure 3.1: 2-D frequency partitions of the proposed designs (a) nuDFBC1 and (b) nuDFBC2.

Note that nonsubsampled designs can be obtained from their subsampled counterparts with use of suitable multirate identities. However, for the proposed nuDFBC1 and nuDFBC2 designs we have not used the filter responses used in the original critically sampled designs [72],[71]. For example, in [71] design for

partition shown in Fig. 3.1(b) require 4 different filter responses (fan filters and 3 parallelogram-shaped filters), while our designs simply need 2 different filter responses (fan filters and rectangular filters). This definitely helps in obtaining efficient separable implementations with lower computational requirements. While, the 2 parallelogram-shaped filters used in [71] cannot be constructed using simple separable implementations. We would also like to mention that the design in [71] suffers from significant aliasing due to the *frequency scrambling* effect. The resultant directional subbands are then obtained using computationally expensive direct optimization technique which also require the good initialization for better convergence. Thus the transform design as well as filter design procedures are quite involved, if we want to obtain the nonsubsampled design using the same. While our designs are simple and have lower computational requirements.

3.2.2 Design of required filter responses

The required nonseparable filter responses used in the proposed designs are same as in the EFiDWT design given in Section 2.2.4. For the sake of completeness, we repeat the same procedure. Proposed designs only require two types of filter responses. They correspond to 2-D, nonseparable FIR fan filters and rectangular filters which are obtained using TROV technique [111]. The ideal impulse response for designing fan filters can be obtained by from the ideal impulse response of diamond-shaped filter ($r^{ds}(\mathbf{n})$) as $r^{fan}(\mathbf{n}) = (-1)^{n_2} \times r^{ds}(\mathbf{n})$, where $r^{ds}(\mathbf{n}) = sinc\left[\frac{(n_1+n_2)\pi}{2}\right] sinc\left[\frac{(n_1-n_2)\pi}{2}\right]$. Ideal impulse responses to design the rectangular filters are:

$$
\begin{aligned}
r^{R1}(\mathbf{n}) &= sinc\left[\frac{n_1\pi}{2}\right] sinc\left[n_2\pi\right] \\
r^{R2}(\mathbf{n}) &= sinc\left[n_1\pi\right] sinc\left[\frac{n_2\pi}{2}\right].
\end{aligned}
\tag{3.1}
$$

The checkerboard-shaped filters are also required and they are obtained using quincunx upsampling of the fan filters [23]. Figure 3.2 shows designed analysis lowpass fan ($H_0^{fan}(\mathbf{z})$), rectangular filter 1 ($H_0^{R1}(\mathbf{z})$), rectangular filter 2 ($H_0^{R2}(\mathbf{z})$) and checkerboard-shaped ($H_0^{cs}(\mathbf{z})$) filter responses obtained using CDF 9/7 filters

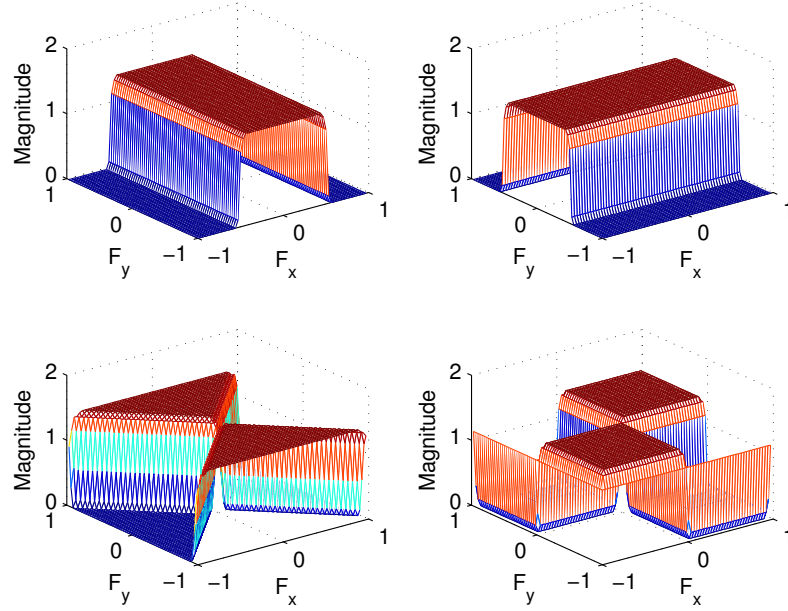and 1-D Kaiser window parameters $L_w = 27$ and $\beta = 4.5$.
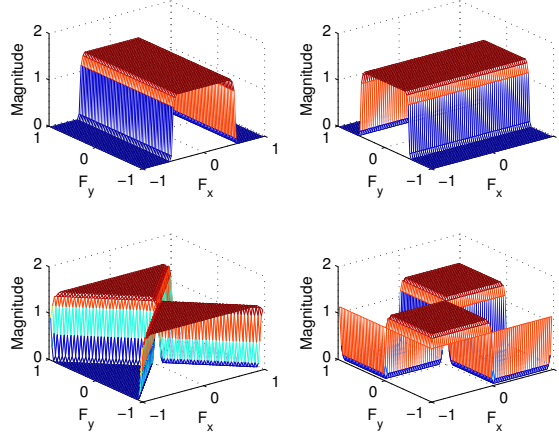
Figure 3.2: Magnitude responses of analysis lowpass filters designed using TROV. Starting from upper-left corner $H_0^{R1}(\mathbf{z})$, $H_0^{R2}(\mathbf{z})$, $H_0^{fan}(\mathbf{z})$ and $H_0^{cs}(\mathbf{z})$.

3.2.3 Multiresolution stage

We use the *nonsubsampled pyramid* (NSP) scheme proposed in the [23] for getting the multiresolution property in the proposed MDFB designs as shown in figure 3.3. For 2-D input image **I**, the NSP outputs one lowpass and J bandpass images for J level decomposition. Each bandpass image X_{in} is the input to the proposed designs i.e., nuDFBC1 and nuDFBC2 designed in the next subsection.
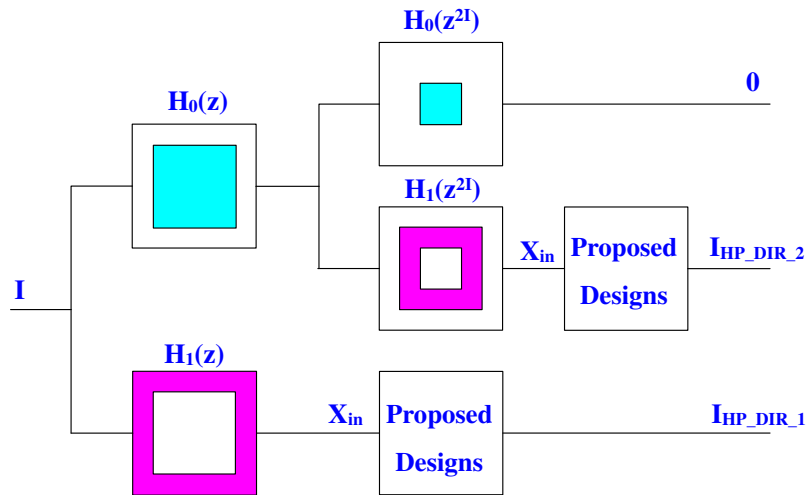
Figure 3.3: Multiresolution scheme used in the proposed MDFB designs (shown for 2 level analysis decomposition).

30

3.2.4 Design of proposed nonuniform directional filter banks

Design of nuDFBC1:

Figure 3.4 shows the analysis filter bank stages of the proposed design for nuDFBC1. The bandpass image from multiresolution or NSP stage is input to the design which gives six output directional subbands having the orientation selectivity as shown in the Fig. 3.1(a). The proposed design meets the 2-D frequency partition exactly with perfect reconstruction.
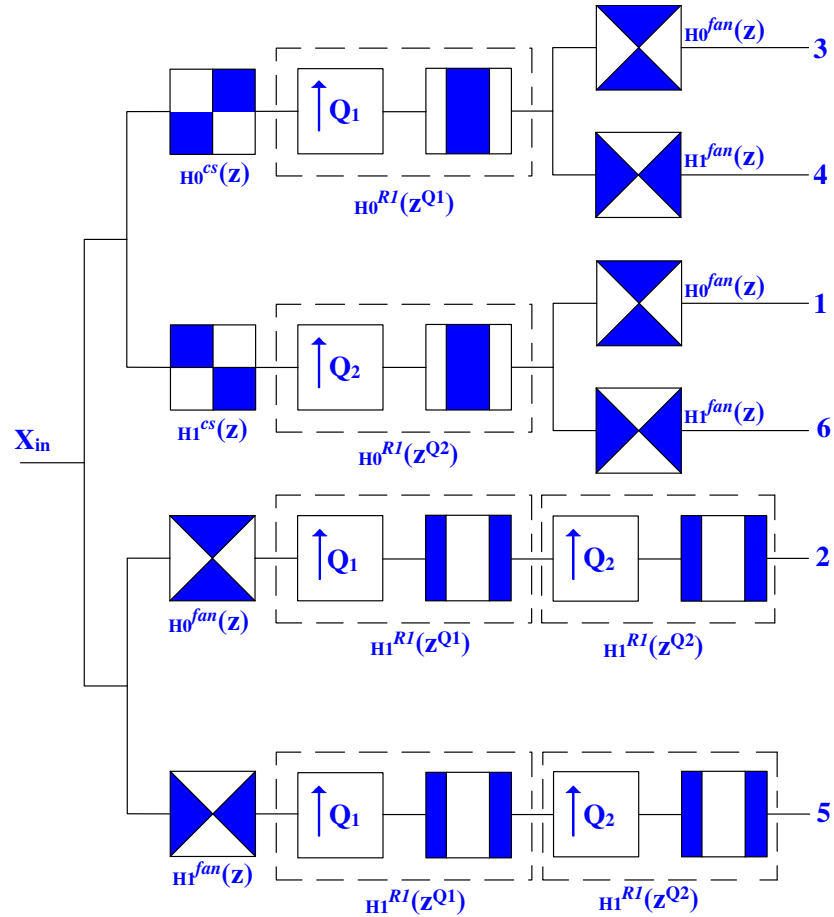
Figure 3.4: Analysis filter bank of the proposed nonsubsampled design for nuDFBC1.

In $z-$transform domain, the analysis equations for the resultant highpass di-

rectional subbands shown in Figure 3.4 can be written as

$$H^3(\mathbf{z}) = H_0^{cs}(\mathbf{z})H_0^{R1}(\mathbf{z^{Q_1}})H_0^{fan}(\mathbf{z})$$

$$H^4(\mathbf{z}) = H_0^{cs}(\mathbf{z})H_0^{R1}(\mathbf{z^{Q_1}})H_1^{fan}(\mathbf{z})$$

$$H^1(\mathbf{z}) = H_1^{cs}(\mathbf{z})H_0^{R1}(\mathbf{z^{Q_2}})H_0^{fan}(\mathbf{z})$$

$$H^6(\mathbf{z}) = H_1^{cs}(\mathbf{z})H_0^{R1}(\mathbf{z^{Q_2}})H_1^{fan}(\mathbf{z}) \qquad (3.2)$$

$$H^2(\mathbf{z}) = H_0^{fan}(\mathbf{z})H_1^{R1}(\mathbf{z^{Q_1}})H_1^{R1}(\mathbf{z^{Q_2}})$$

$$H^5(\mathbf{z}) = H_1^{fan}(\mathbf{z})H_1^{R1}(\mathbf{z^{Q_1}})H_1^{R1}(\mathbf{z^{Q_2}}).$$

Here $\mathbf{Q_1} = \mathbf{Q} = \begin{bmatrix} 1 & -1 \\ 1 & 1 \end{bmatrix}$ and $\mathbf{Q_2} = \mathbf{Q}^T$ are quincunx matrices. The synthesis filter bank stage of the proposed design (not shown) is used to reconstruct input 2-D image $\widehat{X}_{in}(\mathbf{z})$ by reverse filtering all the directional subbands using synthesis filters. The reconstructed signal $\widehat{X}_{in}(\mathbf{n})$ in z-transform domain can be obtained using the equations given below,

$$F^{34}(\mathbf{z}) = [H^3(\mathbf{z})F_0^{fan}(\mathbf{z}) + H^4(\mathbf{z})F_1^{fan}(\mathbf{z})]$$

$$F^{16}(\mathbf{z}) = [H^1(\mathbf{z})F_0^{fan}(\mathbf{z}) + H^6(\mathbf{z})F_1^{fan}(\mathbf{z})]$$

$$F^{C11}(\mathbf{z}) = [F^{34}(\mathbf{z})F_0^{R1}(\mathbf{z^{Q1}})F_0^{cs}(\mathbf{z})]$$

$$F^{C12}(\mathbf{z}) = [F^{16}(\mathbf{z})F_0^{R1}(\mathbf{z^{Q1}})F_1^{cs}(\mathbf{z})]$$

$$F^{C1}(\mathbf{z}) = [F^{C11}(\mathbf{z}) + F^{C12}(\mathbf{z})] \qquad (3.3)$$

$$F^2(\mathbf{z}) = H^2(\mathbf{z})F_1^{R1}(\mathbf{z^{Q2}})F_1^{R1}(\mathbf{z^{Q1}})F_0^{fan}(\mathbf{z})$$

$$F^5(\mathbf{z}) = H^5(\mathbf{z})F_1^{R1}(\mathbf{z^{Q2}})F_1^{R1}(\mathbf{z^{Q1}})F_0^{fan}(\mathbf{z})$$

$$F^{C2}(\mathbf{z}) = [F^2(\mathbf{z}) + F^5(\mathbf{z})]$$

$$\widehat{X}_{in}(\mathbf{z}) = [F^{C1}(\mathbf{z}) + F^{C2}(\mathbf{z})]$$

The design of nuDFBC2:

Figure 3.5 shows the analysis filter bank stages of the proposed design for nuDFBC2. The six highpass directional subbands of this design have directional selectivity similar to as shown in Figure 3.1(b). The proposed design nearly meets 2-D fre-

quency partition with perfect reconstruction.
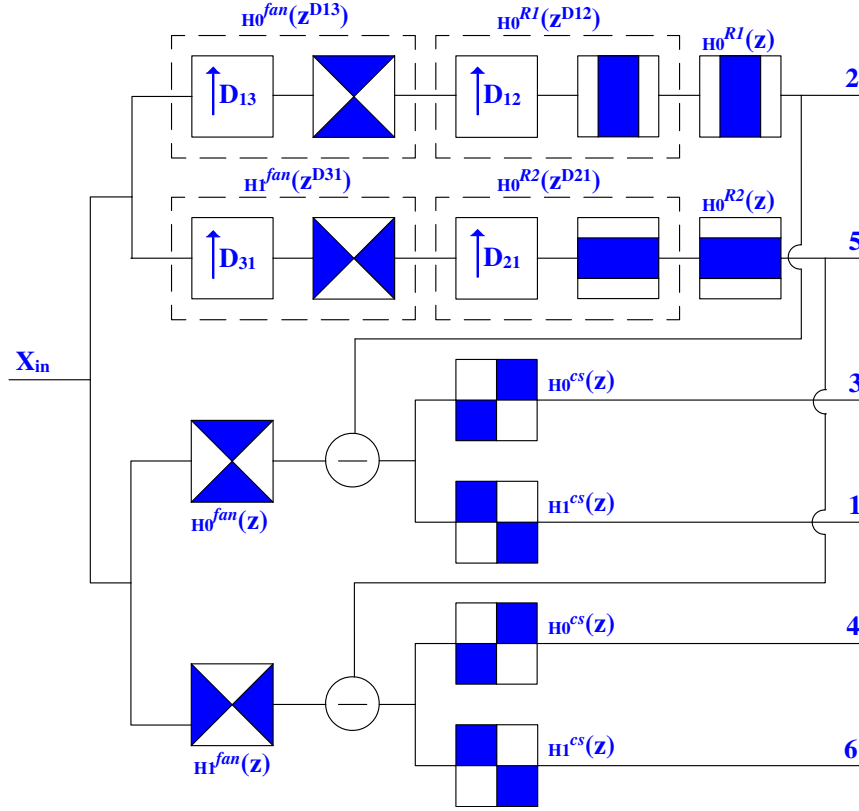
Figure 3.5: Analysis filter bank of the proposed nonsubsampled design for nuDFBC2.

Similar to nuDFBC1, the analysis equations in the $z-$transform domain for the six directional subbands of Figure 3.1(b) are given as

$$H^2(\mathbf{z}) = H_0^{fan}(\mathbf{z}^{\mathbf{D_{13}}})H_0^{R1}(\mathbf{z}^{\mathbf{D_{12}}})H_0^{R1}(\mathbf{z})$$

$$H^5(\mathbf{z}) = H_1^{fan}(\mathbf{z}^{\mathbf{D_{31}}})H_0^{R2}(\mathbf{z}^{\mathbf{D_{21}}})H_0^{R2}(\mathbf{z})$$

$$H^3(\mathbf{z}) = [H_0^{fan}(\mathbf{z}) - H^2(\mathbf{z})]H_0^{cs}(\mathbf{z})$$

$$H^1(\mathbf{z}) = [H_0^{fan}(\mathbf{z}) - H^2(\mathbf{z})]H_1^{cs}(\mathbf{z}) \qquad (3.4)$$

$$H^4(\mathbf{z}) = [H_1^{fan}(\mathbf{z}) - H^5(\mathbf{z})]H_0^{cs}(\mathbf{z})$$

$$H^6(\mathbf{z}) = [H_1^{fan}(\mathbf{z}) - H^5(\mathbf{z})]H_1^{cs}(\mathbf{z})$$

The upsampling matrices used are, $\mathbf{D_{13}} = diag(1,3)$, $\mathbf{D_{12}} = diag(1,2)$, $\mathbf{D_{31}} = diag(3,1)$ and $\mathbf{D_{21}} = diag(2,1)$. The reconstructed signal $\widehat{X}_{in}(\mathbf{n})$ in z-transform

domain can be obtained by using the following equations,

$$F^2(\mathbf{z}) = [H^2(\mathbf{z})F_0^{R1}(\mathbf{z})F_0^{R1}(\mathbf{z}^{\mathbf{D_{12}}})F_0^{fan}(\mathbf{z}^{D_{13}})]$$

$$F^5(\mathbf{z}) = [H^5(\mathbf{z})F_0^{R2}(\mathbf{z})F_0^{R2}(\mathbf{z}^{\mathbf{D_{21}}})F_1^{fan}(\mathbf{z}^{D_{31}})]$$

$$F^{31}(\mathbf{z}) = [H^3(\mathbf{z})F_0^{cs}(\mathbf{z}) + H^1(\mathbf{z})F_1^{cs}(\mathbf{z})]$$

$$F^{46}(\mathbf{z}) = [H^4(\mathbf{z})F_0^{cs}(\mathbf{z}) + H^6(\mathbf{z})F_1^{cs}(\mathbf{z})] \tag{3.5}$$

$$F^{C1}(\mathbf{z}) = [F^{31}(\mathbf{z})F_0^{fan}(\mathbf{z}) + F^{46}(\mathbf{z})F_1^{fan}(\mathbf{z})]$$

$$F^{C2}(\mathbf{z}) = [F^2(\mathbf{z}) + F^5(\mathbf{z})]$$

$$\widehat{X}_{in}(\mathbf{z}) = [F^{C1}(\mathbf{z}) + F^{C2}(\mathbf{z})]$$

The frequency responses of all the analysis highpass directional subbands of the proposed nuDFBC1 and nuDFBC2 designs are shown in Fig. 3.6(a) and 3.6(b), respectively. One can see that the directional subbands of the proposed designs have *nonuniform* and *wedge-shaped* partitions, hence their directional bases are *anisotropic* in nature which better adapt the underlying image features.

(a)   (b)
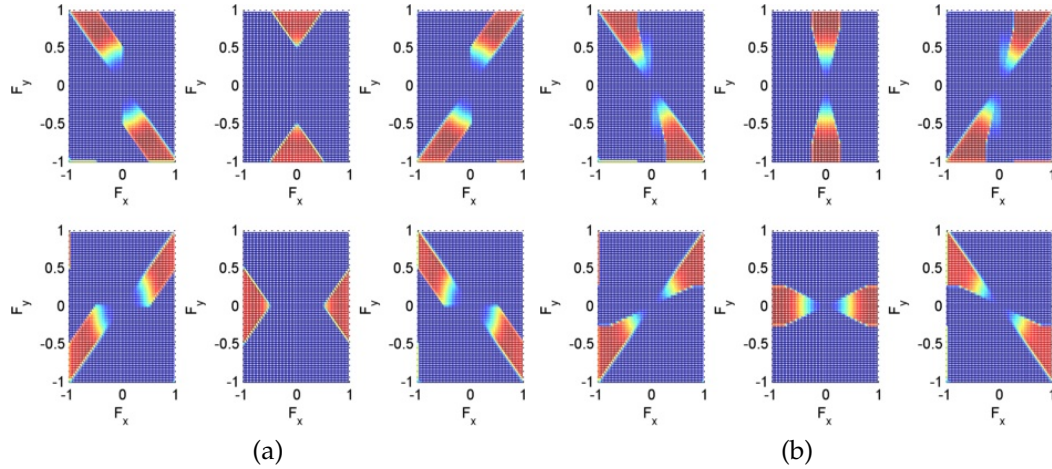
Figure 3.6: 2-D frequency partitions of the proposed designs (a) nuDFBC1 and (b) nuDFBC2.

Unlike nuDFBC1, some of the directional subbands of nuDFBC2 are interdependent. One can observe in Figure 3.5 that the directional subbands 3 and 1 are dependent on subband 2 while subbands 4 and 6 are dependent on subband 5. Here, filters of the 2-channel checkerboard-shaped filter banks used are required to have higher order for obtaining better frequency roll-off characteristics of the

filters. This is required to reduce the *residual* high frequency content which may arise after the subtraction (see equation 3.4) considering the non-ideal passband characteristics of the filters.

The proposed MDFBs can be designed to have lower computational cost by using the separable implementations of the filters used in their NSDFB stages. Both, fan-shaped as well as checkerboard-shaped filters designed using transformations of variables (TROV) technique can be implemented in separable manner [111]. Also, from equation 3.1, one can see that the proposed rectangular filters can be easily implemented in a separable manner.

3.3   Image Denoising Experiment

To verify the denoising ability of the proposed MDFB designs, we compare the image denoising results using *K-sigma hard thresholding* method [23] with two non-subsampled transforms namely undecimated finer directional wavelet transform (UFiDWT) [69] and NSCT [23]. We have chosen UFiDWT since we want to analyze the denoising improvements obtained over separable transform based design. Also, UFiDWT has one lowpass and six directional subband representation similar to the proposed designs. We also compare the results with NSCT which a widely acknowledged nonsubsampled MDFB design. We have used three levels of decomposition for all the transforms. For NSCT, we used 4, 8 and 16 directions in three scales (coarse to fine), while the proposed designs have 6 directions in each scale. Sym8 wavelet filter is used in undecimated wavelet transform (UWT) involved in UFiDWT construction. Additive white Gaussian noise of different standard deviations σ are added to the original image in order to test the performance of our proposed designs on noisy images.

Table 3.1 shows quantitative comparison of Peak Signal-to-Noise Ratio (PSNR), Structural Similarity Index Measure (SSIM) [131] and Feature Similarity Index Measure (FSIM) [135] values of the hard-thresholded denoised images using mentioned transforms on two widely used images *Barbara* and *Lena*. The proposed designs nuDFBC1 and nuDFBC2 perform reasonably well. They have better denois-

Table 3.1: PSNR/SSIM/FSIM comparison of image denoising performance of proposed designs using hard thresholding.

σ	10			30			50		
Input PSNR/SSIM/FSIM	28.13	0.72	0.96	18.59	0.35	0.81	14.15	0.21	0.70
Transform	**Barbara** 512×512								
UFiDWT [69]	32.63	0.91	0.98	26.40	0.74	0.93	23.35	0.59	0.89
NSCT [23]	**33.74**	**0.92**	**0.98**	**27.43**	**0.79**	**0.92**	**24.68**	**0.67**	**0.89**
Proposed nuDFBC1	32.45	0.90	0.98	26.46	0.74	0.93	23.73	0.62	0.89
Proposed nuDFBC2	32.33	0.90	0.98	26.38	0.72	0.93	23.65	0.60	0.89
σ	10			30			50		
Input PSNR/SSIM/FSIM	28.13	0.61	0.95	18.59	0.22	0.79	14.15	0.12	0.67
Transform	**Lena** 512×512								
UFiDWT [69]	34.34	0.88	0.98	28.75	0.73	0.94	25.71	0.60	0.89
NSCT [23]	**35.15**	**0.90**	**0.98**	**30.00**	**0.80**	**0.93**	**27.32**	**0.72**	**0.89**
Proposed nuDFBC1	34.40	0.89	0.98	29.42	0.80	0.94	26.80	0.70	0.90
Proposed nuDFBC2	34.29	0.88	0.98	29.36	0.77	0.94	26.72	0.67	0.90

ing performance when compared to UFiDWT for high σ values. While, they have comparable performance when compared to NSCT which performs best due to its inherent higher directionality at finer scales. Although the performance of proposed designs do not supersede to that of NSCT, the proposed designs show comparable performance but with simple filter bank structure and low computational costs. Overall performance of nuDFBC2 is slightly inferior to that of nuDFBC1 which may be attributed to the residual high frequency content as discussed in the previous section.

Figure 3.7 shows visual denoising results for a small part of Barbara image using the transforms compared in Table 3.1 i.e., UFiDWT, NSCT and proposed MDFB designs i.e., nuDFBC1 and nuDFBC2. Visually, the proposed designs show better preservation of the oriented texture than UFiDWT and perform comparably with NSCT which has much higher directionality. Both the proposed designs perform equally in terms of PSNR values, however texture preservation is evident for visual comparison. For example, vertical lines of the texture below the hand in the original image shown in Figure 3.7(a) are better reconstructed using nuDFBC2 (Figure 3.7(f)) than nuDFBC1 and NSCT shown in Figure 3.7(e) and Figure 3.7(d), respectively.
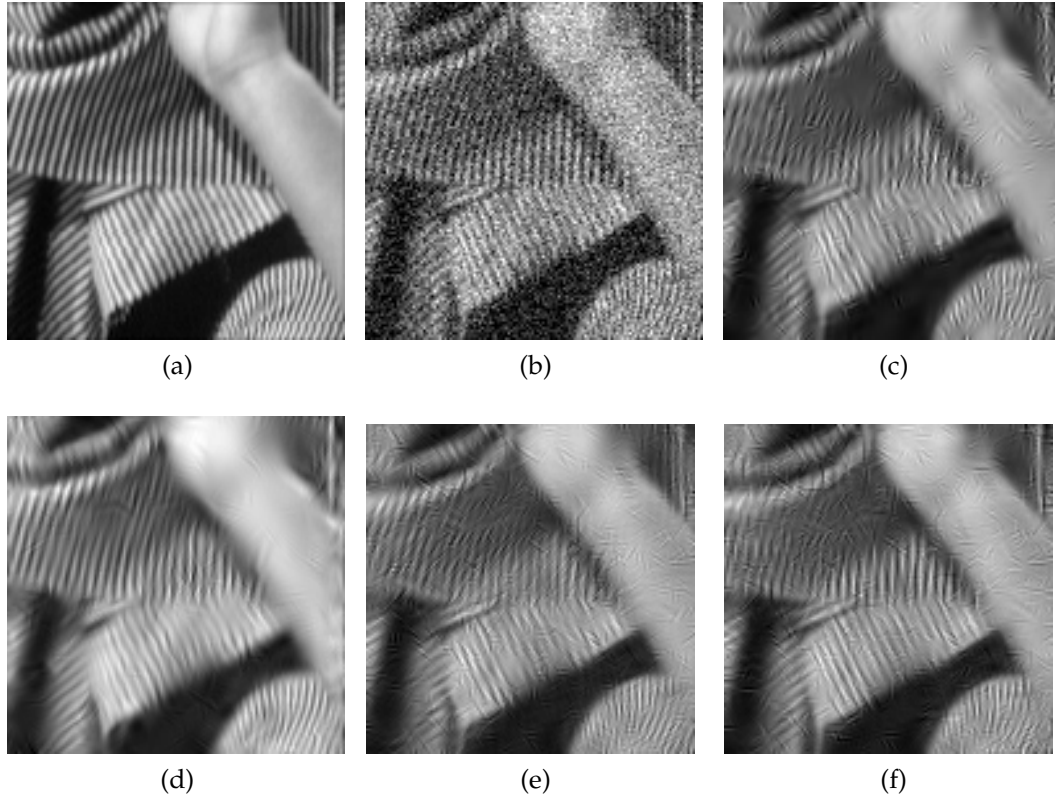
Figure 3.7: Image denoising using hard-thresholding (a) original image (b) noisy image with $\sigma = 30$, PSNR = 18.72 dB (c) UFiDWT, PSNR = 24.18 dB (d) NSCT, PSNR = 25.55 dB (e) nuDFBC1, PSNR = 24.16 dB (f) nuDFBC2, PSNR = 24.21 dB.

When comparing these results with those presented in the previous chapter (Figure 2.9 and Table 2.1), one can see that the proposed EFiDWT performs better than nuDFBC1 and nuDFBC2 due to its higher directionality while it performs comparably with NSCT.

3.4   Conclusion

In this chapter, we have presented two nonsubsampled transform designs belonging to a class of multiresolution directional banks. Both the designs have *nonuniform* 2-D frequency partitions with one lowpass and six directional subband representation. Proposed designs have simple design structure and they can have computationally efficient separable implementations. Qualitative as well as quantitative results indicate their flexibility to handle the noisy image features for image denoising application.

CHAPTER 4

Design of Almost Tight Frame Dual-Tree Complex Wavelet Transform

Many of the transforms proposed in the previous two chapters are *nonsubsampled* and have *real-valued* transform coefficient representation. Although, they have better directionality than the traditional wavelet transforms, higher redundancy may hinder their use in applications which require *output accuracy* vs. *computational complexity* trade-off. Also, due to real-valued representation, *phase information* is not available which may be beneficial in various applications such as motion estimation [66][16].

In this regard, complex-valued representation gives us a promising framework where transform redundancy as well as directionality can be improved using the idea of approximate or near *analyticity*.[1] Dual-tree complex wavelet transform (DTCWT) [92] is one such important representation. 2-D DTCWT has multiscale one lowpass and six directional image representation and has been widely used in various image processing applications. In this chapter, we contribute to the 1-D biorthogonal filter design aspect of DTCWT in order to have improved directional selectivity and almost tight-frame characteristic. By *tight-frame* transform, we mean an orthogonal transform with certain amount of redundancy [18].

---

[1]Analyticity we mean here is related to complex-valued signal representation having support in only one side of the frequency spectrum.

4.1 Introduction

In recent years, Dual-Tree Complex Wavelet Transform (DTCWT) has gained popularity as one of the important transform-domain processing tools in wide range of multimedia applications such as image [39] and video denoising [83], fusion [9], watermarking [13] to name a few. Unlike discrete wavelet transform (DWT), it offers better directionality, near-shift invariance and phase information with limited redundancy. In practice, DTCWT is implemented using two branches of DWT referred to as primal (filter bank: h) and dual (filter bank: g) tree and outputs of these are considered as the real and imaginary parts of the complex coefficient representation of an input signal. With the use of orthogonal/biorthogonal finite impulse response (FIR) filters in these trees, the transform is approximately *analytic* with a redundancy factor of just 2^m for an input of m-dimensional (m-D) signal, while the directionality is $2^{(m-1)} \times (2^m - 1)$. The idea for constructing *dual-tree complex wavelet transform* (DTCWT) was first proposed by Nick Kingsbury [51][53] and subsequently developed by Selesnick in [90][91]. We refer to [92] as an excellent tutorial paper on various aspects of DTCWT.

Although, DTCWT output representation is complex valued, real-valued filter coefficients are used in the construction and no complex arithmetic is required which is very much advantageous. However, design of such filters is quite challenging [109], since the filter coefficients need to satisfy various constraints. Selesnick [90] was the first researcher to arrive at certain conditions that must be satisfied by the DTCWT filters in order to have desired *analyticity* property. He showed that if the wavelet functions associated with the two trees of DTCWT are Hilbert transform pairs, the transform is completely analytic and shift-invariant. Since, obtaining perfect analyticity is difficult using compactly supported filters, approximate analyticity and near shift-invariance can be achieved using FIR orthogonal/biorthogonal wavelet filters [91]. In order to have these properties, filters must satisfy *perfect reconstruction* (PR), *vanishing moment* (VM) and *half-sample delay* (HSD) constraints as minimum requirements. HSD condition plays the role of coupling between two trees of DTCWT to have approximate Hilbert transform

relationship. Intuitively, the HSD requirement given by Selesnick is equivalent to Kingsbury's [53] idea of doubling the sampling rate at each scale thus largely removing the aliasing caused by downsamplers and making the transform nearly shift-invariant [92]. The concept of *generalized* HSD is used in [20] and [21] to obtain M-band extensions of orthogonal and biorthogonal DTCWT, respectively. Theoretical details about the necessary and sufficient conditions in case of orthogonal and biorthogonal DTCWT filters can be found in [133] and [134], respectively.

Traditional wavelet filter design techniques cannot be used directly to design DTCWT filters since they only consider PR and VM conditions. Considering the much needed HSD requirement, various approaches are proposed in the literature to obtain orthogonal/biorthogonal DTCWT filters [92][109]. In this chapter, we only consider the design of biorthogonal FIR filters. For various orthogonal filter design approaches, one can refer to [24, 31, 52, 54, 68, 94, 103, 104, 105, 127, 128, 136, 137, 138, 139, 140].

In [51][53], Kingsbury proposed the use of odd/even filter design approach to obtain biorthogonal wavelet filters (BWFs) based DTCWT construction. In this approach, symmetric odd-length (Type-I) and even-length (Type-II) BWFs are used in primal (first) and dual (second) tree, respectively. Here, given the filters in primal filter bank (FB), aim is to obtain the dual FB filters. In general, well known odd-length filters (such as CDF 9/7, LeGall 5/3) are used in the first tree whereas filters of the second tree are designed such that their magnitude responses are approximately equal to that of corresponding first tree filters. Here, the HSD constraint is perfectly satisfied and the filters have exact linear phase characteristics. In [91], Selesnick devised *common factor* technique capable of designing orthogonal/biorthogonal filters with prescribed number of vanishing moments (VMs). The technique uses binomial product filter factorization approach of Daubechies [26] for including vanishing moments criteria while half-sample delay constraint is approximated using maximally flat all pass filters. Due to HSD approximation, the designed filters have approximately linear phase characteristics. In this technique, both primal and dual tree filters are designed simultaneously.

Most of the BWF design techniques proposed in the literature are variants of

the above two approaches. In [36], Fernandes *et. al* modified the common factor approach by designing the all-pass filter approximation of the HSD condition by using minimax criteria instead of the maxflat approach used in [91]. Better approximation properties of the associated wavelets were obtained in this case. In [134], authors proposed an odd/even approach where constrained optimization is used to obtain the dual FB filters by minimizing the magnitude response error between filters of the two trees. In [110], Tay proposed a new class of even-length biorthogonal wavelet filters to obtain dual FB filters for the chosen primal FB filters. The filters are referred to as even triplet halfband filter bank (ETHFB) and are obtained by modifying odd-length triplet halfband filter bank of Ansari *et al* [12]. A new odd/even scheme is proposed in [95] to design BWFs of dual FB by using constrained optimization and exploiting the relationship between the HSD requirement and the vanishing moments difference of the biorthogonal lowpass filters of the two trees. Techniques for designing rational coefficient BWFs are also proposed in [3][107].

In this chapter, we propose two new approaches to design biorthogonal wavelet filters of DTCWT. Our first approach is a variant of *common factor* solution whereas the second one uses odd/even filter settings. The motivation for the proposed approaches is to design biorthogonal filters having near-orthogonal filter response characteristics that can provide a near *tight frame* DTCWT which is a l^2 norm (energy) preserving transform. Such transforms have improved noise decorrelation and are useful in image denoising application. We also require the resulting wavelet functions to have exact or near-exact symmetry which improves the directional selectivity of DTCWT [91]. This condition makes the image features such as edges to be handled without the unwanted oscillatory behavior [68]. In addition, we also desire filters giving Hilbert pairs of wavelets with improved analyticity for better shift-invariance. In order to obtain these properties, we make use of an optimization approach in the proposed techniques. We build our methods to mitigate the following problems associated with the common factor and odd/even filter design methods:

- The filters designed using common factor approach [91] have poor frequency

response since it uses maximum number of vanishing moments i.e., zeros at $z = -1$ or $\omega = \pi$ resulting in zero degrees of freedom to shape the filter response characteristics. Hence, it is desired to have filters with good frequency response characteristics to minimize the *inherent* residual amplitude distortion present in the maximally decimated filter banks used in the two trees of DTCWT.

- In the odd/even filter setting, if the magnitudes of scaling and the wavelet functions are not aligned at higher levels of decomposition (> 2), it may result in severe implications while using DTCWT with hierarchical algorithms such as hidden Markov tree model etc [53]. The use of near-orthogonal BWFs in this case curtails these effects [53].

In our first approach, we address the problem using common factor technique by designing the filters with better frequency response characteristics (near-orthogonal). In the second approach, we propose to use odd-length biorthogonal filters having near-orthogonal frequency response in the first tree and accordingly design the second tree filters to have nearly tight-frame transform. Both these approaches provide an effective way to handle the filter response characteristics of these filters which is obtained by using unconstrained optimization of free variables. Also, the proposed approaches can be modified to design the orthogonal filters by designing a halfband polynomial satisfying certain non-negativity constraints followed by the spectral factorization approach.

The chapter is organized as follows. In section 4.2, we give the background to understand the DTCWT basics and briefly describe the common factor and odd/even techniques. In section 4.3, the proposed approaches are described while section 4.4 details the design examples of both the proposed approaches along with their qualitative and quantitative measures. In section 4.5, we discuss performance of one of the proposed filter set for image denoising application. Section 4.6 concludes the chapter.

4.2 Background Review

4.2.1 DTCWT basics

Fig. 4.1 shows core structure of the DTCWT. It has two trees consisting of 2-channel filter banks that use 1-D biorthogonal wavelet filters. In Tree-1, the filters
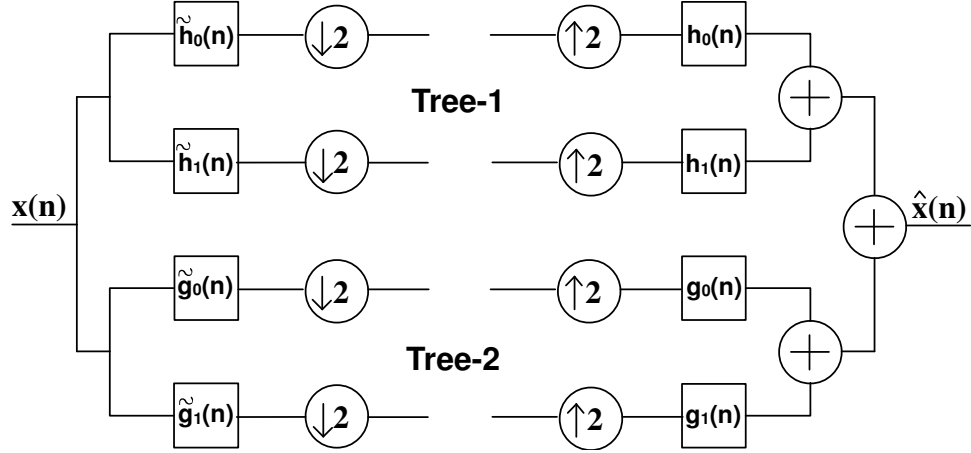
Figure 4.1: Two trees of 2-channel filter banks used in DTCWT construction

$\tilde{h}_0(n)$ and $\tilde{h}_1(n)$ represent the analysis lowpass and highpass filters, respectively. Similarly, the $h_0(n)$ and $h_1(n)$ represent the same on the synthesis side referred to as synthesis lowpass and highpass filters. They are related to each other as follows

$$\tilde{h}_1(n) = -(-1)^n h_0(n), \;\; 0 \leq n \leq N-1$$
$$h_1(n) = (-1)^n \tilde{h}_0(n), \;\; 0 \leq n \leq \tilde{N}-1.$$

(4.1)

Here, $\tilde{N}$ and N represent lengths of the filters $\tilde{h}_0(n)$ and $h_0(n)$, respectively. Similar relations hold good in the case of filters in Tree-2.

Let, $\phi_h(t)$ and $\phi_g(t)$ be the synthesis scaling functions of Tree-1 and Tree-2, respectively and $\psi_h(t)$ and $\psi_g(t)$ be their corresponding wavelet functions. Then

the two-scale equations associated with these are given as

$$\phi_h(t) = \sqrt{2}\sum_n h_0(n)\phi_h(2t-n)$$

$$\psi_h(t) = \sqrt{2}\sum_n h_1(n)\phi_h(2t-n)$$

$$\phi_g(t) = \sqrt{2}\sum_n g_0(n)\phi_g(2t-n)$$ (4.2)

$$\psi_g(t) = \sqrt{2}\sum_n g_1(n)\phi_g(2t-n).$$

In a similar way one can define analysis wavelet functions $\tilde{\psi}_h(t)$ and $\tilde{\psi}_g(t)$. In order to have approximate analyticity of DTCWT, we require that $\psi_g(t) \approx \mathcal{H}\{\psi_h(t)\}$ and $\tilde{\psi}_g(t) \approx \mathcal{H}\{\tilde{\psi}_h(t)\}$ [90][91] representing Hilbert transform pairs criteria. This indicates that the synthesis and analysis wavelet functions of Tree-2 are *approximately* Hilbert transforms of Tree-1 wavelet functions. In Fourier domain, these relations are given as

$$\Psi_g(\omega) \approx \begin{cases} -j\Psi_h(\omega), & \omega > 0 \\ j\Psi_h(\omega), & \omega < 0. \end{cases}$$ (4.3)

Similar expressions exist for $\tilde{\Psi}_g(\omega)$. Here, $\Psi_h(\omega)$, $\Psi_g(\omega)$, $\tilde{\Psi}_h(\omega)$ and $\tilde{\Psi}_g(\omega)$ represent Fourier transforms of $\psi_h(t)$, $\psi_g(t)$, $\tilde{\psi}_h(t)$ and $\tilde{\psi}_g(t)$, respectively. Since, wavelet functions depend on the scaling functions which in turn depend on the lowpass filters associated with that scaling function, the problem of designing the Hilbert transform pairs of wavelet bases reduces to designing the lowpass filters that satisfy $g_0(n) \approx h_0(n-0.5)$ which is known as *half-sample delay* (HSD) constraint [92]. In Fourier domain, this can be expressed as

$$G_0(\omega) \approx e^{-j\frac{\omega}{2}} H_0(\omega)$$ (4.4)

where, $G_0(\omega)$ and $H_0(\omega)$ are Fourier transforms of $g_0(n)$ and $h_0(n)$, respectively. One can design these filters by approximating the magnitude and phase responses

as

$$|G_0(\omega)| = |H_0(\omega)| \tag{4.5}$$

$$\angle G_0(\omega) = -\frac{\omega}{2} + \angle H_0(\omega). \tag{4.6}$$

Due to the nature of the equation (4.4), one of the two conditions given in equations (4.5) and (4.6) is satisfied *exactly* or both are approximated. Based on this, design techniques proposed in the literature for DTCWT are classified into three categories namely Half sample delay (M) (HSD(M)), HSD(P) or HSD(G) [109]. In case of HSD(M), the condition given in equation (4.5) is exactly satisfied whereas the condition on phase given in equation (4.6) is approximated. For HSD(P), the reverse is true i.e., phase condition is perfectly satisfied whereas magnitudes are approximately equal. In the case of HSD(G), both the conditions are approximately equal. The common factor and odd/even filter techniques mentioned earlier belong to the HSD(M) and HSD(P) categories, respectively. Since, our proposed techniques are based on these methods, we explain them briefly in the next subsections.

4.2.2 Common factor technique

Common factor technique [91] proposed by Selesnick uses a two stage design process to approximate the relation given in equation (4.4) and finally obtains the required filters of DTCWT shown in Fig. 4.1. In the first stage, half-sample delay constraint is approximated using Thiran's maximally flat allpass filters [112]. Perfect reconstruction and vanishing moment constraints are imposed in the second stage by considering the use of *maxflat* halfband polynomial factorization approach. Both the stages are combined to obtain the final product filter $P(z)$ to design the biorthogonal wavelet filters. Here, due to the use of product filter factorization, filters with prescribed *vanishing moments* can be easily designed. Also, we only need to design the product filters of one of the two trees i.e., either of the

following two equations (4.7) and (4.8) can be used.

$$P(z) = \tilde{H}_0(z)H_0(z) \tag{4.7}$$

$$= \tilde{G}_0(z)G_0(z). \tag{4.8}$$

Here, $\tilde{H}_0(z)$, $H_0(z)$, $\tilde{G}_0(z)$ and $G_0(z)$ are the $z-$transforms of $\tilde{h}_0(n)$, $h_0(n)$, $\tilde{g}_0(n)$ and $g_0(n)$, respectively. If the lengths of the filters $\tilde{h}_0(n)$ and $h_0(n)$ are $\tilde{N}$ and N, respectively, the filters of Tree-2 can be obtained using time-reversal relationship as

$$\tilde{g}_0(n) = \tilde{h}_0(\tilde{N} - 1 - n), \quad 0 \le n \le \tilde{N} - 1 \tag{4.9}$$

$$g_0(n) = h_0(N - 1 - n), \quad 0 \le n \le N - 1. \tag{4.10}$$

The filters $\tilde{h}_0(n)$ and $h_0(n)$ are obtained using polynomial factorization of the form $\tilde{H}_0(z) = \tilde{F}_0(z)D(z)$ and $H_0(z) = F_0(z)D(z^{-1})z^{-L}$, where $D(z)$ and $D(z^{-1})z^{-L}$ are chosen such that

$$A(z) = \frac{D(z^{-1})z^{-L}}{D(z)} = z^{-1/2}|_{z=1}. \tag{4.11}$$

which represents an all pass filter approximation of half-sample delay. Here, $D(z) \xleftrightarrow{\mathcal{Z}} d(n)$ represents a z-transform pair and L represents order of the filter $d(n)$ obtained using equation (4.12).

$$d(n+1) = d(n).\frac{(L-n)(L-n-0.5)}{(n+1)(n+1+0.5)}, \quad 0 \le n \le L-1 \tag{4.12}$$

where, $d(0) = 1$. Factors $\tilde{F}_0(z)$ and $F_0(z)$ are *maxflat* or *binomial* filters used in order to satisfy the *perfect reconstruction* and *vanishing moments* criteria and are of the form $\tilde{Q}(z)(1+z^{-1})^{\tilde{K}}$ and $Q(z)(1+z^{-1})^{K}$, respectively. The polynomials $\tilde{Q}(z)$ and $Q(z)$ are obtained by solving a set of linear equations by imposing halfband constraint on $P(z)$. Here, $\tilde{K}$ and K represent the number of VMs for $\tilde{h}_0(n)$ and $h_0(n)$, respectively. Since the filters are chosen to satisfy equations (4.9) and (4.10), the magnitude condition given in equation (4.5) is exactly satisfied, whereas the phase condition given in equation (4.6) is approximated since the order L used is finite. Ideally L should be ∞ to satisfy the equation (4.11) exactly.

4.2.3 Odd-even filter design (matching) technique

Biorthogonal filters designed using common factor technique have *approximately* linear-phase characteristics due to phase factor $(e^{-j\frac{\omega}{2}})$ approximation. Exact linear phase filters can be obtained using odd-even filter design technique. The goal here is to design the suitable even length filters of Tree-2 for the chosen odd-length filters of Tree-1. Note that in this case both even and odd length filters are real-valued and symmetric and lead to completely linear phase characteristics. This technique is in contrast to the common factor approach since the condition on phase is inherently satisfied and the problem is to approximate the condition in equation (4.5) by matching their magnitude responses, hence the name matching technique. In this approach, well known symmetric odd-length filters such as CDF 9/7 are used in the first tree. The filters in the second tree are chosen as symmetric even length filters which are designed such that their amplitude responses are matched with corresponding odd length filters in Tree-1. Let the frequency response of odd-length lowpass filters is denoted by $X_0^h(\omega)$ which can be represented in terms of amplitude response as [76]:

$$X_0^h(\omega) = x_0^h(0) + \sum_{n \neq 0} x_0^h(n) cos(\omega n) \tag{4.13}$$

$$= F_{0,R}^h(\omega). \tag{4.14}$$

Similarly, response of even length lowpass filters denoted using $X_0^g(\omega)$ can be written as

$$X_0^g(\omega) = e^{\frac{-j\omega}{2}} F_{0,R}^g(\omega), \quad \text{where} \tag{4.15}$$

$$F_{0,R}^g(\omega) = \sum_n 2x_0^g(n) \cos((n - \frac{1}{2})\omega). \tag{4.16}$$

Here, $F_{0,R}^h(\omega)$ and $F_{0,R}^g(\omega)$ represent real-valued functions of ω representing *amplitude responses* of odd and even-length lowpass filters, respectively. In equation (4.15), one may see the presence of inherent half-sample delay due to factor $e^{\frac{-j\omega}{2}}$. Assuming same signs for $F_{0,R}^h(\omega)$ and $F_{0,R}^g(\omega)$, we get $\angle X_0^g(\omega) = -\frac{\omega}{2} + \angle X_0^h(\omega)$

i.e., phase condition in equation (4.6) is perfectly satisfied. The problem thus reduces to approximating the amplitude responses as

$$F^h_{0,R}(\omega) \approx F^g_{0,R}(\omega). \tag{4.17}$$

In [102], Tay uses a shape parameter optimization of an even-length triplet half-band filter bank (ETHFB) to achieve the same. Approximation given in the equation (4.17) is realized in practise by minimizing the mean squared error function of the form

$$E = \int\limits_0^\pi (F^h_{0,R}(\omega) - F^g_{0,R}(\omega))^2 d\omega. \tag{4.18}$$

4.3 Proposed Approaches

In this section, we explain in detail our two approaches to design biorthogonal DTCWT filters. Both the approaches make use of factorization of a halfband polynomial, which is one of the earliest, simple and widely used approach in the wavelets and filter banks community to design the orthogonal/biorthogonal wavelet filters [98, 117, 118, 120]. A *halfband* polynomial is a finite odd-length symmetric polynomial with coefficients of even power as zero except for the center term which is 1. In the proposed approaches, we use factorization of generalized halfband polynomial (GHBP) [78]. Use of GHBP was first proposed by Le Gall et al. in [58] to design biorthogonal wavelet filters. One set of filters (Le Gall 5/3) proposed in [58] are being used in JPEG-2000 standard for lossless image compression. Following the "free some zeros" approach given by Tay in [108], Patil et al. [78] used higher order GHBP to obtain few independent (free) variables to improve frequency selectivity of the designed filters. In our first approach, we propose and design generalized halfband polynomial such that perfect reconstruction and vanishing moment and half-sample delay constraints are satisfied for any value of the free variables i.e., we design GHBP and obtain DTCWT filters.

4.3.1 Proposed HSD-based approach

Using equations (4.7) or (4.8), we obtain the generalized halfband polynomial for $P(z)$ that satisfies perfect reconstruction (PR) and vanishing moment (VM) and half-sample delay (HSD) constraints in order to design the DTCWT filters. Let us choose equation (4.7) for designing DTCWT filters of Tree-1 i.e., $\tilde{h}_0(n)$ and $h_0(n)$. There are three input parameters $\tilde{K}$, K and L. Here, $\tilde{K}$ and K represent number of vanishing moments for $\tilde{h}_0(n)$ and $h_0(n)$, respectively while L represents order of $d(n)$ i.e., denominator polynomial of an allpass filter used to approximate the HSD condition. Since, we wish to design $\tilde{h}_0(n)$ and $h_0(n)$ as real symmetric odd-length filters of arbitrary lengths, all the input parameters must be even. Let, n_f be the number of free variables used in the optimization to shape the frequency response characteristics. We then select the GHBP of order D given by

$$
\begin{aligned}
P^D(z) = a_0 + a_2 z^{-2} + \cdots + a_{(D/2)-1} z^{-(D/2)-1} + z^{-(D/2)} \\
+ a_{(D/2)-1} z^{-(D/2)+1} + \cdots + a_0 z^{-D},
\end{aligned}
\tag{4.19}
$$

where the polynomial order D is chosen as $D = 2(M-1) + 4L + 8n_f$. Note that, order D is chosen such that it includes *desired* number of VMs, L^{th} order all-pass HSD approximation with n_f degrees of freedom to shape the frequency responses of the filters. The values for the constants used are obtained heuristically after exhaustive experiments such that desired optimization results are obtained. Here, $M = \tilde{K} + K$ represents total number of VMs required in the design. For $P^D(z)$ of order D, there exist maximum $(\frac{D}{2} + 1)$ zeros at $z = -1$ and $\frac{(D+2)}{4}$ unknown variables i.e., a_i, $i = 0, 2, \ldots, (\frac{D}{2} - 1)$. By imposing M number of zeros at $z = -1$, the $P^D(z)$ can then be expressed as

$$
P^D(z) = (1 + z^{-1})^M R(z) = (1 + z^{-1})^{\tilde{K}+K} R(z)
\tag{4.20}
$$

where, the term $(1 + z^{-1})$ represents the condition on vanishing moments which decides smoothness or regularity of the wavelet functions and $R(z)$ is a remainder polynomial expressed in terms of free variables. Here, a double zero at $z = -1$

eliminates one degree of freedom from $P^D(z)$, thus $\frac{M}{2}$ unknown variables are expressed in terms of $n_f = \left(\frac{D+2}{4} - \frac{M}{2} \right)$ free variables in the remainder polynomial $R(z)$. With this, our modified product filter $P(z)$ to design the lowpass filters of Tree-1 can be chosen as

$$P(z) = \tilde{H}_0(z)H_0(z) \tag{4.21}$$

$$P(z) = P^D(z)D(z)D(z^{-1})z^{-L} \tag{4.22}$$

$$P(z) = P^D(z)D_L(z). \tag{4.23}$$

From equation (4.23), one can see that unlike common factor technique, we use GHBP $P^D(z)$ to obtain the factors $\tilde{F}_0(z)$ and $F_0(z)$ whose frequency response characteristics can be controlled using free variables. The polynomial factor $D_L(z) = D(z)D(z^{-1})z^{-L}$ used here represents *half-sample delay* constraint where $D(z)$ can be obtained using equation (4.12). Due to the factor $D_L(z)$, $P(z)$ is no longer a halfband polynomial and perfect reconstruction property of the designed filters is lost. Therefore, we impose halfband constraints on $P(z)$ to make it a halfband polynomial before the factorization step. Using equation (4.20), $P(z)$ can be then written as

$$P(z) = (1 + z^{-1})^{\tilde{K}+K}R(z)D_L(z) \tag{4.24}$$

$$P(z) = B_M(z)R(z)D_L(z) \tag{4.25}$$

$$P(z) = B(z)R(z) = \tilde{H}_0(z)H_0(z), \tag{4.26}$$

where $B_M(z) = (1 + z^{-1})^{\tilde{K}+K}$ and $B(z) = B_M(z)D_L(z)$.

Imposing halfband constraints: In equation (4.26), coefficients of the $B(z)$ polynomial are exactly known while $R(z)$ is a symmetric polynomial having unknown variables $a_i, i = 0, 2, \ldots, (D/2) - 1$ as coefficients. After collecting the terms of the product $B(z)R(z)$, we see that $P(z)$ has both odd and even powers of z i.e., it violates the halfband condition. Hence, coefficients of even powers of z are made 0 while the center term (or constant term) is chosen to be 1 in order to obtain the halfband polynomial $P(z)$. Remainder polynomial $R(z)$ in equation (4.26) is now

expressed in terms of desired n_f number of free variables.

Let remainder polynomial $R(z)$ given in equation (4.26) is factorized into two symmetric polynomials $R_1(z)$ and $R_2(z)$, respectively. Then the expressions for the factorized filters $\tilde{H}_0(z)$ and $H_0(z)$ can be written as

$$\tilde{H}_0(z) = (1 + z^{-1})^{\tilde{K}} R_1(z) D(z) \tag{4.27}$$

$$H_0(z) = (1 + z^{-1})^K R_2(z) D(z^{-1}) z^{-L}. \tag{4.28}$$

i.e.,

$$\tilde{H}_0(\omega) = (1 + z^{-1})^{\tilde{K}} R_1(z) D(z)\big|_{z=e^{j\omega}} \tag{4.29}$$

$$H_0(\omega) = (1 + z^{-1})^K R_2(z) D(z^{-1}) z^{-L}\big|_{z=e^{j\omega}}. \tag{4.30}$$

In order to obtain the filters $\tilde{H}_0(z)$ and $H_0(z)$ i.e., the analysis and synthesis low-pass filters of Tree-1, we minimize the following objective function with respect to n_f number of free variables. To do this we use MATLAB optimization toolbox routine *fminunc*.

$$
\begin{aligned}
F_{obj} = {} & \int_0^{\omega_p} \left|1 - \tilde{H}_0(\omega)\right|^2 d\omega + \int_{\omega_s}^{\pi} \left|\tilde{H}_0(\omega)\right|^2 d\omega \\
& + \int_0^{\omega_p} \left|1 - H_0(\omega)\right|^2 d\omega + \int_{\omega_s}^{\pi} \left|H_0(\omega)\right|^2 d\omega.
\end{aligned}
\tag{4.31}
$$

Here, ω_p and ω_s represent passband and stopband cut-off frequencies (in radian), respectively. During the optimization, for the given values of the free variables, polynomial $R(z)$ is first evaluated and factorized into polynomials $R_1(z)$ and $R_2(z)$. Since, this factorization is not unique the objective function is evaluated for all possible combinations of real-valued symmetric polynomials $R_1(z)$ and $R_2(z)$. We choose them to be symmetric polynomials such that $\tilde{h}_0(n)$ and $h_0(n)$ obtained are real-valued biorthogonal filters having near-orthogonal frequency response characteristics. Due to *approximation* of the HSD condition using finite length polynomial, the designed filters have approximate linear-phase property.

4.3.2 Proposed odd-even (matching) technique

In this approach, we use two stages in the design procedure. In the first stage, we design Tree-2 filters by using GHBP and unconstrained optimization approach. In the second stage referred as *shape-parameter optimization*, we modify the Tree-1 filters in order to improve the analytic quality of the designed filters. The first stage has two parts: 1) selection of Tree-1 filters and 2) design of Tree-2 filters using GHBP optimization explained as follows:

Selection of Tree-1 filters: we obtain the Tree-1 lowpass filters $\tilde{h}_0(n)$ and $h_0(n)$ by choosing them from a class of triplet halfband filter bank (THFB) proposed in [12]. The filter coefficients are chosen as:

$$\tilde{H}_0(z) = \frac{1+p}{2} + \left(\frac{1+p}{2}\right) z T_1(z^2) \left(\frac{1 - pz T_0(z^2)}{1+p}\right) \tag{4.32}$$

$$H_0(z) = \left(\frac{1 + pz T_0(z^2)}{1+p}\right) + \left(\frac{1-p}{1+p}\right) z T_2(z^2) H_0(-z). \tag{4.33}$$

The method uses three halfband filter kernels $T_0(z^2)$, $T_1(z^2)$ and $T_2(z^2)$ to take care of perfect reconstruction. Here p represents shape parameter and it gives flexibility to tailor the frequency response characteristics of the designed filters. Using different values of $p \in [0,1]$, the response value at $\omega = \frac{\pi}{2}$ for both the filters can be easily fixed. One may obtain biorthogonal filters having near-orthogonal response characteristics for $p = \sqrt{2} - 1$ which gives us $|H(\omega)|$ at $\omega = \frac{\pi}{2}$, same as in the case of orthogonal filters. Here, N_0, N_1 and N_2 are the lengths of the three halfband polynomials $T_0(z^2)$, $T_1(z^2)$ and $T_2(z^2)$, respectively. The vanishing moments for $\tilde{h}_0(n)$ and $h_0(n)$ are $2 * \min(N_0, N_1)$ and $2 * \min(N_0, N_1, N_2)$, respectively where $*$ denotes multiplication operation.

Designing Tree-2 filters using GHBP optimization: We restrict the Tree-2 lowpass filters i.e., $\tilde{g}_0(n)$ and $g_0(n)$ to be symmetric and even-length having their magnitude responses *matched* approximately to the magnitude responses of corresponding Tree-1 filters ($\tilde{h}_0(n)$ and $h_0(n)$). In order to do this, we use factorization of

GHBP as given in equation (4.19) with D chosen as

$$D = 2 * (M - 1) + 4 * n_f, \tag{4.34}$$

Here, $M = \tilde{K} + K$ with $\tilde{K}$ and K representing the number of VMs of $\tilde{g}_0(n)$ and $g_0(n)$, respectively. n_f represents the number of free variables. $\tilde{K}$ and K must be odd and they are chosen as:

$$\tilde{K} = 2 * \min(N_0, N_1) - 1$$
$$K = 2 * \min(N_0, N_1, N_2) - 1. \tag{4.35}$$

The final product filter $P(z)$ in this case is as given in equation (4.20). Here, $R(z)$ is a remainder polynomial expressed in terms of n_f number of free variables. After factorizing $R(z)$ into two symmetric polynomials $R_1(z)$ and $R_2(z)$, the lowpass filters $\tilde{G}_0(z)$ and $G_0(z)$ can be expressed as

$$\tilde{G}_0(z) = (1 + z^{-1})^{\tilde{K}} R_1(z) \tag{4.36}$$
$$G_0(z) = (1 + z^{-1})^K R_2(z). \tag{4.37}$$

Now the expressions for $\tilde{G}_0(\omega)$ and $G_0(\omega)$ to be used in the objective function can be written as

$$\tilde{G}_0(\omega) = (1 + z^{-1})^{\tilde{K}} R_1(z)|_{z=e^{j\omega}} \tag{4.38}$$
$$G_0(\omega) = (1 + z^{-1})^K R_2(z)|_{z=e^{j\omega}}. \tag{4.39}$$

We then use the MATLAB optimization function *fminunc* to minimize the following objective function with respect to the chosen number of free variables (n_f) and obtain the filters $\tilde{g}_0(n)$ and $g_0(n)$.

$$F_{obj} = \int_0^\pi \left(|\tilde{H}_0(\omega)| - |\tilde{G}_0(\omega)| \right)^2 d\omega + \int_0^\pi \left(|H_0(\omega)| - |G_0(\omega)| \right)^2 d\omega, \tag{4.40}$$

Here, the remainder polynomial $R(z)$ is factorized into symmetric factors $R_1(z)$

and $R_2(z)$ while performing the unconstrained minimization of the above objective function. With the optimized values of the free variables, we obtain symmetric even-length linear phase biorthogonal FIR filters $\tilde{g}_0(n)$ and $g_0(n)$ to be used in the Tree-2.

In order to have improved shift-invariance, we use second stage where we modify the Tree-1 filters using the Tree-2 filters obtained in first stage by further decreasing the error of magnitude approximation. Here, we modify the Tree-1 filters such that their magnitude responses better match to that of Tree-2 filters. We make use of equations (4.32) and (4.33) where shape parameter p is subjected to unconstrained optimization as follows.

Shape-parameter optimization: We minimize the error E given in equation (4.18) by *matching* the amplitude responses of the Tree-1 filters to their corresponding Tree-2 filters obtained at the first stage output. Here, we make use of one degree of freedom associated with the Tree-1 filters $\tilde{h}_0(n)$ and $h_0(n)$ in the form of shape parameter p. We use it for minimizing the magnitude error between filters of the two trees. The optimized shape parameter p for the Tree-1 filters is obtained by minimizing the following objective function

$$F_{obj} = \int_0^\pi \left(|\tilde{G}_0(\omega)| - |\tilde{H}_0(\omega)|\right)^2 d\omega + \int_0^\pi \left(|G_0(\omega)| - |H_0(\omega)|\right)^2 d\omega, \qquad (4.41)$$

where $\tilde{G}_0(\omega)$ and $G_0(\omega)$ are the outputs of the first stage i.e., the even-length filters $\tilde{g}_0(n)$ and $g_0(n)$. The expressions for $\tilde{H}_0(\omega)$ and $H_0(\omega)$ are from equations (4.32) and (4.33), respectively where z is replaced by $e^{j\omega}$. During the optimization, for a specific value of p, the objective function value is evaluated and optimization is continued until F_{obj} is minimized. Note that in this case $\tilde{G}_0(\omega)$ and $G_0(\omega)$ are fixed. Once the optimal value of p is known output filters $\tilde{h}_0(n)$ and $h_0(n)$ can be easily obtained using equations (4.32) and (4.33). The optimized filters of the first and second stage are then considered as the final DTCWT filters. Due to second stage optimization, analyticity of the associated wavelets is improved due to better *matching* between the magnitude responses given in equation (4.17).

4.4 Design Examples

In this section, we give numerous design examples for the two approaches proposed in section 4.3. The designed filters are analyzed qualitatively by showing their magnitude responses and wavelet function plots to judge the orthogonality and analyticity, respectively. Following conventions are true while displaying the analytic quality using wavelet function plots:

- For the first approach, wavelet functions have *mirror symmetry* only since it is a variant of common factor method and follow conventions of [91].

- For the second approach, wavelet functions have both *mirror* as well as *anti-symmetry* due to odd-even structure and follow conventions of [134][110].

The error measuring *analyticity* is quantified using two quantitative measures E_1 and E_2 given by Tay et al. in [106]. E_1 and E_2 as given in equations (4.42) and (4.43) measure the peak error and energy in the negative frequency region of the Fourier transform of complex wavelet basis, respectively.

$$E_1 = \frac{\max_{\omega<0}\left|\Psi_h(\omega) + j\Psi_g(\omega)\right|}{\max_{\omega>0}\left|\Psi_h(\omega) + j\Psi_g(\omega)\right|} \tag{4.42}$$

$$E_2 = \frac{\int\limits_{-\infty}^{0}\left|\Psi_h(\omega) + j\Psi_g(\omega)\right|^2 d\omega}{\int\limits_{0}^{\infty}\left|\Psi_h(\omega) + j\Psi_g(\omega)\right|^2 d\omega}, \tag{4.43}$$

where, $\Psi_h(\omega)$ and $\Psi_g(\omega)$ are Fourier transforms of Tree-1 and Tree-2 wavelets i.e., $\psi_h(t)$ and $\psi_g(t)$, respectively. Ideally, E_1 and E_2 must be 0. We express quantitative measures in terms of E_1_A, E_2_A, E_1_S, E_2_S, and E_1_Avg, E_2_Avg, where A, S and Avg represent analysis, synthesis and average, respectively.

Example-1: In this example, we design our first set of DTCWT filters using proposed HSD-based approach. Design specifications used in this example are: $\tilde{K} = K = 2$, $L = 2$ with one free variable for optimization i.e., $n_f = 1$. Our design procedure is as follows: Substituting the values of $\tilde{K}$, K, L and n_f in the expression

for D, we get $D = 22$. Hence $P^D(z)$ becomes

$$P^D(z) = a_0 + a_2 z^{-2} + a_4 z^{-4} + a_6 z^{-6} + a_8 z^{-8} + a_{10} z^{-10} + z^{-11}$$
$$+ a_{10} z^{-12} + a_8 z^{-14} + a_6 z^{-16} + a_4 z^{-18} + a_2 z^{-20} + a_0 z^{-22}.$$

Maximum number of VMs possible for this order is 12. With $M = \tilde{K} + K = 4$ zeros at $z = -1$ and $D(z)$ obtained using closed-form formula for $d(n)$ given in equation (4.12), $P(z)$ expressed in terms of equation (4.25) can be given by:

$$P(z) = (1 + z^{-1})^4 R(z) D(z) D(z^{-1}) z^{-2}. \tag{4.44}$$

From this, the expressions for $B_4(z)$, $R(z)$ and $D_2(z)$ are given as follows

$$B_4(z) = (1 + z^{-1})^4 = 1 + (4)z^{-1} + (6)z^{-2} + (4)z^{-3} + (1)z^{-4}.$$
$$R(z) = a_0 + a_2 z^{-1} + a_4 z^{-2} + a_6 z^{-3} + a_8 z^{-4} + a_{10} z^{-5} + a_8 z^{-6} + a_6 z^{-7}$$
$$+ a_4 z^{-8} + a_2 z^{-9} + a_0 z^{-10}.$$
$$D_2(z) = \left(\frac{1}{5}\right) + \left(\frac{12}{5}\right) z^{-1} + \left(\frac{126}{25}\right) z^{-2} + \left(\frac{12}{5}\right) z^{-3} + \left(\frac{1}{5}\right) z^{-4}.$$

After imposing the halfband constraints, the $R(z)$ can be expressed with one free variable a_8 as

$$R(z) = \left(\frac{5\,a_8}{1642} + \frac{3984125}{37448318976}\right) + \left(-\frac{40\,a_8}{821} - \frac{3984125}{2340519936}\right) z^{-1}$$
$$+ \left(\frac{401\,a_8}{1642} + \frac{302491075}{37448318976}\right) z^{-2} + \left(-\frac{512\,a_8}{821} - \frac{5660175}{390086656}\right) z^{-3}$$
$$+ (a_8) z^{-4} + \left(\frac{33075875}{1170259968} - \frac{944\,a_8}{821}\right) z^{-5} + (a_8) z^{-6}$$
$$+ \left(-\frac{512\,a_8}{821} - \frac{5660175}{390086656}\right) z^{-7} + \left(\frac{401\,a_8}{1642} + \frac{302491075}{37448318976}\right) z^{-8}$$
$$+ \left(-\frac{40\,a_8}{821} - \frac{3984125}{2340519936}\right) z^{-9} + \left(\frac{5\,a_8}{1642} + \frac{3984125}{37448318976}\right) z^{-10}.$$

The above $R(z)$ is factorized into two symmetric polynomials in z i.e., factors $R_1(z)$ and $R_2(z)$ during the optimization. For optimized value of $a_8 = -0.0101$, the lowpass filters $\tilde{h}_0(n)$ and $h_0(n)$ obtained have the lengths of 7 and 13, respec-
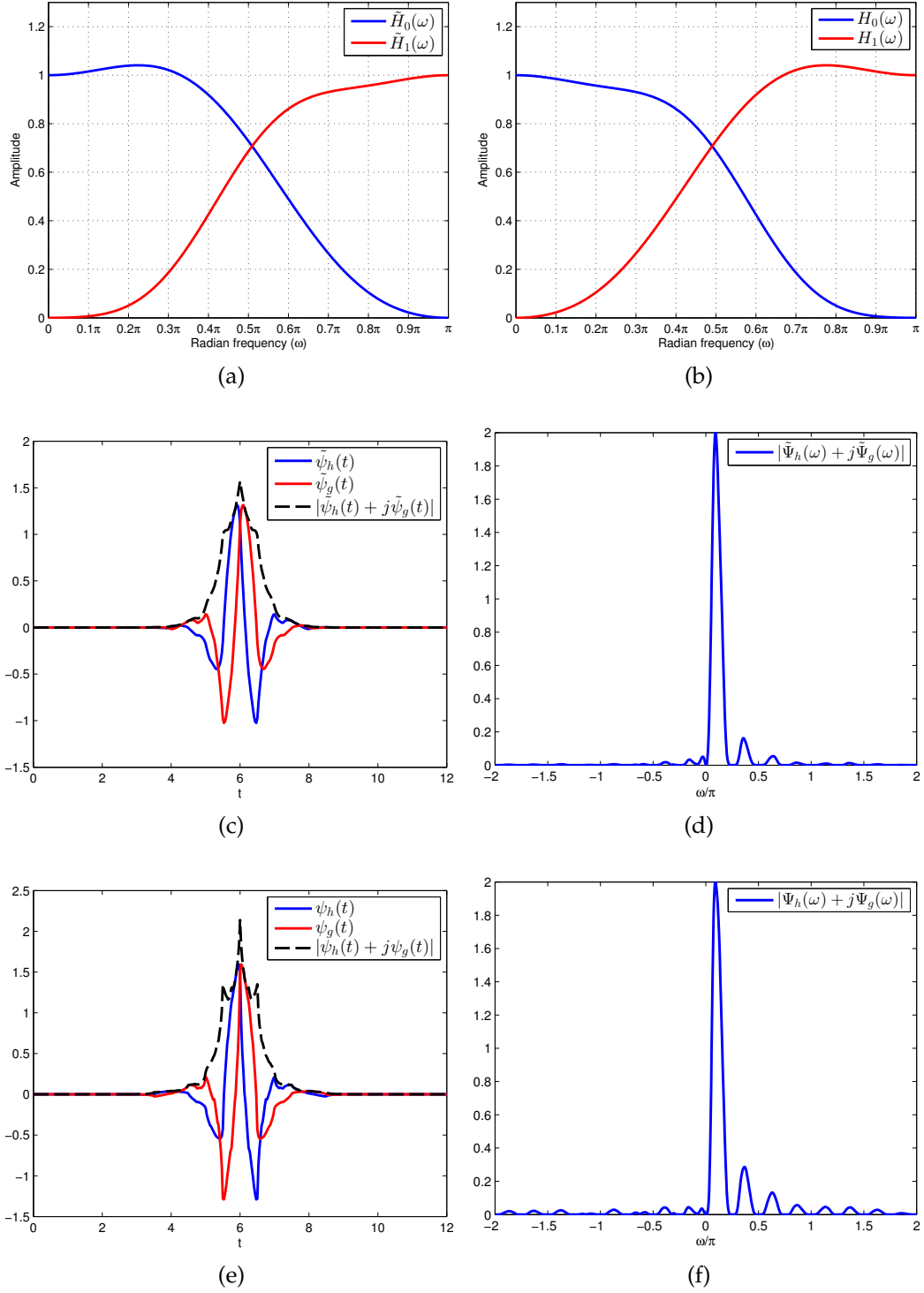
Figure 4.2: Plots for Example-1 (a) magnitude responses of analysis filters of Tree-1 i.e., $|\tilde{H}_0(\omega)|$ and $|\tilde{H}_1(\omega)|$ (b) magnitude responses of synthesis filters of Tree-1 i.e., $|H_0(\omega)|$ and $|H_1(\omega)|$. (c) Analysis wavelet functions $\tilde{\psi}_h(t)$, $\tilde{\psi}_g(t)$ and $|\tilde{\psi}_h(t) + j\tilde{\psi}_g(t)|$ (d) Magnitude frequency spectrum for $|\tilde{\Psi}_h(\omega) + j\tilde{\Psi}_g(\omega)|$ (e) Synthesis wavelet functions $\psi_h(t)$, $\psi_g(t)$ and $|\psi_h(t) + j\psi_g(t)|$ (f) Magnitude frequency spectrum for $|\Psi_h(\omega) + j\Psi_g(\omega)|$.

57

tively having the coefficients given in Table 4.1. From these coefficients, Tree-2 filters i.e., $\tilde{g}_0(n)$ and $g_0(n)$ are obtained using equations (4.9) and (4.10), where $\tilde{N} = 7$ and $N = 13$, respectively. Figure 4.2 shows magnitude responses of Tree-1 filters. The plots of wavelet functions for analyzing the quality of their associated Hilbert transform pairs of wavelet bases are also shown in the same figure. Magnitude responses for Tree-2 filters are similar to Tree-1 filters due to time-reversal relationship. From Figure 4.2, we can see that frequency response characteristics

Table 4.1: Coefficients of the Example-1 filters.

n	$\tilde{h}_0(n)$	$h_0(n)$
1	0.0455	0.0002
2	0.0128	-0.0000
3	-0.3944	-0.0156
4	-0.5882	0.0061
5	-0.1602	0.0680
6	0.0753	-0.1679
7	0.0091	-0.5394
8	-	-0.3767
9	-	-0.0004
10	-	0.0454
11	-	-0.0136
12	-	-0.0069
13	-	0.0008

of the designed filters appear closer to the orthogonal filter response characteristics as well as analyticity of the wavelets is good as evident from Fig. 4.2(d) and 4.2(f). Quantitative measures for analyticity of the complex wavelets obtained from the designed filters are tabulated in Table 4.7. One can see that the values of analyticity measures are closer to zero indicating a better design.

Example-2: In this example, we consider number of free variables as 3 i.e., $n_f = 3$, keeping all other specifications same as in the Example-1. This is done to see the effect of number of free variables on the desired frequency response of
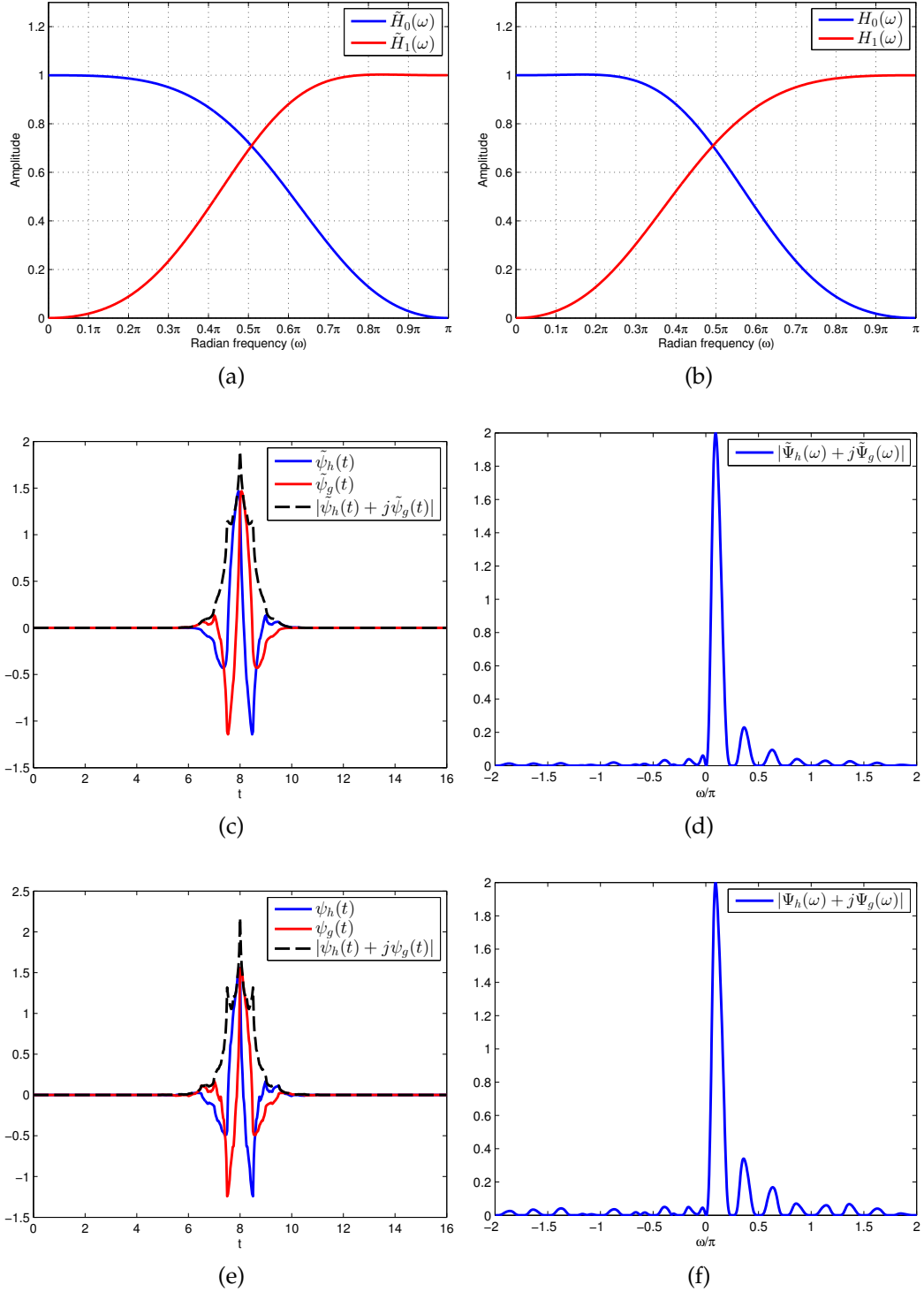
Figure 4.3: Plots for Example-2 (a) magnitude responses of analysis filters of Tree-1 i.e., $|\tilde{H}_0(\omega)|$ and $|\tilde{H}_1(\omega)|$ (b) magnitude responses of synthesis filters of Tree-1 i.e., $|H_0(\omega)|$ and $|H_1(\omega)|$. (c) Analysis wavelet functions $\tilde{\psi}_h(t)$, $\tilde{\psi}_g(t)$ and $|\tilde{\psi}_h(t) + j\tilde{\psi}_g(t)|$ (d) Magnitude frequency spectrum for $|\tilde{\Psi}_h(\omega) + j\tilde{\Psi}_g(\omega)|$ (e) Synthesis wavelet functions $\psi_h(t)$, $\psi_g(t)$ and $|\psi_h(t) + j\psi_g(t)|$ (f) Magnitude frequency spectrum for $|\Psi_h(\omega) + j\Psi_g(\omega)|$.

59

designed filters. For this set of design parameters, the length of the filters $\tilde{h}_0(n)$ and $h_0(n)$ correspond to 11 and 17, respectively. Following the design procedure for HSD-based technique, we obtain the filter coefficients as given in Table 4.2. The different plots for this example are shown in Fig. 4.3 and the quantitative measures are given in Table 4.7. It is clear from the magnitude responses given

Table 4.2: Coefficients of the Example-2 filters.

n	$\tilde{h}_0(n)$	$h_0(n)$
1	0.0007	0.0000
2	-0.0071	0.0000
3	0.0278	-0.0001
4	0.0184	-0.0011
5	-0.3775	-0.0043
6	-0.5782	0.0082
7	-0.1438	0.0677
8	0.0672	-0.1633
9	-0.0074	-0.5636
10	-0.0003	-0.3839
11	0.0001	0.0038
12	-	0.0429
13	-	-0.0033
14	-	-0.0028
15	-	-0.0003
16	-	0.0000
17	-	0.0000

in Fig. 4.3(a) and Fig. 4.3(b) that the designed filters have frequency responses comparable to that of quadrature mirror filters (QMFs) and the response characteristics are better when compared to that of Example-1. However this is possible at the cost of increase in filter lengths leading to increase in computational cost. We observe that, the analyticity of the filters $\tilde{h}_0(n)$ and $h_0(n)$ is marginally inferior both visually as well as quantitatively when compared to Example-1.

Figure 4.4: Plots for Example-3 (a) magnitude responses of analysis filters of Tree-1 i.e., $|\tilde{H}_0(\omega)|$ and $|\tilde{H}_1(\omega)|$ (b) magnitude responses of synthesis filters of Tree-1 i.e., $|H_0(\omega)|$ and $|H_1(\omega)|$. (c) Analysis wavelet functions $\tilde{\psi}_h(t)$, $\tilde{\psi}_g(t)$ and $|\tilde{\psi}_h(t) + j\tilde{\psi}_g(t)|$ (d) Magnitude frequency spectrum for $|\tilde{\Psi}_h(\omega) + j\tilde{\Psi}_g(\omega)|$ (e) Synthesis wavelet functions $\psi_h(t)$, $\psi_g(t)$ and $|\psi_h(t) + j\psi_g(t)|$ (f) Magnitude frequency spectrum for $|\Psi_h(\omega) + j\Psi_g(\omega)|$.

61

Example-3: We now consider another example where everything else being same as in Example-1 only the order L is changed which is set to 4. Intuitively, this should yield better HSD approximation and hence should improve the analyticity of the resulting filters. This, however occurs at the cost of increased lengths. For the chosen parameters, lengths of the filters $\tilde{h}_0(n)$ and $h_0(n)$ obtained are 15 and 13, respectively. The coefficients of these filters are given in Table 4.3 while the necessary plots are shown in Fig. 4.4. Analyticity measures for the wavelets obtained using these filters are given in Table 4.7. One can observe from the plots

Table 4.3: Coefficients of the Example-3 filters.

n	$\tilde{h}_0(n)$	$h_0(n)$
1	0.0001	0.0000
2	0.0003	-0.0000
3	-0.0037	-0.0034
4	-0.0151	0.0159
5	0.0399	0.0700
6	0.0118	-0.1682
7	-0.3821	-0.5696
8	-0.5523	-0.3996
9	-0.1537	0.0053
10	0.0658	0.0528
11	0.0001	-0.0023
12	-0.0107	-0.0009
13	-0.0005	0.0000
14	0.0002	-
15	0.0000	-

given in Fig. 4.4 that the magnitude responses of both the analysis and synthesis filters are similar to that of Example-1. Note that the analyticity is better in this case when compared to both Example-1 and 2. For $\omega < 0$, we see that the magnitude frequency plots of $|\tilde{\Psi}_h(\omega) + j\tilde{\Psi}_g(\omega)|$ and $|\Psi_h(\omega) + j\Psi_g(\omega)|$ have negligible frequency contents. This can also be verified from the quantitative measures given in Table 4.7 where the measures corresponding to E_2 have negligible values.

Example-4: In this example, we show the improvement in the frequency response characteristics of the designed filters using proposed HSD-based approach over the common factor technique [91] proposed by Ivan Selesnick. The input parameters chosen are $\tilde{K} = 2$, $K = 4$, $L = 2$ and $n_f = 1$. With this set of parameters, the lengths of the designed filters $\tilde{h}_0(n)$ and $h_0(n)$ are 11 and 13, respectively and their coefficients are given in Table 4.4. We have chosen this set of input parameters since the lengths of the filters obtained using our approach are same as the biorthogonal filters given in Table III of [91]. These filters were obtained using *maxflat* factorization approach of Daubechies [26] with input parameters as $\tilde{K} = K = 4$ and $L = 2$ and we refer to them as Selesnick's 11/13 filters. Since free variables are not used in common factor technique [91], there is no control over frequency response characteristics of the designed filters. We see from Table 4.4

Table 4.4: Coefficients of the Example-4 filters.

n	$\tilde{h}_0(n)$	$h_0(n)$
1	0.0015	0.0002
2	0.0007	-0.0001
3	0.0381	-0.0195
4	0.0080	0.0113
5	-0.3869	0.0772
6	-0.5781	-0.1724
7	-0.1584	-0.5473
8	0.0670	-0.3851
9	0.0055	0.0031
10	0.0025	0.0551
11	0.0003	-0.0149
12	-	-0.0088
13	-	0.0010

that the filter coefficients obtained in our case are entirely different from [91]. Figure 4.5 shows magnitude response characteristics of the proposed and Selesnick's 11/13 filters. It is clear that the frequency responses of the proposed filters are much better and they are close to response characteristics of near-orthogonal fil-

ters when compared to those designed using maxflat approach. Wavelet plots for the proposed filters are not shown since they are similar to that of Example-1, however analytic quality measures for the same are given in Table 4.7.
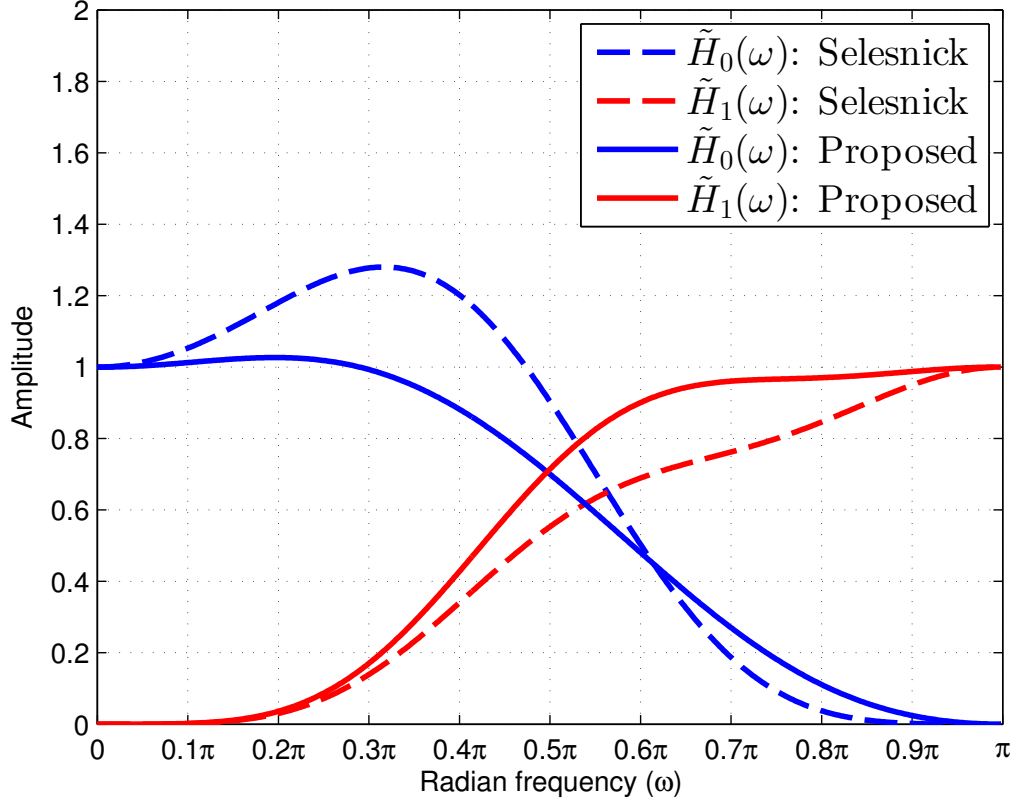
Figure 4.5: Magnitude response comparison between Tree-1 analysis filters of proposed 11/13 filters of Example-4 and Selesnick's 11/13 filters.

Improving linear-phase approximation and analyticity: In the proposed HSD-based approach, the HSD constraint given in equation (4.4) is satisfied using an allpass filter approximation $A(z)$ of the form given in equation (4.11). Hence for a finite L, we can write $A(e^{j\omega}) \approx e^{j\theta(\omega)}$, where $\theta(\omega) = -\frac{\omega}{2}$ which represents the phase delay between the scaling filters of the two trees of DTCWT. Figures 4.6(a) and 4.6(b) show the phase response characteristics obtained using the proposed approach for orders $L = 2$ and $L = 4$, respectively. Note that they are only dependent on the phase response characteristics of the numerator and denominator polynomials of the HSD condition given in equation (4.11). As stated in section 2.2, ideally L should be infinite to have the exact linear phase over the entire frequency range of 0 to 1. Since it should be finite in practice, the biorthogonal DTCWT

filters designed using the proposed HSD-based approach exhibit *approximate* linear phase characteristics. Obtaining the exact linear phase is desirable to make the wavelet functions completely symmetric which results in better directional selectivity. This gives improved performance in applications such as denoising, superresolution etc. [91]. Note that, it is not possible to obtain the exact linear phase using the $A(z)$ as in equation (4.11) using finite L. Although increase in L improves the linearity, this also increases the resulting filter lengths. For design examples 1-4, we used the maximally flat approximation of the $A(z)$ while designing the filters. But the use of such an approximation increases the error in linear phase as $|\omega|$ increases which is clearly seen in the Figures 4.6(a) and 4.6(b). One can observe that significant deviation from linearity occurs for $\frac{\omega}{\pi} > 0.5$ and $\frac{\omega}{\pi} > 0.7$ for $L = 2$ and $L = 4$, respectively. Such a phase approximation leads to poor analyticity of the DTCWT [126]. Hence, a practical approach is to use the *minimax* or L_∞ approximation rather than maximally flat all-pass filter approximation [36][103][139][126]. Hence, we also propose to use minimax approximation to improve the analyticity there by obtaining better linear-phase approximation of designed filters with the use of comparatively smaller filter lengths. Also, by using minimax approximation one can design filters with better frequency selectivity. In our case we focus mainly on improving the analyticity by using minimax HSD approximation. The approach proposed in [56] is used to design the filter $d(n)$ of desired order L. Improvements over maximally flat approach are shown by designing the filters with same input parameters as in Example-2 and Example-3. We first discuss their analyticity followed by improvements in the linear phase characteristics.

Example-5: Design parameters used here are the same as in the Example-2. Table 4.5 shows the filter coefficients of the designed filters, while in Fig. 4.7 we display the various plots. Although these plots appear similar to those given in Fig. 4.3, analyticity measures for the magnitude spectrum plots shown in Figs. 4.7(d) and 4.7(f) indicate significant improvement in terms of reduced ripples in the negative frequency region.
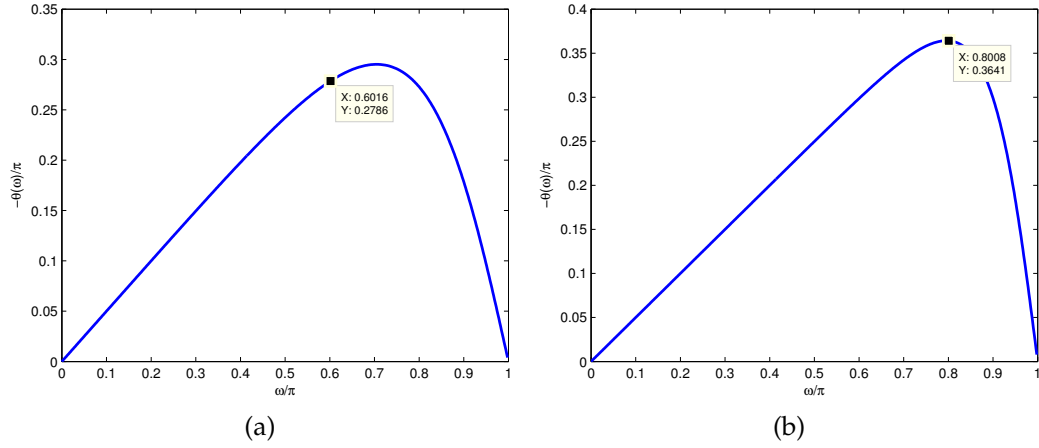
Figure 4.6: Phase response $\frac{\omega}{\pi}$ vs. $-\frac{\theta(\omega)}{\pi}$ for (a) $L = 2$. (b) $L = 4$ obtained using the maximally flat all-pass filter approximation of half-sample delay condition in the proposed HSD-based method.

Table 4.5: Coefficients of the Example-5 filters.

| n	$\tilde{h}_0(n)$	$h_0(n)$
1	0.0053	0.0000
2	-0.0439	0.0000
3	-0.0094	0.0000
4	0.3901	0.0001
5	0.5636	0.0008
6	0.1604	0.0057
7	-0.0610	-0.0006
8	-0.0067	-0.0648
9	0.0016	0.1523
10	-	0.5652
11	-	0.3869
12	-	-0.0178
13	-	-0.0416
14	-	0.0115
15	-	0.0021
16	-	0.0002
17	-	0.0000
18	-	0.0000
19	-	0.0000
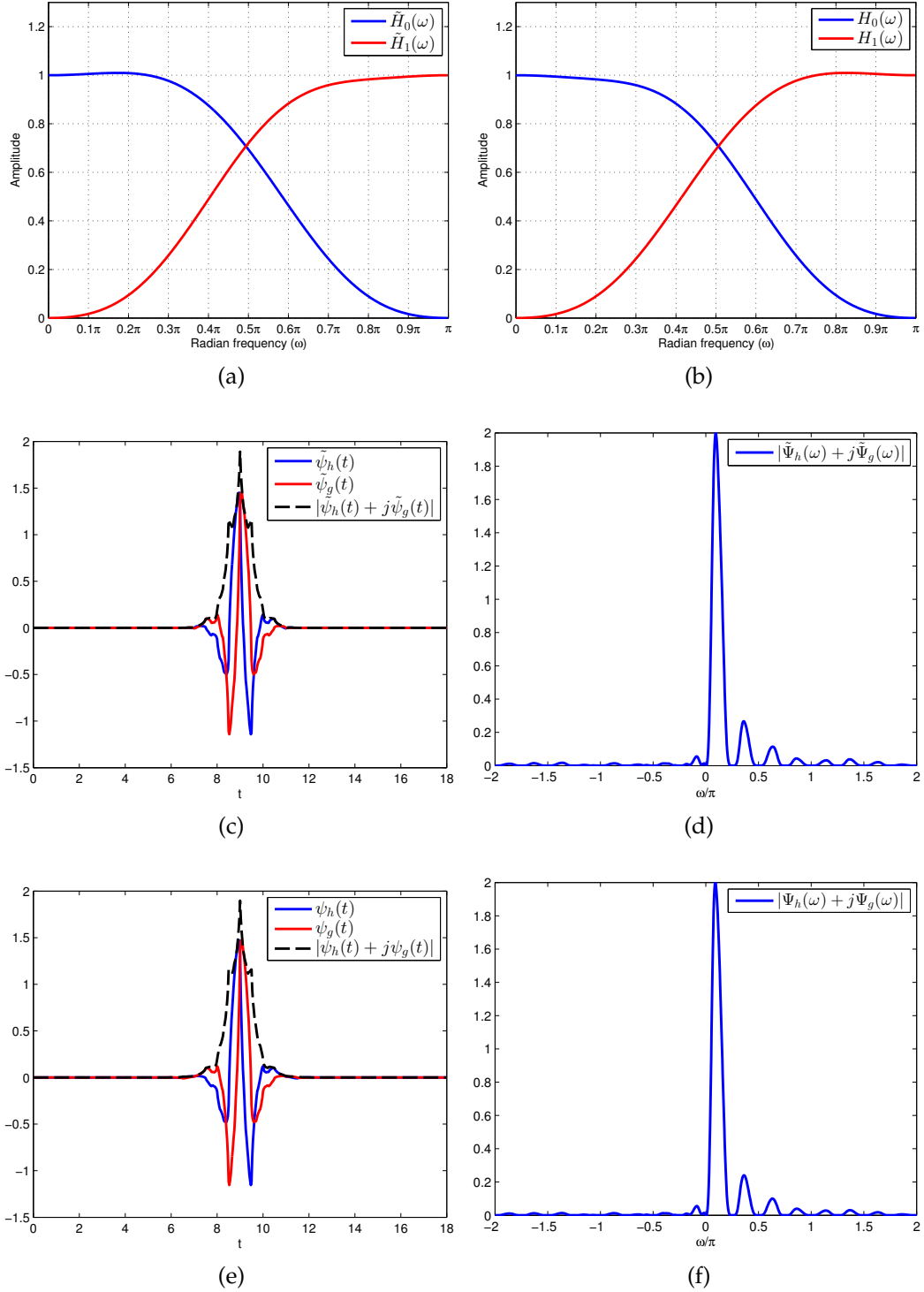
Figure 4.7: Plots for Example-5 (a) magnitude responses of analysis filters of Tree-1 i.e., $|\tilde{H}_0(\omega)|$ and $|\tilde{H}_1(\omega)|$ (b) magnitude responses of synthesis filters of Tree-1 i.e., $|H_0(\omega)|$ and $|H_1(\omega)|$. (c) Analysis wavelet functions $\tilde{\psi}_h(t)$, $\tilde{\psi}_g(t)$ and $|\tilde{\psi}_h(t) + j\tilde{\psi}_g(t)|$ (d) Magnitude frequency spectrum for $|\tilde{\Psi}_h(\omega) + j\tilde{\Psi}_g(\omega)|$ (e) Synthesis wavelet functions $\psi_h(t)$, $\psi_g(t)$ and $|\psi_h(t) + j\psi_g(t)|$ (f) Magnitude frequency spectrum for $|\Psi_h(\omega) + j\Psi_g(\omega)|$.

Example-6: Design parameters for this example are same as in the Example-3. In this case also, similar to Example-5, analyticity improvements can be visually seen by comparing the magnitude spectrum plots shown in Figs. 4.9(d) and 4.9(f) to those given in Figs. 4.4(d) and 4.4(f), respectively. The filter coefficients are shown in Table 4.6.

Table 4.6: Coefficients of the Example-6 filters.

n	$\tilde{h}_0(n)$	$h_0(n)$
1	0.0002	0.0000
2	0.0006	-0.0000
3	-0.0065	-0.0004
4	-0.0174	0.0012
5	0.0466	-0.0026
6	0.0094	0.0169
7	-0.3841	0.0696
8	-0.5461	-0.1703
9	-0.1595	-0.5694
10	0.0689	-0.4021
11	0.0042	0.0048
12	-0.0158	0.0534
13	-0.0008	-0.0020
14	0.0005	0.0009
15	0.0000	-0.0000
16	-	-0.0002
17	-	0.0000

Improvement in the analyticity measures for Example-5 and 6 can also be verified by looking at Table 4.7, where both E_1 and E_2 measures have near ideal values. Both the examples signify importance of using *minimax* approach for obtaining improved analyticity of wavelet functions when approximation to half-sample delay constraint is used during DTCWT filter design.
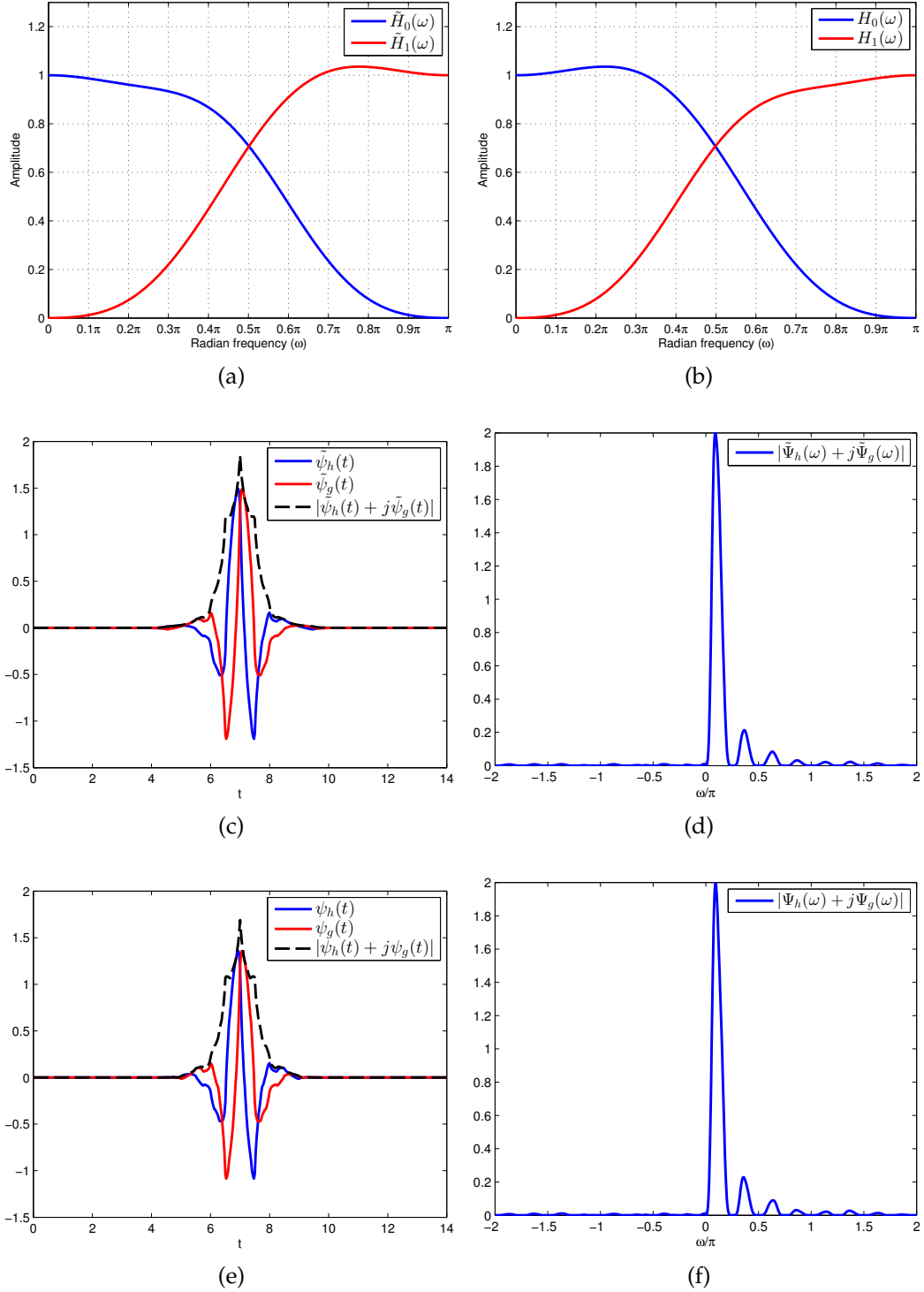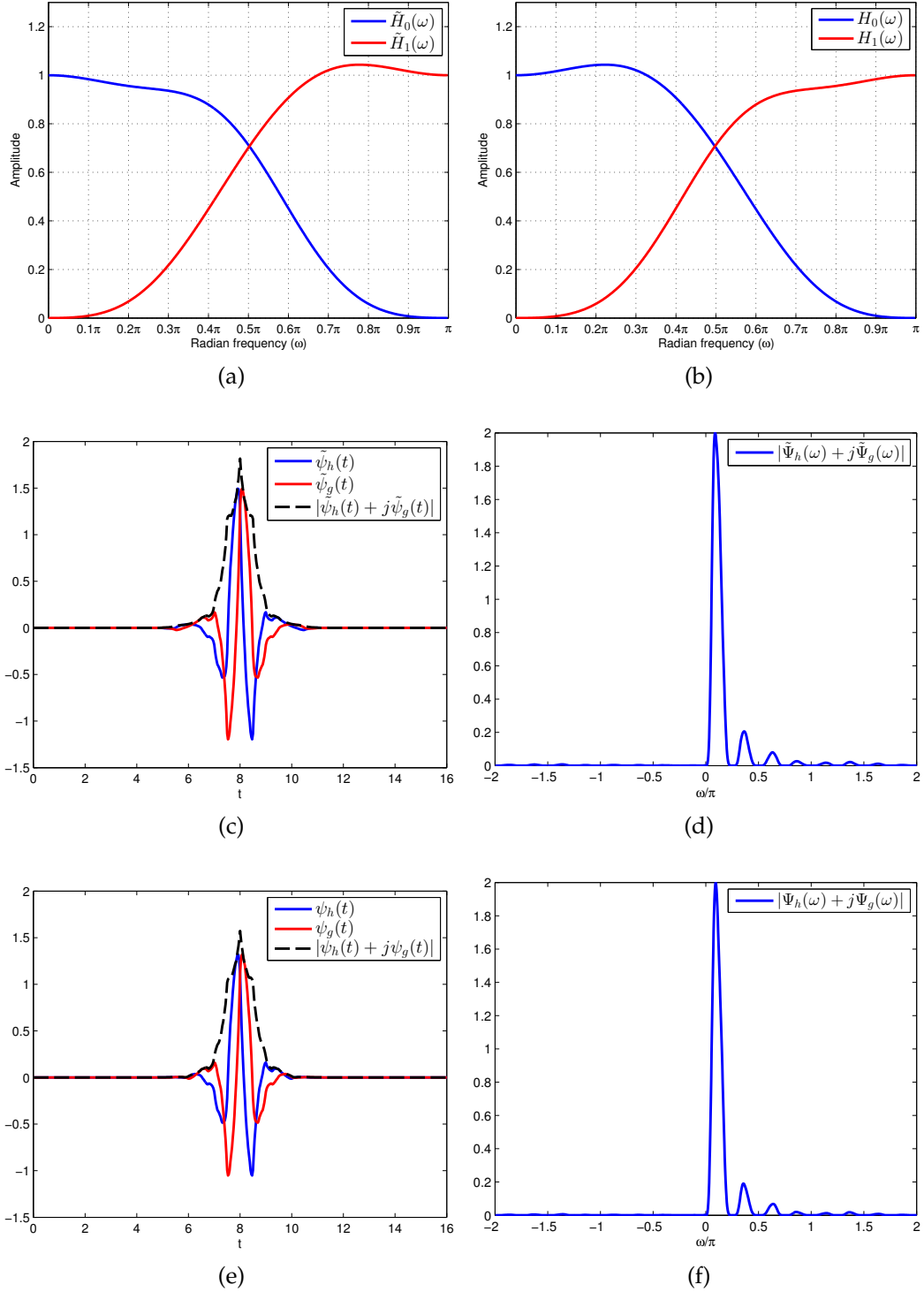
Figure 4.9: Plots for Example-6 (a) magnitude responses of analysis filters of Tree-1 i.e., $|\tilde{H}_0(\omega)|$ and $|\tilde{H}_1(\omega)|$ (b) magnitude responses of synthesis filters of Tree-1 i.e., $|H_0(\omega)|$ and $|H_1(\omega)|$. (c) Analysis wavelet functions $\tilde{\psi}_h(t)$, $\tilde{\psi}_g(t)$ and $|\tilde{\psi}_h(t) + j\tilde{\psi}_g(t)|$ (d) Magnitude frequency spectrum for $|\tilde{\Psi}_h(\omega) + j\tilde{\Psi}_g(\omega)|$ (e) Synthesis wavelet functions $\psi_h(t)$, $\psi_g(t)$ and $|\psi_h(t) + j\psi_g(t)|$ (f) Magnitude frequency spectrum for $|\Psi_h(\omega) + j\Psi_g(\omega)|$.

69

Figure 4.8 shows improvements in linear-phase characteristics for minimax all-pass HSD approximation used in our approach over the maximally flat approach shown in Fig. 4.6. To show the improvements, we have selected normalized angular frequency points at $\frac{\omega}{\pi} = 0.6$ and $\frac{\omega}{\pi} = 0.8$ in Figs. 4.6(a), 4.8(a) and Figs. 4.6(b), 4.8(b), respectively. One can see that approximate linear phase characteristics are improved for the minimax approach.

(a) (b)
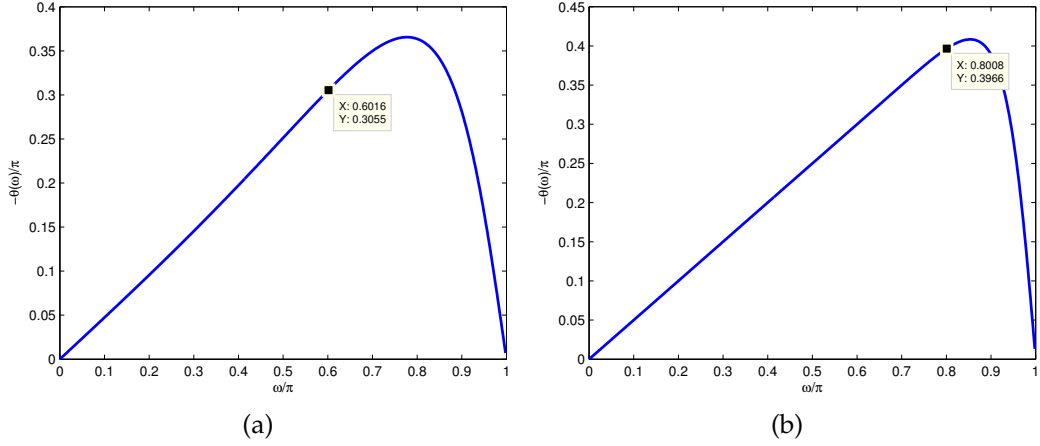
Figure 4.8: Phase response $\frac{\omega}{\pi}$ vs. $-\frac{\theta(\omega)}{\pi}$ for (a) $L = 2$. (b) $L = 4$ obtained using minimax all-pass filter approximation used in our approach.

Figures 4.10(a) and 4.10(b) are shown to compare phase approximation characteristics of maximally flat and minimax approaches along with their respective error plots. It is clear from these plots that minimax approximation with $L = 2$ is nearly similar to that of maximally flat approximation with $L = 4$. Similarly minimax approximation with $L = 4$ shows much better linear-phase characteristics than the maximally flat approximation with $L = 4$. From error plots given in Fig. 4.10(b), it is clear that by using minimax all-pass HSD approximation, smaller phase error is obtained as $|\omega|$ increases when compared to the maximally flat approximation. Due to better linear phase approximation, analyticity of wavelets is also improved both visually as well as quantitatively as verified from Figs. (4.7), (4.9) and Table 4.7, respectively.

Orthogonality measures: For qualitative evaluation of the frequency response characteristics of the proposed filters, we use two orthogonality measures given in [62] and [84]. They indicate how good the response characteristics match to the
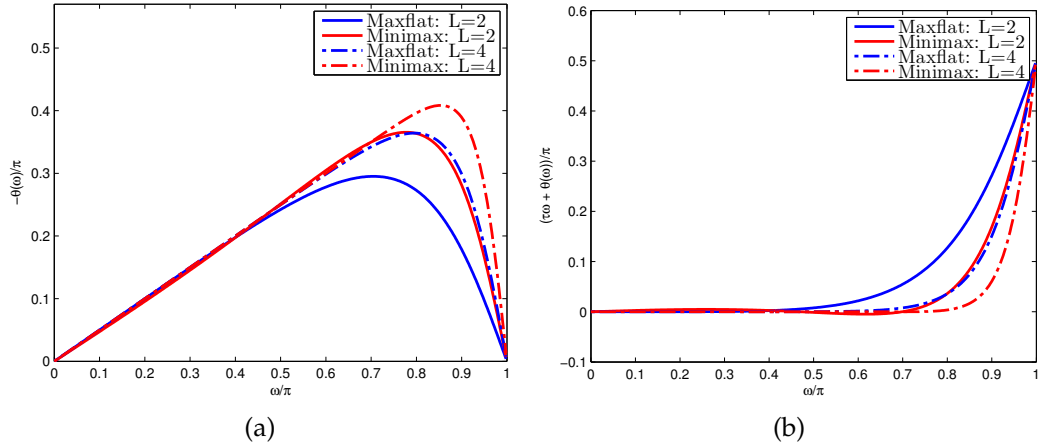
Figure 4.10: (a)Phase response $\frac{\omega}{\pi}$ vs. $-\frac{\theta(\omega)}{\pi}$ comparison for maximally flat and minimax approximations with $L = 2, 4$. (b) Error plots for the phase approximations shown in Fig. 4.10(a).

Table 4.7: Analyticity measures for the different wavelet bases.

	E_1_A	E_2_A	E_1_S	E_2_S	E_1_Avg	E_2_Avg
Example-1	0.0256	0.0006	0.0213	0.0010	0.0235	0.0008
Example-2	0.0308	0.0009	0.0239	0.0015	0.0274	0.0012
Example-3	0.0048	4.4E-5	0.0047	4.6E-5	0.0047	4.5E-5
Example-4	0.0260	0.0005	0.0218	0.0010	0.0239	0.0008
Example-5	0.0276	0.0006	0.0272	0.0005	0.0274	0.0005
Example-6	**0.0011**	**5.7E-6**	**0.0010**	**2.8E-6**	**0.0010**	**4.2E-6**
Selesnick 11/13 [91]	0.0180	3.2E-04	0.0161	3.7E-04	0.0171	3.4E-04

orthogonal filters which have ideal value of 0. Expression for the first measure used is:

$$ON1 = \frac{1}{\pi} \int_0^\pi (2 - O(\omega))^2 d\omega, \tag{4.45}$$

where $O(\omega) = O(z)|_{z=e^{j\omega}}$ with $O(z) = H_0(z)H_0(z^{-1}) + H_1(z)H_1(z^{-1})$. Expression for the second measure is:

$$ON2 = \left| \left| H_0\left(\frac{\pi}{2}\right) \right| - \left| H_1\left(\frac{\pi}{2}\right) \right| \right|. \tag{4.46}$$

Here, $H_0(z)$ and $H_1(z)$ denote analysis lowpass and highpass filters, respectively. Table 4.8 shows comparison of orthogonality measures for different filters designed using the proposed HSD-based approach and common factor technique.

Table 4.8: Orthogonality measures for the different filters.

	ON1 [62]	ON2 [84]
Example-1	0.0025	0.0421
Example-2	8.8E-04	0.0310
Example-3	0.0030	**0.0061**
Example-4	0.0010	0.0145
Example-5	**2.5E-04**	0.0259
Example-6	0.0031	0.0114
Selesnick 11/13 [91]	0.0372	0.3510

From Table 4.8, one can see that values of orthogonality measures for the filters obtained using proposed HSD-based approach are near to ideal value i.e., zero. For Selesnick's 11/13 filters obtained using common factor approach [91] these values are significantly high indicating their poor frequency response characteristicss.

Example-7: Here, we give a design example for our second approach i.e., proposed odd-even (matching) technique. For better understanding, we analyze the outputs of the two stages. In the first stage, Tree-1 filters $\tilde{h}_0(n)$ and $h_0(n)$ are obtained using equations (4.32) and (4.33), respectively with chosen parameters as $N_0 = N_1 = N_2 = 2$ and $p = \sqrt{2} - 1$ for the design specifications $\tilde{K} = K = 4$. The lengths of resulting filters are 13 and 19, respectively the coefficients of which are given in Table 4.9. To design the Tree-2 filters $\tilde{g}_0(n)$ and $g_0(n)$ using GHBP optimization we choose $n_f = 1$ i.e., one free variable. GHBP order D and number of vanishing moments are set automatically using equations (4.34) and (4.35), respectively. Coefficients of the remainder polynomial $R(z)$ are then obtained using equations (4.19) and (4.20) as given below

$$\left[(a_0), \quad (-6\,a_0), \quad \left(\frac{513\,a_0}{32} + \frac{3}{256} \right), \quad \left(-\frac{419\,a_0}{16} - \frac{9}{128} \right), \quad \left(\frac{489\,a_0}{16} + \frac{19}{128} \right) \right.$$
$$\left. \left(-\frac{419\,a_0}{16} - \frac{9}{128} \right), \quad \left(\frac{513\,a_0}{32} + \frac{3}{256} \right), \quad (-6\,a_0), \quad (a_0) \right] .$$

During the unconstrained optimization, remainder polynomial $R(z)$ is factorized into $R_1(z)$ and $R_2(z)$. For the optimized value of the free variable $a_0 = -9.2448 \times 10^{-04}$, F_{obj} in equation (4.40) is minimum and Tree-2 filters $\tilde{g}_0(n)$ and $g_0(n)$ of length 10 and 6, respectively are obtained. The coefficients for the same are as

Table 4.9: Coefficients of the filters $\tilde{h}_0(n)$ and $h_0(n)$ used for GHBP optimization stage.

n	$\tilde{h}_0(n)$	$h_0(n)$
1	-0.0008	0.0000
2	0.0000	0.0000
3	0.0146	-0.0006
4	-0.0313	-0.0008
5	-0.0510	0.0045
6	0.2813	0.0146
7	0.5744	-0.0416
8	0.2813	-0.0510
9	-0.0510	0.2877
10	-0.0313	0.5744
11	0.0146	0.2877
12	0.0000	-0.0510
13	-0.0008	-0.0416
14	-	0.0146
15	-	0.0045
16	-	-0.0008
17	-	-0.0006
18	-	0.0000
19	-	0.0000

given in Table 4.10.

Table 4.10: Coefficients of the filters $\tilde{g}_0(n)$ and $g_0(n)$ using the proposed odd-even technique

n	1	2	3	4	5	6	7	8	9	10
$\tilde{g}_0(n)$	0.0076	0.0080	-0.0641	0.0602	0.4883	0.4883	0.0602	-0.0641	0.0080	0.0076
$g_0(n)$	0.0610	-0.0640	-0.4970	-0.4970	-0.0640	0.0610	-	-	-	-

Figures 4.12 and 4.11 show frequency response characteristics of the Example-7 (stage-1) filters and their associated Hilbert pairs of wavelet bases, respectively. It is quite clear from Fig. 4.12 that the both Tree-1 and Tree-2 filters have near-orthogonal or almost-QMF frequency response characteristics. Fig. 4.12(e) and
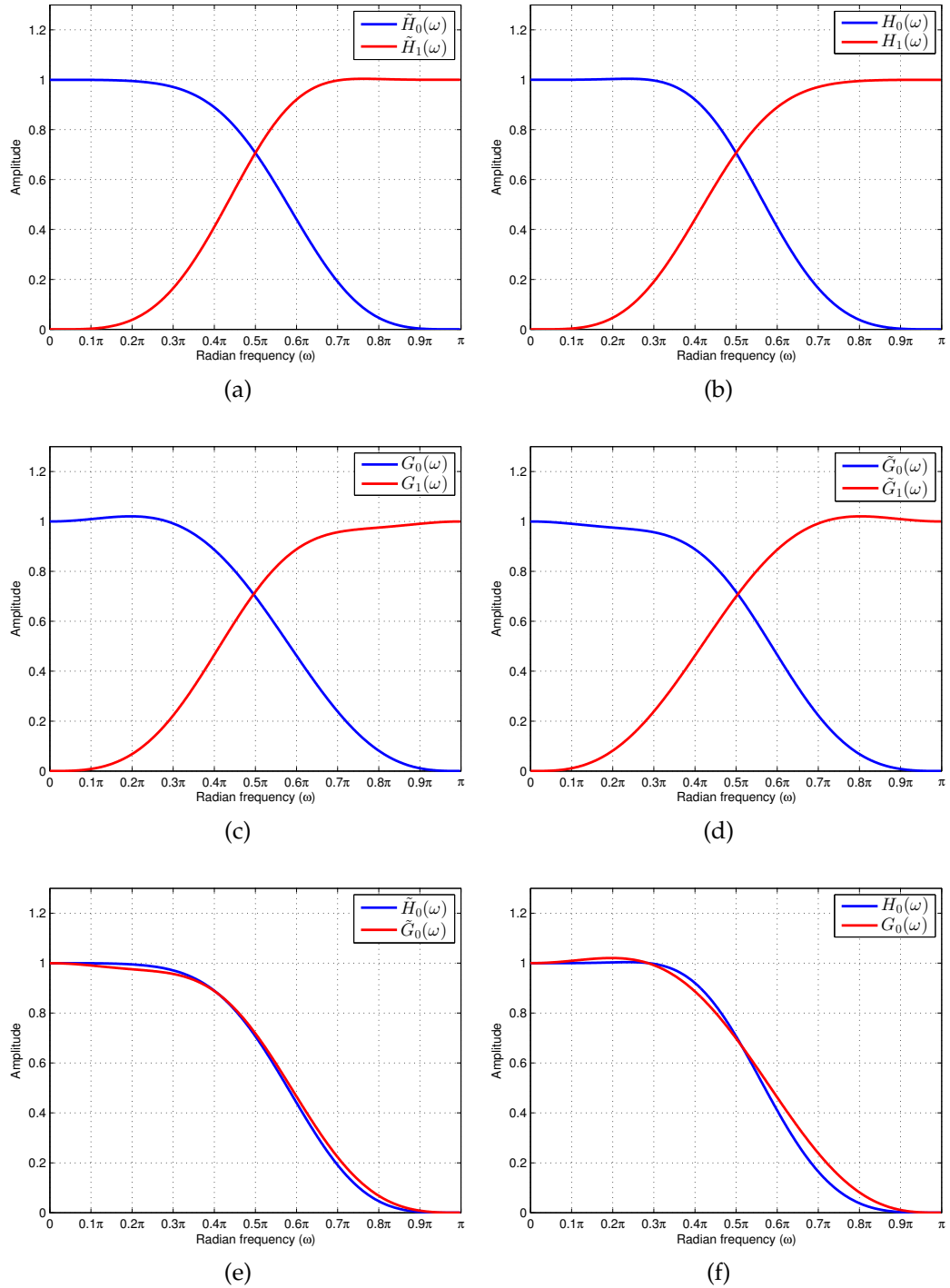
Figure 4.12: Magnitude responses for Example-7 (stage-1) (a) Tree-1: analysis lowpass and highpass filters i.e., $|\tilde{H}_0(\omega)|$ and $|\tilde{H}_1(\omega)|$ (b)Tree-1: synthesis lowpass and highpass filters i.e., $|H_0(\omega)|$ and $|H_1(\omega)|$ (c) Tree-2: analysis lowpass and highpass filters i.e., $|\tilde{G}_0(\omega)|$ and $|\tilde{G}_1(\omega)|$ (d)Tree-2: synthesis lowpass and highpass filters i.e., $|G_0(\omega)|$ and $|G_1(\omega)|$ (e) comparison between analysis lowpass filters of Tree-1 and Tree-2 i.e., $|\tilde{H}_0(\omega)|$ and $|\tilde{G}_0(\omega)|$ (f)comparison between synthesis lowpass filters of Tree-1 and Tree-2 i.e., $|H_0(\omega)|$ and $|G_0(\omega)|$.

Fig. 4.12(f) compare the magnitude responses of the analysis and synthesis low-pass filters of Tree-1 and Tree-2, respectively. It is clear that although responses match fairly well there is still scope for improvement, which motivated us to have second shape-parameter optimization stage. Fig. 4.11 shows plots of analysis and synthesis wavelet functions for first stage filters obtained in Example-7. It
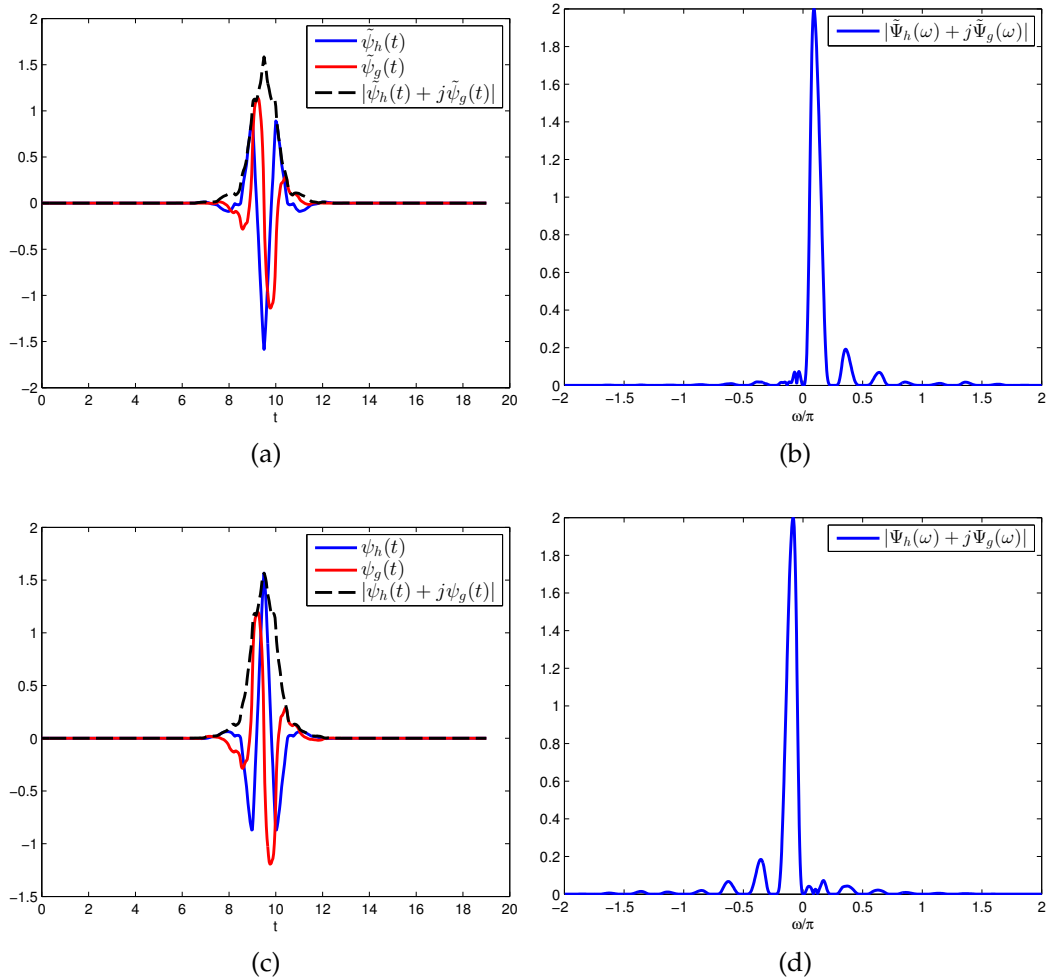
Figure 4.11: Plots for Example-7 (stage-1) (a) Analysis wavelet functions $\tilde{\psi}_h(t)$, $\tilde{\psi}_g(t)$ and $|\tilde{\psi}_h(t) + j\tilde{\psi}_g(t)|$ (b) Magnitude frequency spectrum for $|\tilde{\Psi}_h(\omega) + j\tilde{\Psi}_g(\omega)|$ (c) Synthesis wavelet functions $\psi_h(t)$, $\psi_g(t)$ and $|\psi_h(t) + j\psi_g(t)|$ (d) Magnitude frequency spectrum for $|\Psi_h(\omega) + j\Psi_g(\omega)|$.

is clear from the frequency spectrum plots given in Figs. 4.11(b) and 4.11(d) that they are approximately zero for $\omega < 0$ and $\omega > 0$, respectively. Thus, their corresponding analysis/synthesis wavelet functions of both the trees shown in Figs. 4.11(a) and 4.11(c) are approximately Hilbert transform pairs of each other.

To improve the analyticity of the wavelet functions of desired filters, we use second stage by using shape-parameter optimization of the Tree-1 filters. That is we obtain optimized Tree-1 filters for better analyticity. During the optimization, different combinations of lengths of halfband filters are considered to obtain the optimum filter coefficients. For $N_0 = N_1 = 2$, $N_2 = 1$ and $p = 0.4327$ combination, objective function in equation (4.41) was *minimum*. Optimized Tree-1 filters $\tilde{h}_0(n)$ and $h_0(n)$ are of lengths 13 and 15, receptively. Their filter coefficients are given in Table 4.11. Figure 4.13 shows magnitude response comparison between lowpass filters of the newly optimized Tree-1 and the proposed Tree-2 filters. It is clear that magnitude response approximation is much better in this case. Also, the visual quality of the analyticity of wavelet bases looks much better than the first stage filters. Analytic quality of wavelets obtained using stage-1 and stage-2 filters is tabulated in Table 4.13 and it is clear that stage-2 optimization improves analytic quality quantitatively as well. In Table 4.13, we have also compared results of this example with the design examples given in state-of-the-art odd-even matching techniques [134][95]. One can see that, wavelets obtained for filters of Example-7 have analyticity comparable to these methods which use constrained optimization and are computationally expensive.

Finally, we compare the results obtained using this approach to our first approach based on vanishing moments criteria where we consider same number of vanishing moments for the scaling filters of Tree-1. As the wavelet functions for Example-7 (stage-2) are obtained using $\tilde{K} = 4$ and $K = 2$, the filters of HSD-based approach are obtained using $\tilde{K} = 4$, $K = 2$, $L = 2$ and $n_f = 1$ referred as Example-8 filters. The lengths of the filters obtained are 17 and 11, respectively with their coefficients tabulated in Table 4.12. Analyticity measures for the wavelets obtained using these filters are given Table 4.13. One can see that analyticity measures for the wavelets obtained using both Example-7 (stage 2) and Example-8 filters are similar. However, using the proposed HSD-based method we only need to design the either of the tree filters which is beneficial when considering the multiplier-less implementation of DTCWT [3][107]. The disadvantage is that these filters have approximate linear phase characteristics. Whereas,

Table 4.11: Optimized coefficients of $\tilde{h}_0(n)$ and $h_0(n)$ after shape-parameter optimization stage.

n	$\tilde{h}_0(n)$	$h_0(n)$
1	-0.0008	-0.0002
2	0.0000	0.0000
3	0.0152	0.0028
4	-0.0312	0.0062
5	-0.0532	-0.0264
6	0.2812	-0.0495
7	0.5777	0.2737
8	0.2812	0.5866
9	-0.0532	0.2737
10	-0.0312	-0.0495
11	0.0152	-0.0264
12	0.0000	0.0062
13	-0.0008	0.0028
14	-	0.0000
15	-	-0.0002

Table 4.12: Coefficients of the Example-8 filters.

n	$\tilde{h}_0(n)$	$h_0(n)$
1	0.0000	0.0001
2	-0.0001	0.0007
3	-0.0018	-0.0139
4	0.0087	-0.0671
5	0.0180	0.1698
6	-0.0541	0.5676
7	-0.0081	0.3898
8	0.3854	0.0007
9	0.5516	-0.0465
10	0.1688	-0.0020
11	-0.0802	0.0007
12	-0.0079	0.0000
13	0.0210	0.0000
14	-0.0009	0.0000
15	-0.0006	0.0000
16	0.0000	0.0000
17	0.0000	0.0000

Table 4.13: Analytic quality comparison of the 1st and 2nd stage filters obtained using the proposed matching technique

	E_1_A	E_2_A	E_1_S	E_2_S	E_1_Avg	E_2_Avg
Example-7 (Stage-1)	0.0372	0.0010	0.0360	0.0017	0.0366	0.0014
Example-7 (Stage-2)	0.0198	**0.0004**	**0.0184**	**0.0004**	**0.0191**	**0.0004**
Table I of [134]	0.0222	0.0007	0.0328	0.0008	0.0275	0.0007
Table III of [95]	0.0202	0.0008	0.0242	0.0004	0.0222	0.0006
Example-8	**0.0186**	0.0007	0.0207	0.0005	0.0196	0.0006
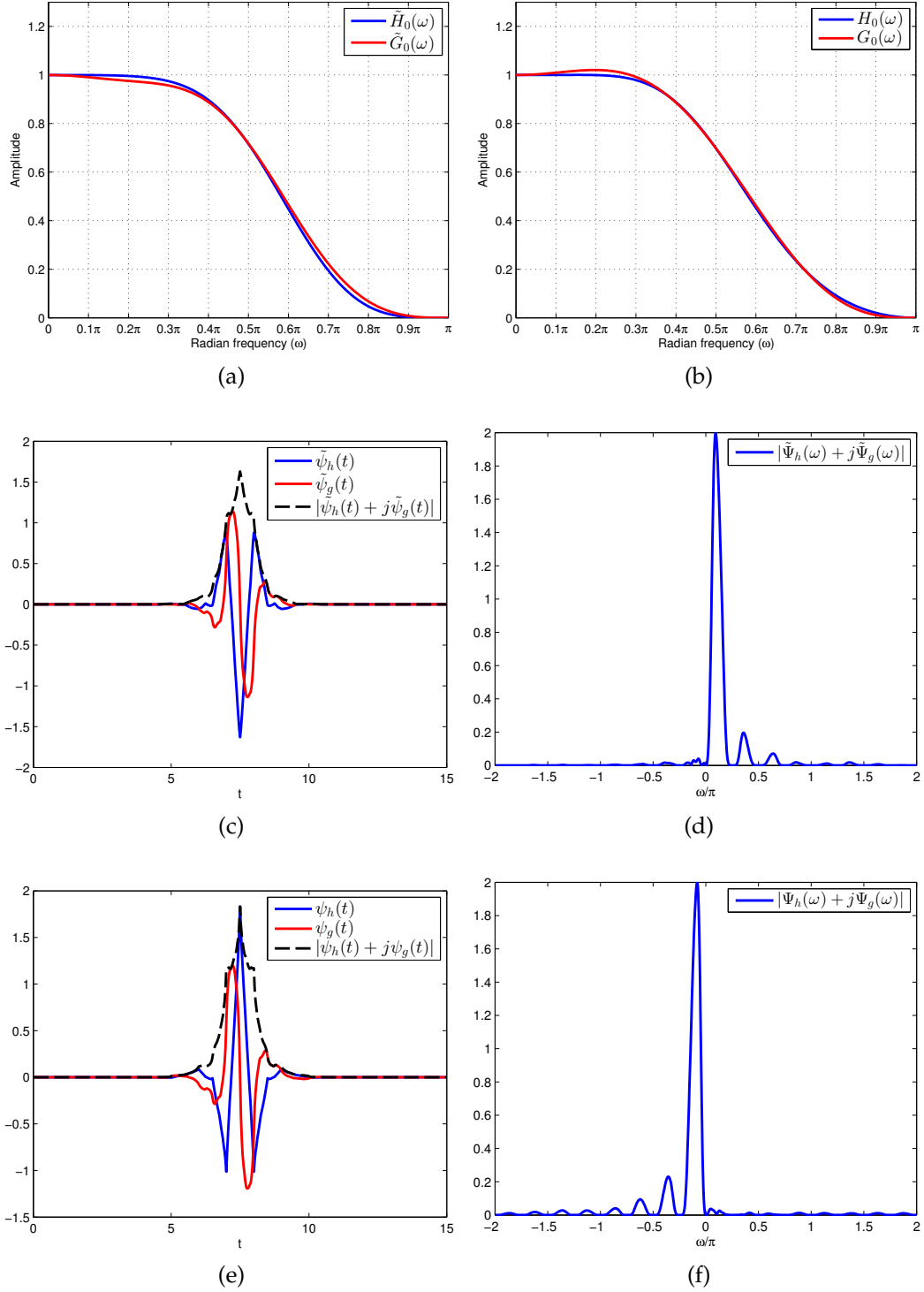
Figure 4.13: Plots for Example-7 (stage-2) (a) magnitude response comparison between analysis lowpass filters of Tree-1 and Tree-2 i.e., $|\tilde{H}_0(\omega)|$ and $|\tilde{G}_0(\omega)|$ (b)magnitude response comparison between synthesis lowpass filters of Tree-1 and Tree-2 i.e., $|H_0(\omega)|$ and $|G_0(\omega)|$. (c) Analysis wavelet functions $\tilde{\psi}_h(t)$, $\tilde{\psi}_g(t)$ and $|\tilde{\psi}_h(t) + j\tilde{\psi}_g(t)|$ (d) Magnitude frequency spectrum for $|\tilde{\Psi}_h(\omega) + j\tilde{\Psi}_g(\omega)|$ (e) Synthesis wavelet functions $\psi_h(t)$, $\psi_g(t)$ and $|\psi_h(t) + j\psi_g(t)|$ (f) Magnitude frequency spectrum for $|\Psi_h(\omega) + j\Psi_g(\omega)|$.

proposed odd-even approach is quite useful if exact linear-phase of filters and exact symmetry of wavelets is desirable.

4.5   Image Denoising Application

In this section, we show the performance of one of the DTCWT biorthogonal wavelet filter set for the image denoising application. For this purpose, we have chosen output stage-2 filters of the Example-7 designed in the previous section. Coefficients of the analysis and synthesis lowpass filters of the chosen set for Tree-1 and Tree-2 are given in Tables 4.11 and 4.10, respectively. We use these filters to obtain the 2-D DTCWT by using the construction given [92]. Six 2-D oriented six wavelets obtained for the chosen filter set are shown in Figure 4.14. Here, the first and second rows correspond to the real and imaginary parts of each complex wavelet while third row corresponds to the magnitude parts of the same.
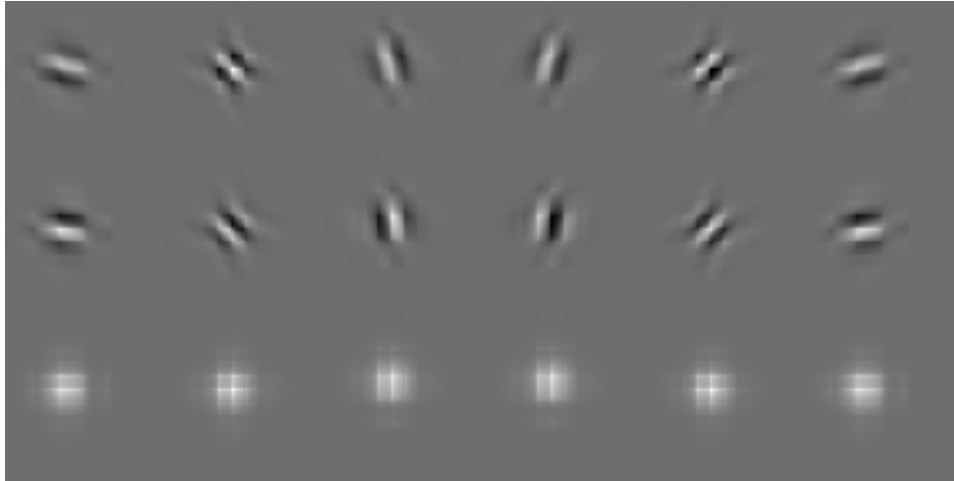
Figure 4.14: 2D Dual-Tree Complex Wavelets for the proposed biorthogonal wavelet filters of the chosen filter set.

For comparing the image denoising performance we have used the MATLAB software provided by Ivan W. Selesnick on his website [89]. We have compared our results with their 2-D DTCWT given for the best performing filters namely 6-tap orthogonal Q-shift filters of [52]. Additive white Gaussian noise (AWGN) of standard deviation σ is added to the original image in order to test the performance of our proposed designs on noisy images. We have used *hard thresholding*

method [30] with a threshold value of $T = 2\sigma$ as used in the DTCWT software mentioned above. Figure 4.15 shows hard thresholding results on a part of Barbara image containing oriented texture for AWGN of standard deviation $\sigma = 30$.

(a)   (b)

(c)   (d)
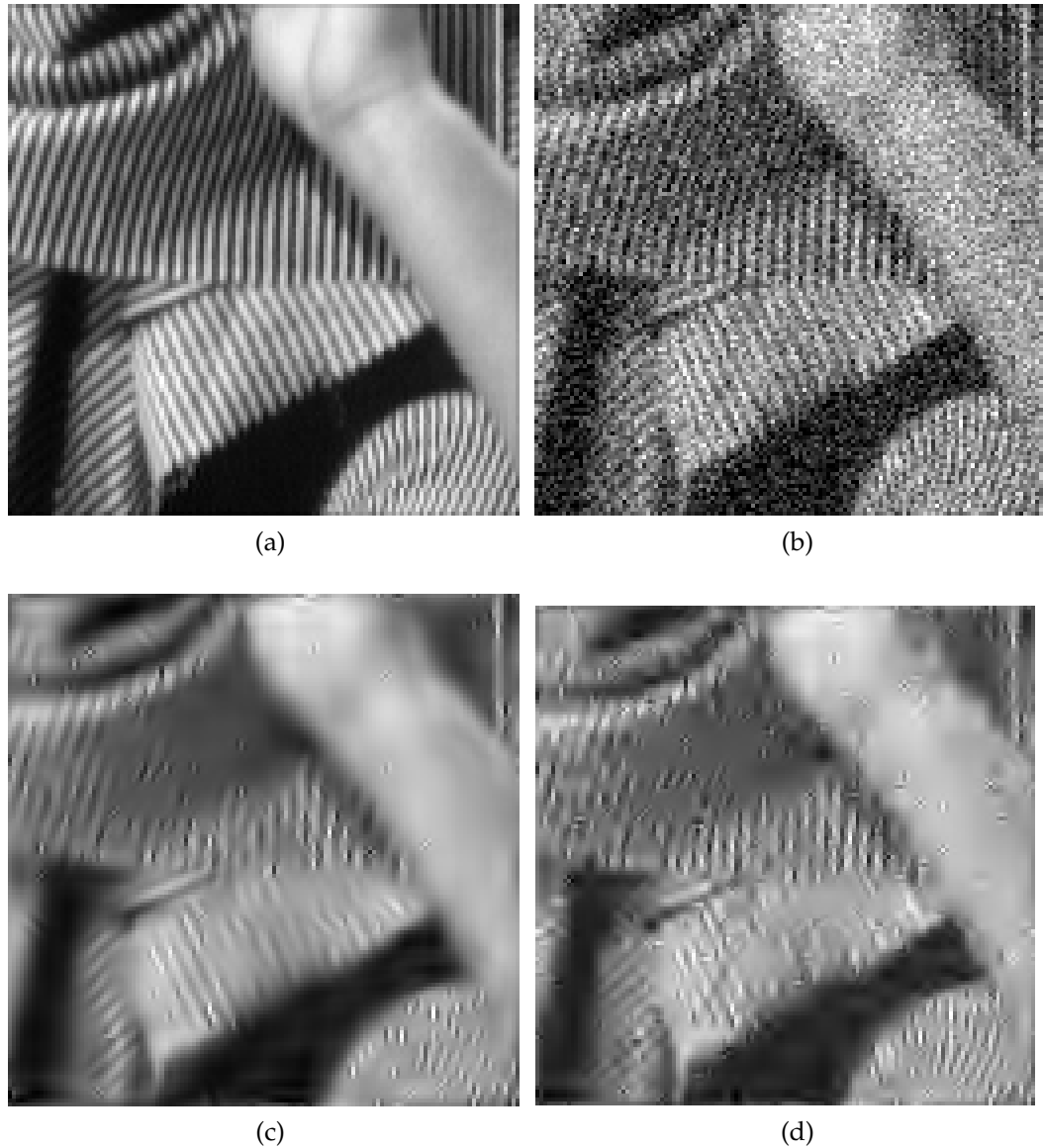
Figure 4.15: Image denoising using 2-D DTCWT (a) original image (b) noisy image with $\sigma = 30$, PSNR = 18.72 dB. Denoising using (c) 6-tap orthogonal Q-shift filters of [52], PSNR = 23.35 dB. (d) for the proposed biorthogonal wavelet filters of the chosen filter set, PSNR = 23.23 dB.

It can be observed that the 2-D DTCWT obtained using proposed BWFs of the chosen set performs comparably to that of best known orthogonal 6-tap Q-shift filters of [52] in terms of PSNR value. Denoising output shown in Figure 4.15(c)

for Q-shift filters have slightly better visual performance when compared to the output for proposed BWFs of the chosen filter set shown in Figure 4.15(d). However, directional features are better captured using the proposed filters (see the textural features visible in the bottom right hand corner) due to better directional selectivity of their 2-D dual-tree directional wavelets. Better visual performance of Q-shift filters may be reasoned for their short lengths which helps in suppressing the *ringing* artifacts near the image edges.

4.6   Conclusion

In this chapter, we have proposed two new approaches to design a set of biorthogonal wavelet filters of DTCWT having near-orthogonal filter response characteristics which are useful to get tight-frame transform. The proposed approaches are based on optimization of free variables obtained through factorization of generalized halfband polynomial. Use of unconstrained optimization makes both approaches simple and computationally effective. Associated wavelets of the filters obtained using the proposed approaches have better analytic properties leading to improved shift-invariance. Image denoising performance using simple thresholding applied on the multiscale six directional suubands of the 2-D DTCWT constructed using one of the proposed filter set shows better directional selectivity and comparable performance as compared to one of the best performing orthogonal DTCWT filter set.

CHAPTER 5

Design of Extrafine Complex Directional Wavelet Transform

In chapter 4, we discussed the 1-D filter design aspect of dual-tree complex wavelet transform (DTCWT). Multidimensional (m-D) extensions of DTCWT are easy to follow and 2-D DTCWT used in image processing applications has six directional representation with redundancy factor 4 [92]. Due to its specific construction, the directionality of 2-D DTCWT cannot be improved without increase in the redundancy factor. In this chapter, we propose a new 2-D complex wavelet transform having higher directionality and lower redundancy factor than 2-D DTCWT. The proposed transform referred as *extrafine complex directional wavelet transform* (EFiCDWT) is obtained using separable and nonseparable filtering stages and has twelve directional representation with a redundancy factor of just 2.

5.1   Introduction

In recent years, *complex wavelet transforms* (CWTs) have attained a status of useful transform domain processing tool in wide range of multimedia applications such as image [85][39] and video [83] denoising, super-resolution [132][48], image fusion [125], image quality assessment [87] to name a few. For numerous other applications one can refer to [92]. The reason for their success is ascribed to their improvements in the signal representation over *discrete wavelet transform* (DWT) with reasonable redundancy. CWTs offer less oscillatory behaviour at edges and have robust edge information. Along with better directionality they exhibit near

shift-invariance and phase information is also available.

We refer [92] as an excellent comprehensive tutorial on CWTs. The most popular CWTs are those obtained using dual-tree (DT) structure of DWTs [92] which is discussed in detail in Section 4.2. As per the discussion, any DWT structure cannot be used here since the wavelets of the two trees must be approximate Hilbert transform pairs of each other and hence the scaling filters of the two DWT trees are related to each other. In 2-D DTCWT, the subband outputs of the two branches i.e., primal and dual trees are considered as the real and imaginary parts of the complex coefficient representation of an input image. These complex coefficients are approximately analytic and represent single sided directional subbands in the 2-D frequency plane. Various transforms proposed using DTCWT concept can be found in [43], [20], [15]. The 2-D CWTs can also be obtained using post/pre filtering stages to the DWT [92]. In [37], Fernandes *et. al* proposed a new projection-based framework for CWTs with controllable redundancy factor using a two stage approach. In the first stage, projection of input image onto complex function space is obtained using 1-D quasi-analytic projection filters followed by any DWT stage. Multidimensional extensions of this framework are discussed in detail in [38]. Its 2-D extended CWT has a redundancy factor of 2.67. Although, the 2-D CWTs discussed above (dual-tree and projection-based) have different redundancy factors, they can only have one lowpass and six directional subbands oriented at $15°$, $45°$, $75°$, $-75°$ (or $105°$), $-45°$ (or $135°$) and $-15°$ (or $165°$).

In this chapter, we propose decimated and undecimated designs of extrafine complex directional wavelet transform (EFiCDWT) having 12 directional subbands at each scale. In order to do this, we first propose a new 2-D mapping-based CWT which forms core of the proposed transform. It has the advantage of extensible directionality. An additional stage of 2-D complex FIR filters referred simply as *partition filters*, is used to obtain the extrafine directionality. This stage partitions the directional subbands of the proposed CWT to obtain the decimated EFiCDWT. This design has one lowpass and 12 complex-valued directional subbands with near shift-invariance. Decimated EFiCDWT has a redundancy factor of 2 because of complex nature of the coefficients ($2 * N$ real coefficients where, N:

number of image pixels). We also propose undecimated EFiCDWT which is completely shift-invariant. Both designs are useful in image processing applications such as image denoising, super-resolution etc. that require improved *directionality* and *shift-invariance* properties. The rest of the paper is organized as follows: In Section 5.2, we explain in detail the design procedures of the proposed decimated and undecimated EFiCDWT including the designs of the necessary 2-D FIR filters. In Section 5.3, we test the image denoising capability of the proposed designs using the *hard thresholding* method. Section 5.4 concludes the chapter.

5.2 Proposed EFiCDWT designs

Figure 5.1(b) shows, the 2-D frequency partition for the proposed EFiCDWT that has 12 complex-valued directional subbands. Coloured parts of the frequency plane are for complex-valued directional subbands and taking the real-part of these will cover both sides of the 2-D frequency plane. EFiCDWT partition is obtained by extrafine partitioning of the CWT-like partition shown in Figure 5.1(a). Our new approach to obtain the CWT-like partition uses real-valued highpass subbands of the *finer directional wavelet transform* (FiDWT) [63], which are mapped to approximately analytic domain by filtering them with appropriate 2-D mapping filters. Finally, extrafine directional subbands are obtained by filtering the analytic subbands using additional filter bank stage of partition filters.

5.2.1 Design of required 2-D FIR filters

The filter responses used in the proposed EFiCDWT are obtained using *transformations of variables* (TROV) [111] technique, with Cohen-Daubechies-Feauveau *CDF 9-7* as 1-D wavelet filter and using 2-D transformation kernel obtained by truncating the 2-D ideal impulse response of each filter by a 2-D window obtained from 1-D Kaiser window having parameters $L_w = 7$ and $\beta = 4.5$.

Checkerboard-shaped filters design ($H_i^{cs}(\mathbf{z}), i = 0, 1$): These are obtained using the procedure given in [111].

Mapping filters design for analytic representation: To obtain the complex 2-D
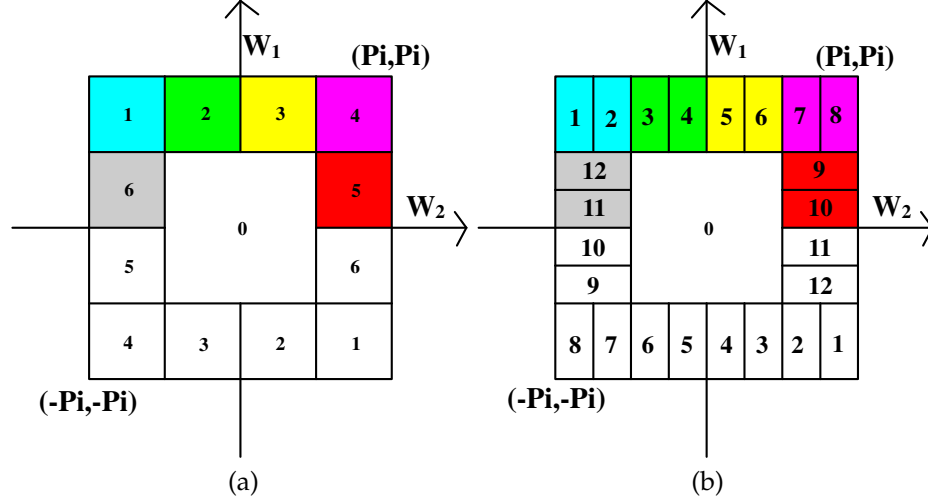
Figure 5.1: 2-D frequency partitions of (a) new mapping-based CWT (b) proposed EFiCDWT Here, Pi in the figure represents π.

frequency partition shown in figure 5.1(a), we need to design the analytic mapping filters which will filter the real-valued directional subbands of the FiDWT to obtain CWT-like representation. Ideal magnitude responses of the desired mapping filters are

$$
\begin{aligned}
H_0^m(\boldsymbol{\omega}) &= 0, \ \ \text{for} \ \ \omega_1 \in [-\pi, 0], \ \ \omega_2 \in [-\pi, \pi] \\
H_1^m(\boldsymbol{\omega}) &= 0, \ \ \text{for} \ \ \omega_1 \in [0, \pi], \ \ \ \ \omega_2 \in [-\pi, \pi]
\end{aligned}
\tag{5.1}
$$

However, this is not possible in practise. Hence a quasi (approximate) analytic mapping filter is obtained using TROV, with ideal impulse response as,

$$
r^m(\mathbf{n}) = jsinc\left(\frac{n_1\pi}{2}\right) sinc\left(n_2\pi\right) sin\left(\frac{n_1\pi}{2}\right).
\tag{5.2}
$$

Design of partition filters: We propose a class of special 2-D complex FIR filters which are obtained by shifting the 2-D nonseparable rectangular-shaped filters in the frequency domain. The rectangular shaped filters have passband support in $[-0.5\pi, 0.5\pi]$. In the proposed filters, the positive passband edge (at 0.5π) is shifted arbitrarily at any cut-off between $[-\pi, \pi]$ along ω_1 or ω_2 axes with same passband support size. The generalized ideal impulse response equations for de-

signing filters having passband edge along ω_2 axis are,

$$r^{c_2}(\mathbf{n}) = sinc\left(\frac{n_1\pi}{2}\right) sinc\left(n_2\pi\right) \exp(-j\pi(0.5 - C_f)n_1) \tag{5.3}$$

$$r^{c_2}(\mathbf{n}) = sinc\left(\frac{n_1\pi}{2}\right) sinc\left(n_2\pi\right) \exp(j\pi(0.5 + C_f)n_1). \tag{5.4}$$

Here C_f is any cut-off frequency number between $[-1,1]$. For $C_f \geq 0$ equation (5.3) is used else equation (5.4) is used. Similarly, generalized ideal impulse response equations for designing filters having passband edge along ω_1 axis are,

$$r^{c_1}(\mathbf{n}) = sinc\left(\frac{n_2\pi}{2}\right) sinc\left(n_1\pi\right) \exp(-j\pi(0.5 - C_f)n_2)$$

$$r^{c_1}(\mathbf{n}) = sinc\left(\frac{n_2\pi}{2}\right) sinc\left(n_1\pi\right) \exp(j\pi(0.5 + C_f)n_2). \tag{5.5}$$

Figure 5.2 shows the typical analysis lowpass frequency responses of the designed filters.
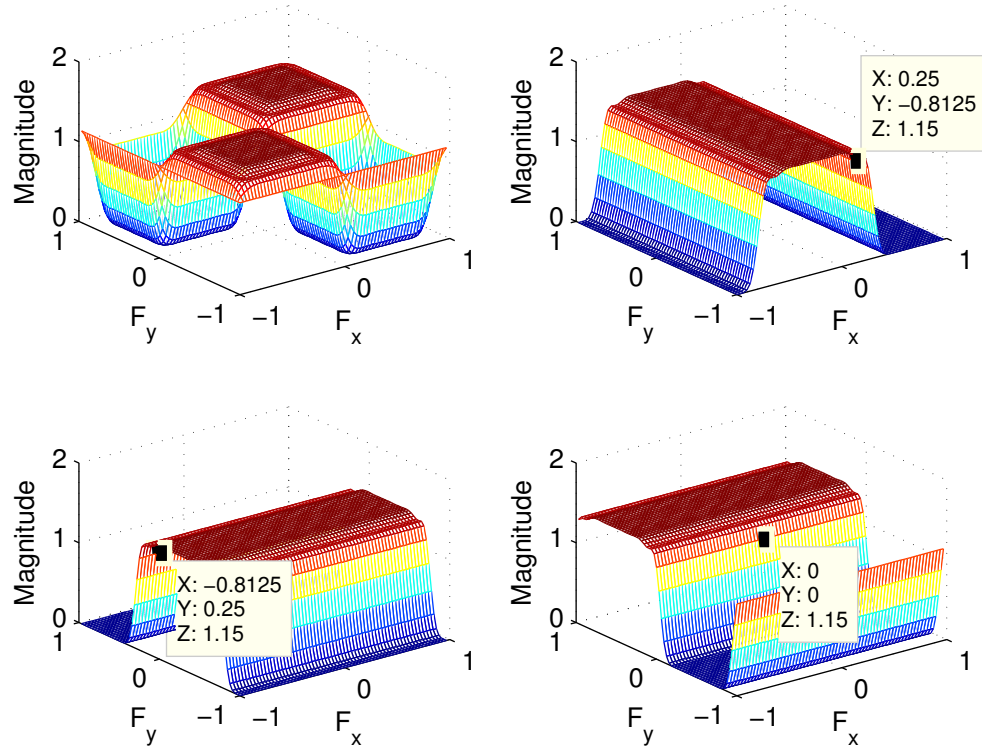
Figure 5.2: Magnitude responses of analysis lowpass filters designed using TROV with $L_w = 7$ and $\beta = 4.5$. Starting from upper-left corner $H_0^{cs}(\mathbf{z})$, $H_0^{c_2}(\mathbf{z})$ ($C_f = 0.25$), $H_0^{c_1}(\mathbf{z})$ ($C_f = 0.25$) and $H_0^m(\mathbf{z})$.

5.2.2 Proposed decimated EFiCDWT design

Figure 5.3 shows the analysis section of the proposed decimated EFiCDWT design for one level decomposition. The 2-D DWT is shown as a 4-channel filter bank
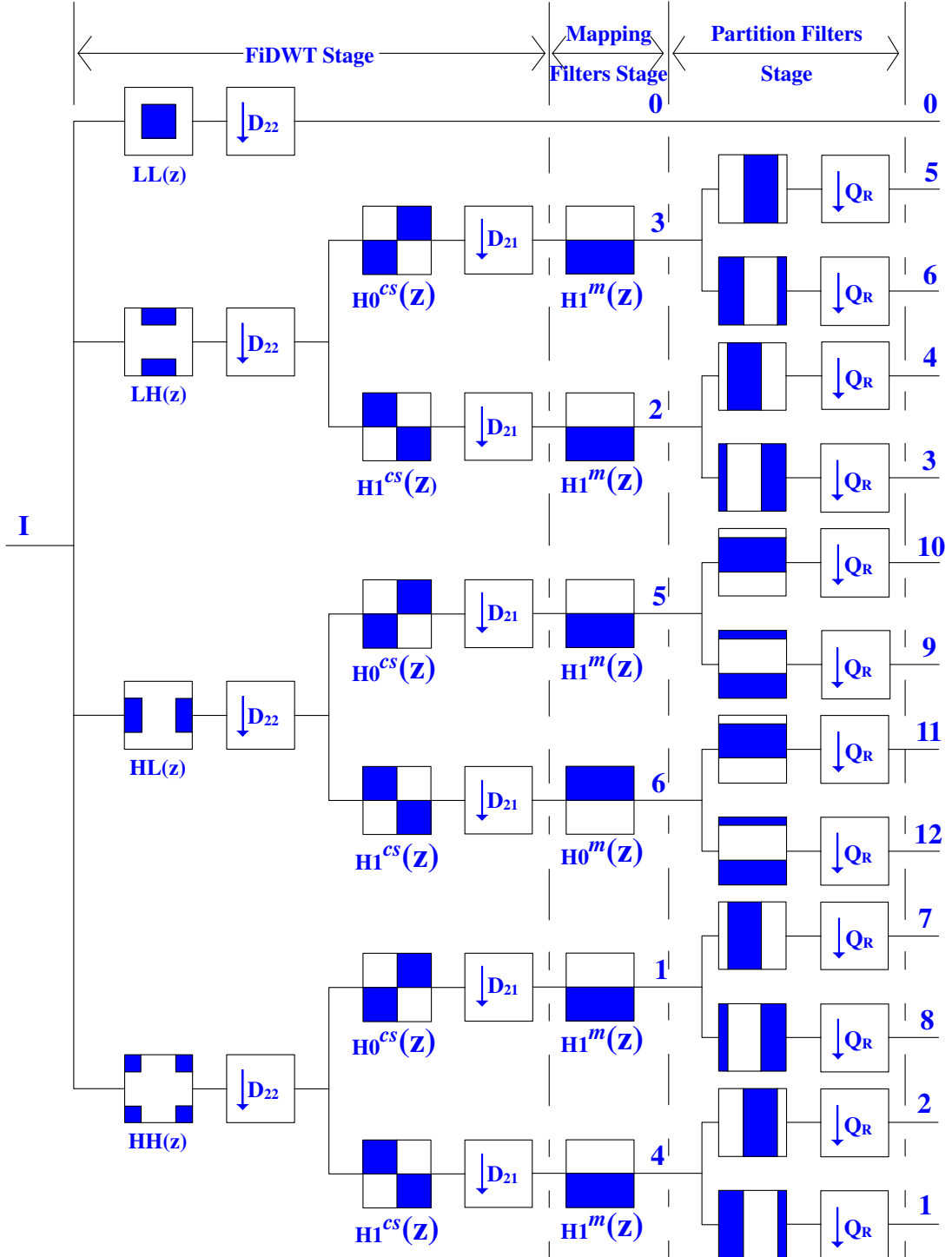
Figure 5.3: Analysis side of the proposed decimated EFiCDWT.

with 2-D filters obtained using the 1-D filters along the horizontal and vertical directions. Using z-transform, they can be represented as

$$
\begin{aligned}
LL(\mathbf{z}) &= H_0^{1D}(z_1)H_0^{1D}(z_2); \quad LH(\mathbf{z}) = H_0^{1D}(z_1)H_1^{1D}(z_2); \\
HL(\mathbf{z}) &= H_1^{1D}(z_1)H_0^{1D}(z_2); \quad HH(\mathbf{z}) = H_1^{1D}(z_1)H_1^{1D}(z_2)
\end{aligned}
\tag{5.6}
$$

where, $H_i^{1D}(z_1)$ and $H_i^{1D}(z_2)$ $(i = 0, 1)$ are the 1-D filter responses used for filtering the input image $\mathbf{I}$ along horizontal (row-wise) and vertical (column-wise) directions, respectively. Vertical (LH), horizontal (HL) and diagonal (HH) subbands of the 2-D discrete wavelet transform (DWT) are followed by decimated 2-channel checkerboard shaped filter bank (CSFB) to get the finer directional wavelet transform (FiDWT) [63]. The six highpass directional subbands of the FiDWT have the orientation selectivity of 75°, 105°, 15°, 165°, 45° and 135°, respectively and have the z-transform representation as,

$$
\begin{aligned}
H^3(\mathbf{z}) &= LH(\mathbf{z})H_0^{cs}(\mathbf{z}^{\mathbf{D_{22}}}); \quad H^2(\mathbf{z}) = LH(\mathbf{z})H_1^{cs}(\mathbf{z}^{\mathbf{D_{22}}}); \\
H^5(\mathbf{z}) &= HL(\mathbf{z})H_0^{cs}(\mathbf{z}^{\mathbf{D_{22}}}); \quad H^6(\mathbf{z}) = HL(\mathbf{z})H_1^{cs}(\mathbf{z}^{\mathbf{D_{22}}}); \\
H^1(\mathbf{z}) &= HH(\mathbf{z})H_0^{cs}(\mathbf{z}^{\mathbf{D_{22}}}); \quad H^4(\mathbf{z}) = HH(\mathbf{z})H_1^{cs}(\mathbf{z}^{\mathbf{D_{22}}}).
\end{aligned}
\tag{5.7}
$$

Here $\mathbf{D_{22}} = diag(2,2)$ is downsampling matrix for DWT and $\mathbf{D_{21}} = diag(2,1)$ is downsampling matrix for 2-channel checkerboard-shaped filter bank. Note that being critically sampled, number of directional subbands and directional selectivity of the FiDWT is similar to that of CWT. However it suffers from aliasing effects [69] due to nonideal passbands of the CSFB filters. On the other hand the CWT having phase information, posses near-shift invariance property and the coefficients are less oscillatory at edges. Since real-part 2-D frequency partition of CWT is same as that of FiDWT, we can easily obtain it from FiDWT subbands with proper filtering stages. We filter each of the real-valued directional subbands of FiDWT by an appropriate quasi-analytic filter to obtain the CWT-like directional subbands i.e., frequency response of any directional subband exists on positive side of the origin of ω_2 axis as shown in Figure 5.1(a).

Our approach for obtaining the CWT-like 2-D frequency partition is motivated

by the works [16] [37]. In [16], Bernard used the post-filtering stage on the real-valued highpass subbands of the DWT using *almost analytic* 1-D wavelets to obtain analytic DWT and applied the same for optical flow estimation. In [37], Fernandes used the prefiltering by 1-D quasi-analytic projection filters to get the 2-D CWT. Our approach uses the 2-D quasi-analytic mapping filters designed in section 5.2.1 to filter the real-valued subbands of the FiDWT to get 2-D CWT-like representation shown in Figure 5.1(a). The mapping filters designed using TROV [111], $H_j^m(\mathbf{z}), j = 0, 1$ are used appropriately as shown in Figure 5.3 to get the six complex directional subbands $H^i(\mathbf{z})$, where $i = 3, 2, 5, 6, 1, 4$.

Considering the flexibility of additional directionality offered by our new mapping-based CWT, we use a decimated 2-channel filter bank with new generalized partition filters $(H_i^{C_j}, i = 0, 1$ and $j = 1, 2)$ with specific normalized cut-off frequency (C_f) to add *extra* directionality to the complex directional subbands of the proposed CWT. The complex directional subband 3 $(H^3(\mathbf{z}))$ is decomposed using 2-channel filter bank with partition filters $H_i^{C_2}(\mathbf{z})$ with $C_f = -0.25$. Similarly, the remaining subbands are decomposed as:

$$\text{subband } 2 \text{ using } H_i^{C_2}(\mathbf{z}) \text{ with } C_f = 0.25,$$

$$\text{subband } 5 \text{ using } H_i^{C_1}(\mathbf{z}) \text{ with } C_f = -0.25,$$

$$\text{subband } 6 \text{ using } H_i^{C_1}(\mathbf{z}) \text{ with } C_f = -0.25,$$

$$\text{subband } 1 \text{ using } H_i^{C_2}(\mathbf{z}) \text{ with } C_f = 0.75,$$

$$\text{subband } 4 \text{ using } H_i^{C_2}(\mathbf{z}) \text{ with } C_f = -0.75.$$

These designed *partition filters* used here as mentioned in section 5.2.1 are obtained by appropriately shifting the 2-D rectangular-shaped filters in the frequency domain along ω_1 or ω_2 axis. The passband support of the rectangular filters have alias-free decimation for the quincunx downsampling matrix $\mathbf{Q}$ [115]. This is because of the nonuniqueness of the possible passband supports generated by the quincunx decimation matrix which can have alias-free decimation as elaborated in Figure 12.5-4 of [115]. Hence the designed class of partition filters obtained merely by *frequency shifting* of the rectangular-shaped filters in the frequency do-

main have alias-free decimation for matrix $\mathbf{Q}$. We obtain the 12 directional sub-bands from the 6 complex directional subbands of the proposed CWT-like transform by filtering each of this subband by a 2-channel decimated filter bank with partition filters and downsampling matrix $\mathbf{Q_R}$ used in [33] to have square output subbands. Here, $\mathbf{Q_R} = \mathbf{Q} * \mathbf{R} = \begin{bmatrix} 1 & -1 \\ 1 & 1 \end{bmatrix} * \begin{bmatrix} 1 & 0 \\ -1 & 1 \end{bmatrix}$ where, $\mathbf{Q}$ is a quincunx downsampling matrix and $\mathbf{R}$ is the vertical resampling matrix. $\mathbf{R}$ used to get the square output subbands from the horizontally rectangular subbands of the proposed CWT resulted by decimation matrix $\mathbf{D_{21}}$ used in FiDWT stage. Similarly, synthesis side of the proposed decimated EFiCDWT design (not shown) can be obtained by using all the filter bank stages present on the analysis side. These are arranged in the reverse order where analysis filters and downsamplers are replaced by appropriate synthesis filters and upsamplers, respectively. Filtered outputs of the 2-channel filter banks are combined using adders appropriately to obtain the reconstructed image $\hat{\mathbf{I}}$ as the final output.

The proposed decimated EFiCDWT have perfect reconstruction property with one lowpass and 12 directional subbands. Due to complex coefficients it has redundancy factor of only 2. To the authors best knowledge, no complex wavelet transform has these properties with such a low redundancy factor. Figure 5.4 shows one level decomposition of the *Cameraman* image using DWT and decimated EFiCDWT (real-part).

5.2.3 Undecimated EFiCDWT design

Since the proposed decimated EFiCDWT has near shift-invariance property it can be useful in applications such as image denoising, super-resolution etc. However, complete shift-invariance guarantees an improved performance in case of image denoising [23]. Undecimated EFiCDWT can be easily obtained from the decimated counterpart by removing all the downsamplers. Undecimated wavelet transform (UWT) is used instead of DWT followed by undecimated CSFB and mapping stage to get undecimated version of the proposed CWT. Then the 2-channel undecimated filter bank with specially designed partition filters are used
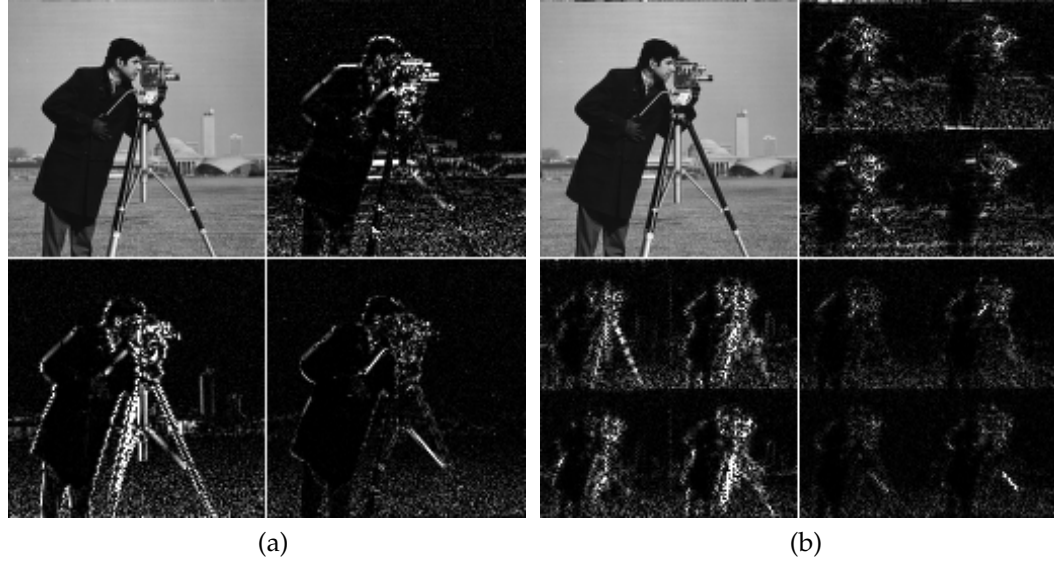
Figure 5.4: One level decomposition of Cameraman image using (a) DWT (b) proposed decimated EFiCDWT (real-part).

to get the completely shift-invariant directional representation with 12 directions. The 2-D nonseparable filter responses used must satisfy the *Bezout* identity [23] in order to get the perfect reconstruction. To satisfy this identity, we divide the impulse responses of the designed filters by $\sqrt{2}$. The complex extensions to undecimated transforms offers many advantages such as extra directional flexibility due to single sided frequency partition, less constraints on filter design, phase information etc. at the expense of high redundancy. Such transforms can be beneficial for applications where transform redundancy is secondary.

5.3 Image Denoising Application

In this section, we test the image denoising capability of the proposed decimated and undecimated EFiCDWT (DEFiCDWT and UEFiCDWT) designs using *hard thresholding* method [30]. We compare decimated EFiCDWT denoising performance with that of DWT, FiDWT [63], DTCWT [92]. For DTCWT denoising, we have used the MATLAB software provided by Ivan W. Selesnick on his website [89]. While undecimated EFiDWT is compared with UWT, undecimated finer directional wavelet transform (UFiDWT) [69]. Three levels of decomposition of all

transforms is used. *Sym8* wavelet filter is used for all DWT and UWT decompositions. Additive white Gaussian noise (AWGN) of standard deviation σ is added to the original image in order to test the performance of our proposed designs on noisy images. A value of $T = 3\sigma$ is used for thresholding DWT, FiDWT, UFiDWT transforms. Threshold $T = 2\sigma$ is used in DTCWT software mentioned above, we use the same threshold for thresholding proposed DEFiCDWT and UEFiCDWT. In case of EFiCDWT, UEFiCDWT and DTCWT, both real and imaginary parts are thresholded to obtain final denoised image.

Figure 5.5 shows hard thresholding results on a part of Barbara image containing oriented texture for AWGN of standard deviation $\sigma = 30$. Figure 5.6(a) and 5.6(b) shows PSNR comparisons of the decimated and undecimated transforms, respectively under different noise levels.

Proposed DEFiCDWT design shows improvement in denoising performance over DWT, FiDWT and DTCWT, while UEFiCDWT design performs better in terms of *peak signal-to-noise ratio* (PSNR) value and has less visual artifacts in the denoised image while preserving the oriented textural features. Table 5.1 shows comparison in terms of PSNR, *structural similarity index measure* (SSIM) [131] and *feature similarity index measure* (FSIM) [135] values of the hard-thresholded denoised images using the mentioned transforms on two widely used images *Barbara* and *Lena*. For both these images, the proposed designs shows PSNR improvement while preserving geometrical features of the original image (evident from better SSIM and FSIM values). Although the denoising results of the proposed DEFiCDWT don't supersede to that of DTCWT, however it has comparable performance with UWT which is $3 * J + 1$ (*J*:number of levels of decomposition) redundant transform. While proposed DEFiCDWT achieve this performance at redundancy factor (RF) of only 2. It is clear that UWT being a completely shift-invariant transform, its denoising performance is undermined by limited directionality. We reason the under-performance of DEFiCDWT compared to DTCWT (RF:4) because of the *aliasing* effect inherent in FiDWT explained in detail by Murugesan *et al.* in [69]. Due to nonideal passbands of the CSFB filters, the over-lapped region at the edges between DWT highpass subbands and CSFB filters
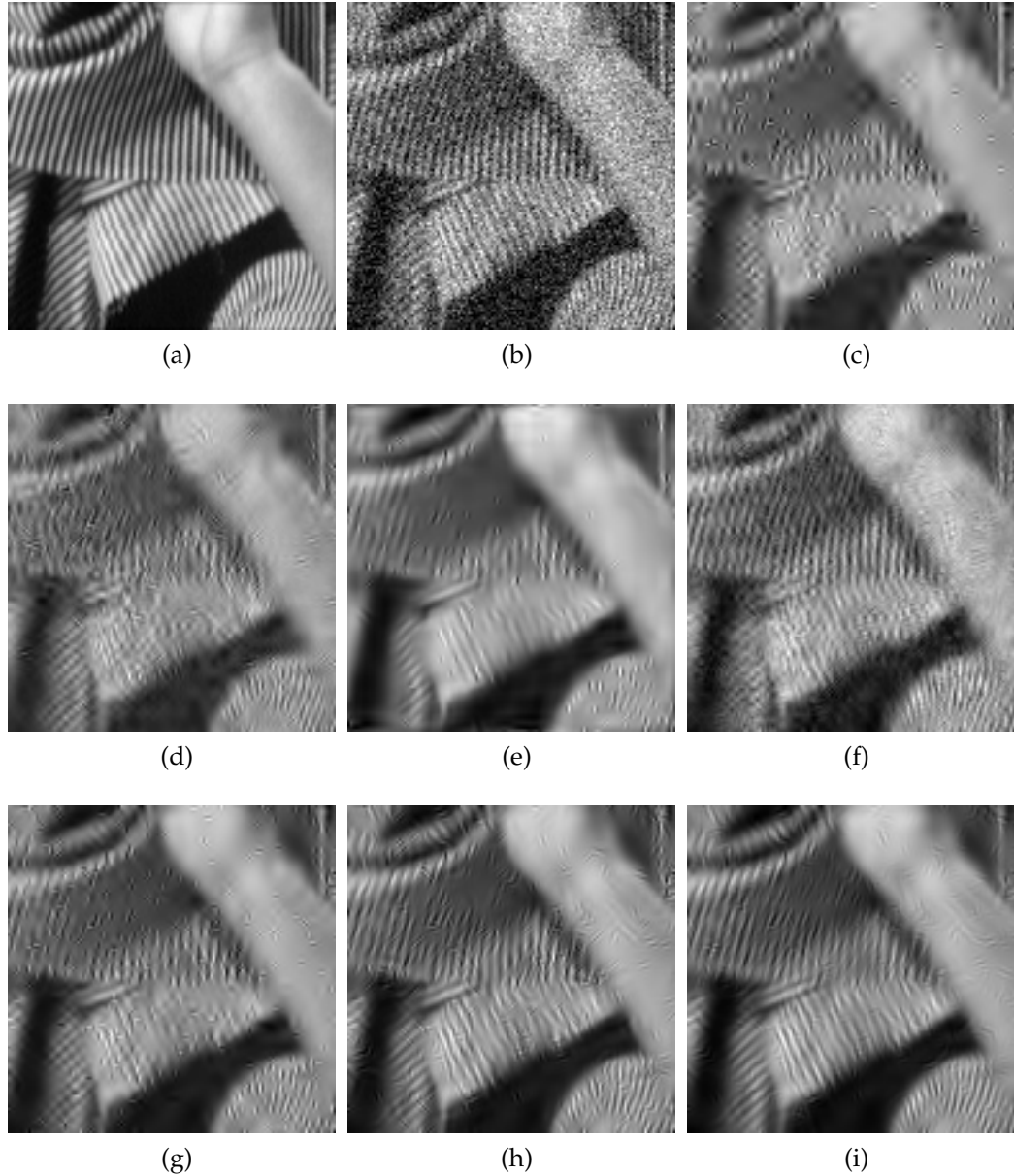
Figure 5.5: Image denoising using hard-thresholding (a) Original image (b) noisy image with $\sigma = 30$, PSNR = 18.72 dB (c) DWT, PSNR = 22.05 dB (d) FiDWT, PSNR = 22.15 dB (e) DTCWT, PSNR = 23.35 dB (f) proposed DEFiCDWT, PSNR = 23.63 dB (g) UWT, PSNR = 23.51 dB (h) UFiDWT, PSNR = 24.18 dB (i) proposed UEFiCDWT, PSNR = 24.75 dB.

cause *energy leakage*, also presence of two downsamplers lead to aliasing as well as consequential shift-variance than DWT. However it is clear from the Table 5.1 that complex and directional extension to FiDWT shows significant improvement in denoising performance i.e., better shift invariance property than FiDWT, DWT. It is clear from Figure 5.5(f) that underlying oriented textural features are better
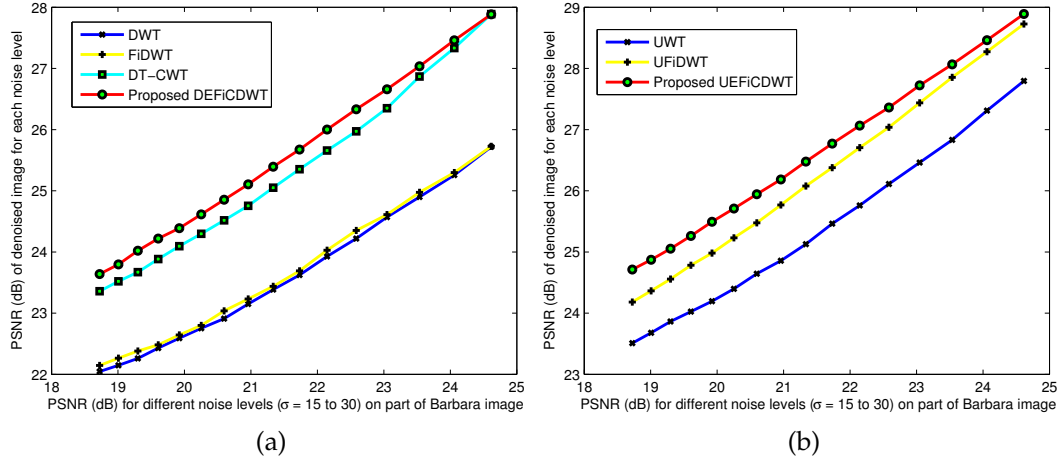
Figure 5.6: PSNR (dB) comparison of mentioned transforms under different noisy levels on the image shown in Figure 5.5(a) (a) decimated transforms (DWT, FiDWT, DTCWT and proposed DEFiCDWT) (b) undecimated transforms (UWT, UFiDWT and UEFiCDWT).

preserved by DEFiCDWT due to its *extrafine* directionality. Proposed UEFiCDWT design having extrafine directionality and completely shift-invariance shows consistent improvements in the denoising performance.

The main advantage of the proposed designs is that their directionality can be enhanced and can have computationally efficient *generalized separable* implementations. We refer to [118] as an excellent guide for computational complexities of the wavelet and filter bank designs. The DWT and UWT used in the transform have efficient separable implementations, the CSFB filter stages that use checkerboard-shaped filter responses designed using TROV method can also have efficient separable implementations as explained in [111]. All the partition filters used in the proposed designs use simple frequency shifting property on rectangular-shaped filters which further reduces the computational complexity since we just need here to design *prototype* filters (rectangular-shaped filters) which can have efficient separable implementations. One can note that the ideal impulse response equations of prototype filters are multiplications of two 1-D *sinc* functions. In comparison to DTCWT, the proposed decimated EFiCDWT has the advantage of higher directionality at lower redundancy factor. Unlike DTCWT, the proposed design structure has the advantage of extensible directionality.

Table 5.1: PSNR/SSIM/FSIM comparison of image denoising performance of mentioned transforms using hard thresholding method

σ	10			30			50		
Input PSNR/SSIM/FSIM	28.13	0.72	0.96	18.59	0.35	0.81	14.15	0.21	0.70
Transform	**Barbara** 512×512								
DWT	29.83	0.86	0.96	23.97	0.65	0.89	21.81	0.54	0.85
FiDWT [63]	29.71	0.85	0.95	24.34	0.65	0.88	22.00	0.53	0.84
DTCWT [92]	32.50	0.90	0.97	25.63	0.72	0.91	23.03	0.61	0.87
Proposed DEFiCDWT	31.29	0.87	0.97	25.25	0.68	0.90	22.82	0.57	0.86
UWT	31.96	0.90	0.98	25.47	0.71	0.92	22.92	0.58	0.88
Proposed UEFiCDWT	33.27	0.92	0.98	26.99	0.76	0.93	24.16	0.66	0.89
σ	10			30			50		
Input PSNR/SSIM/FSIM	28.13	0.61	0.95	18.59	0.22	0.79	14.15	0.12	0.67
Transform	**Lena** 512×512								
DWT	32.40	0.85	0.97	27.03	0.70	0.90	24.52	0.62	0.86
FiDWT [63]	32.00	0.84	0.96	26.79	0.67	0.89	24.33	0.57	0.85
DTCWT [92]	34.32	0.88	0.97	29.17	0.79	0.92	26.55	0.72	0.88
Proposed DEFiCDWT	32.91	0.87	0.97	27.61	0.73	0.91	25.40	0.67	0.87
UWT	34.14	0.88	0.98	28.61	0.74	0.93	25.70	0.63	0.89
Proposed UEFiCDWT	34.71	0.90	0.98	29.33	0.79	0.93	26.78	0.73	0.89

5.4   Conclusion

This chapter presented a new way of obtaining complex wavelet transform having extrafine directionality and perfect reconstruction property. This directional extensibility is achieved by filtering the real-valued subbands of the finer directional wavelet transform using novel complex-valued filter bank stages. Proposed complex wavelet transform designs having twelve directional subbands possess improved shift-invariance property. The efficacy of the transform designs are tested for image denoising application using simple subband thresholding scheme obtaining better denoising performances. The denoising results signify the advantages of the proposed direction-extensible complex wavelet transforms. The possible *generalized* separable implementations of the proposed designs make them practically tractable.

Design of Complex Adaptive Multiresolution Directional Filter Bank (CAMDFB)

All the transforms designed in the previous chapters, either by extending the directionality of DWT/UWT or by using a completely nonseparable filtering approach, have *fixed* directional image representation. Although, such transforms have been successful for most of the applications, one may desire *adaptive* directional representation for deeper analysis of the input image features. Since the transform suitability and its effectiveness depends on the application under consideration, fixed directionality may be suitable in some applications while adaptive directionality of the transform may be a sensible choice for some applications. Based on the motivations and works reviewed in Chapter 1 and the *flexibility* in direction selectivity evidenced by the use of analyticity and partition FB stage as discussed in the previous chapter, we propose in this chapter a complex-valued MDFB having image adaptive directional representation. The proposed transform effectively represents the dominant directions present in the input image *adaptively* and is obtained using nonseparable filtering based multiresolution and directional filter bank stages. We demonstrate the proposed transform efficacy using the panshaperpening application.

For the sake of completeness, we again introduce the problem and review of related filter banks in the next section.

6.1 Introduction

Natural images most often have directional information captured at various spatial resolutions and *efficient* representation of the same is a major problem in various image processing tasks such as denoising, compression, feature extraction, fusion etc. The key features in these images are *oriented geometrical structures* and the representation tool used should capture the *orientation information*. Research in the field of wavelets and filter banks has provided many useful multiscale and multidirectional transform representations for the same.

Initially, separable multidimensional extensions of the 1-D wavelet transform were applied successfully however they suffered from limited directionality. For example, 2-D discrete wavelet transform (DWT) is good at isolating the image discontinuities or edges in fixed directions. However, *edges* are often present along the smooth contours which are created by smooth boundaries of the image objects and have arbitrary orientations. Hence DWT fails to efficiently capture the *smoothness along the contour* and this has encouraged researchers to propose various 2-D nonseparable *multiresolution directional filter bank* (MDFB) designs. These MDFB designs provide multiple *directional* and *anisotropic* basis representation for image discontinuities at various resolutions. Contourlet transform proposed by Do and Vetterli [29] is one such MDFB design that captures the 2-D geometrical features of the images effectively and has been used in various image processing applications. Countourlet transform is constructed by using Laplacian pyramid stage cascaded with the directional filter bank (DFB) stage to have multiscale and multiresolution representation of input images. DFBs were first introduced by Bamberger and Smith in [14] and they have been used to develop several multiscale directional transforms [28, 34, 64]. However, Bamberger's DFBs have limited directional flexibility of 2^l in their l-level tree-structure realization. A class of nonredundant multiresolution directional filter banks (MDFBs) proposed in [71, 72] offers flexible number of directional subbands, however in this case the design of required filters is quite involved [71]. Maximal decimation in these DFB families limits their directionality and also leads to shift-variant representation

unsuitable for many specific image processing applications such as denoising and enhancement [23].

Attempts have been made to achieve near shift-invariance and improved directionality using the idea of *near-analytic* transform designs such as *complex wavelet transforms* (CWTs) [37, 38, 92] with small redundancy. Salient features of these complex transform designs are *shiftability* i.e., near shift-invariance, *increased directionality* and the availability of *phase information*. In [73], Nguyen and Oraintara proposed a shiftable complex directional transform by combining Laplacian pyramid and complex directional filter bank. Here in order to obtain the analyticity, dual-tree structure of real DFBs is constructed where the fan filters used in the trees are constrained to satisfy the Hilbert pair criteria and certain conditions on phase responses. In [74] the same authors addressed the implementation issues such as border artifacts and the constraints on the designed finite impulse response (FIR) filters. However these FIR filters correspond to truncated versions of infinite impulse response (IIR) filters and the transform is approximately shift-invariant. In [80], authors proposed complex-valued steerable filterbank for texture synthesis application and utilize the same for finding features based on local phase and energy. Although these transform designs need lower computational requirements, downsampling stages used in these designs lead to *suboptimal* performance in many image processing applications and hence limits their applicability. Downsampling stages in these transforms causes *aliasing* effect which leads to large reconstruction error, reduced directional flexibility, difficulty in filter design etc. Also it is not possible to build a *subsampled* (or downsampled) transform having arbitrary frequency partitions [61], which is a key requirement for designing an adaptive transform.

In the recent years, the nonsubsampled multiresolution transforms have attained preference in many applications such as image denoising [23][47], enhancement [60], image fusion [25],[17], etc. due to their superior performance. The multiresolution directional filter banks (MDFBs) along with the notion of *nonsubsampledness* allow flexibility in directional feature selection [61] and one can achieve increased directionality and better frequency selectivity [23]. Efficient and fast al-

gorithms such as *"algorithme à trous*" exist for implementing nonsubsampled designs. Decimation free operations lead to a completely *shift invariant* representation useful for many image processing operations. In [23] authors proposed nonsubsampled contourlet transform using the DFBs and Laplacian pyramid without decimation. They discuss the frame theoretic designs of the nonsubsampled pyramid and fan-shaped filters used in the implementation of the transform. Other notable nonsubsampled transform designs can be found in [32, 61, 65]. All the transforms discussed until now are built without considering the input image characteristics and hence *nonadaptive* in nature.

Over the past one decade, different adaptive directional lifting-based wavelet transforms have been proposed for image coding with the initial contribution from Taubman [101]. Lifting scheme was proposed by Wim Sweldens in [99] for implementing the standard DWT. Its profound success can be attributed to its in place computations, structural perfect reconstruction and nearly half of the computational requirements than the Mallat's scheme. In [27] Ding *et. al.* proposed adaptive directional lifting (ADL) based wavelet transform for image coding. Here, the subband decomposition is similar to the standard-lifting based wavelet implementation but the prediction step is performed in the direction of strongest pixel correlation in contrast to the horizontal and vertical directions in the latter. Few other related lifting-based adaptive wavelet transforms in this context can be found in [19, 42, 100, 129]. In [96], the translation invariant directional framelet transform is proposed where the local orientation information is obtained using Gabor filters. For various other adaptive image representations one can refer to [79] as an excellent review paper. Also, comprehensive coverage of numerous other transforms can be found in [28, 49].

Motivated by the aforementioned works on nonsubsampled MDFBs and CWTs, in this paper we present a simple transform design which selects *noteworthy* directional features present in the input image. In other words our design is adaptive to number of dominant directions of the input image. The design is *nonsubsampled* and desired flexibility in directional selectivity is achieved using real and complex-valued filters in simple filter bank stages.

The rest of the paper is organized as follows. In Section 6.2, we explain in detail the design of the proposed adaptive transform with all the necessary steps explained in the subsections. In Section 6.3, we discuss our CAMDFB based pansharpening approach. Experimental results are provided in Section 6.4, where we compare the performance of the proposed method with state-of-the-art approaches including transform-based methods. Finally, we conclude the work in Section 6.5.

6.2 Design of the Proposed CAMDFB

In this section, we start with the description of our fix partitioned CDFB design which constitutes the core of the proposed CAMDFB. In next subsection, we explain our design of Laplacian pyramid stage used to implement the multiresolution CDFB. We then discuss the procedure for obtaining the N number of spatially dominant directions present in the input image. Finally, partition filter bank stage following the CDFB stage is explained which completes the CAMDFB design.

6.2.1 Complex-valued directional filter bank (CDFB)

Complex-valued directional filter bank (CDFB) is at the core of the proposed CAMDFB which simplifies its design procedure. The directional selectivity of the CDFB is shown using 2-D frequency partition diagram given in Fig. 6.1. It has fix 8 directional complex-valued representation and serves to provide half-plane coarse frequency partition of the input image as shown in Fig. 6.1(a). Partition for conventional 8 directional DFB is shown in Fig. 6.1(b). Note that partition for proposed CDFB considering real-part only is same as in Fig. 6.1(b). Main advantages of the proposed CDFB representation are:

1. Since directional subbands only exist in either half-plane of the 2-D frequency partition, effects of aliasing (due to subband mixing problem caused by periodic nature of the Fourier transform) are reduced.

2. High flexibility in filter design is obtained since finer partitioning of the directional subbands is much easier due to their half-plane existence.
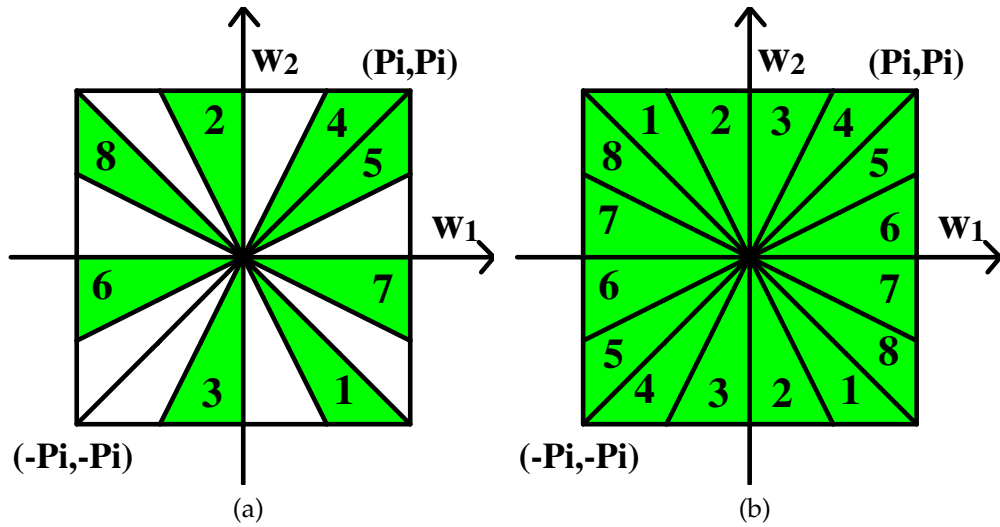
Figure 6.1: 2-D frequency partition for (a) proposed 8 directional complex-valued CDFB (b) conventional 8 directional DFB as well as for proposed CDFB with real-part only. Here ω_1 and ω_2 are frequency axes and Pi represents π.
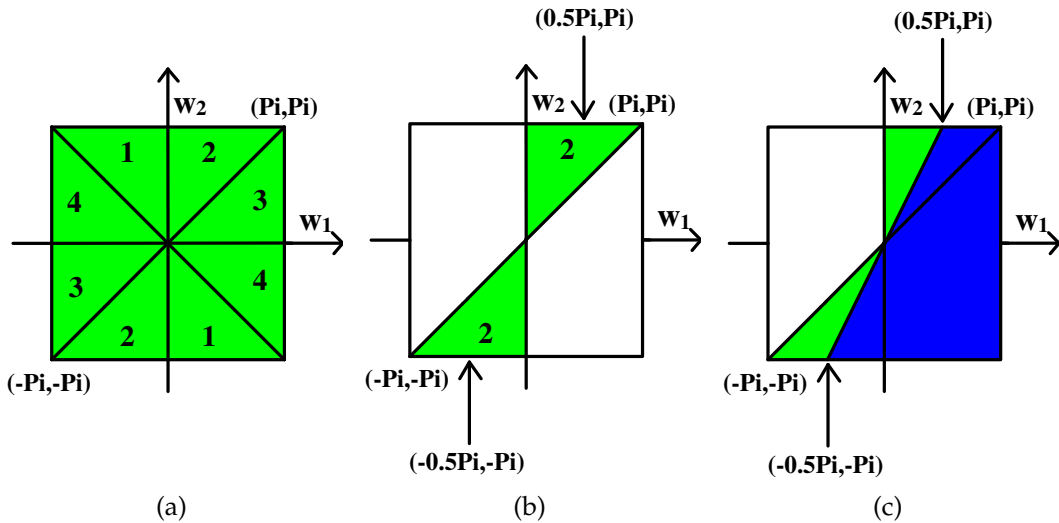
Figure 6.2: Explanation for proposed partition filters design. (a) conventional 4 directional DFB (b) Subband 2 (c) desired partition filter passband for subband 2 (denoted with blue color)

Proposed CDFB partition shown in Fig. 6.1(a) with 8 subbands is obtained by appropriately partitioning the real-valued subbands of the conventional 4 directional DFB (also known as Bamberger's 4-channel DFB) shown in Fig. 6.2(a) using two proposed filter responses. For explaining our idea, let us consider the subband 2 of Fig. 6.2(a) separately which is shown in Fig. 6.2(b) having cut-

off frequencies marked with arrows. Now to have two different directions out of subband 2 in the opposing half-planes, we need to design a filter having passband response shown with blue color given in Fig. 6.2(c). i.e., we need a group of 4 special 2-D directional filters having appropriate passband responses for subbands 1-4 with cut-off frequencies as given below

$$
\begin{aligned}
&[(-0.5\pi, \pi), (0.5\pi, -\pi)], \quad [(0.5\pi, \pi), (-0.5\pi, -\pi)], \\
&[(-\pi, 0.5\pi), (\pi, -0.5\pi)], \quad [(-\pi, -0.5\pi), (\pi, 0.5\pi)].
\end{aligned}
\tag{6.1}
$$

We refer these directional filters as *fixed partition filters* and propose the design for these. Note that they have complex impulse response coefficients and hence the overall filter bank has complex coefficients. In order to have CDFB the *analyticity* property which has several advantages over the real-valued transforms [92], we design a filter bank stage with 2-D filters having passband responses in one half of the 2-D frequency axes. These filters are referred as *mapping* filters since they map the outputs of the complex-valued partition filters into CDFB subbands having *analyticity* property. In order to obtain the analyticity, one needs infinite impulse response (IIR) mapping filters. However, IIR filters lead to non-linear phase response making them unsuitable for image processing tasks. This makes us to propose a pair of 2-D finite impulse response (FIR) mapping filters to obtain approximately analytic directional subbands of the proposed CDFB.

Figure 6.3 shows complete design diagram of the proposed 8 directional filter bank (CDFB). It consists of analysis and synthesis sides used to decompose and reconstruct the input image. The analysis side consists of two stages in which the first stage is a Bamberger's 4-channel DFB having fan ($H_i^{\text{fan}}(\mathbf{z})$) and checkerboard-shaped ($H_i^{\text{cs}}(\mathbf{z})$) filters arranged in a tree-structure as shown in Fig. 6.3. Here subscript $i = 0, 1$ indicates lowpass and highpass responses, respectively. The output of this stage has 4 real-valued directional subbands having 2-D frequency partition as shown in Fig. 6.2(a). These subbands are given as input to the second stage involving the proposed complex-valued filter responses of fixed partition and mapping filters. In this stage, each input subband is filtered using one of the 4 lowpass partition filters denoted as $H_0^{pk}(\mathbf{z}), k = 1, \ldots, 4$ having passband cut-
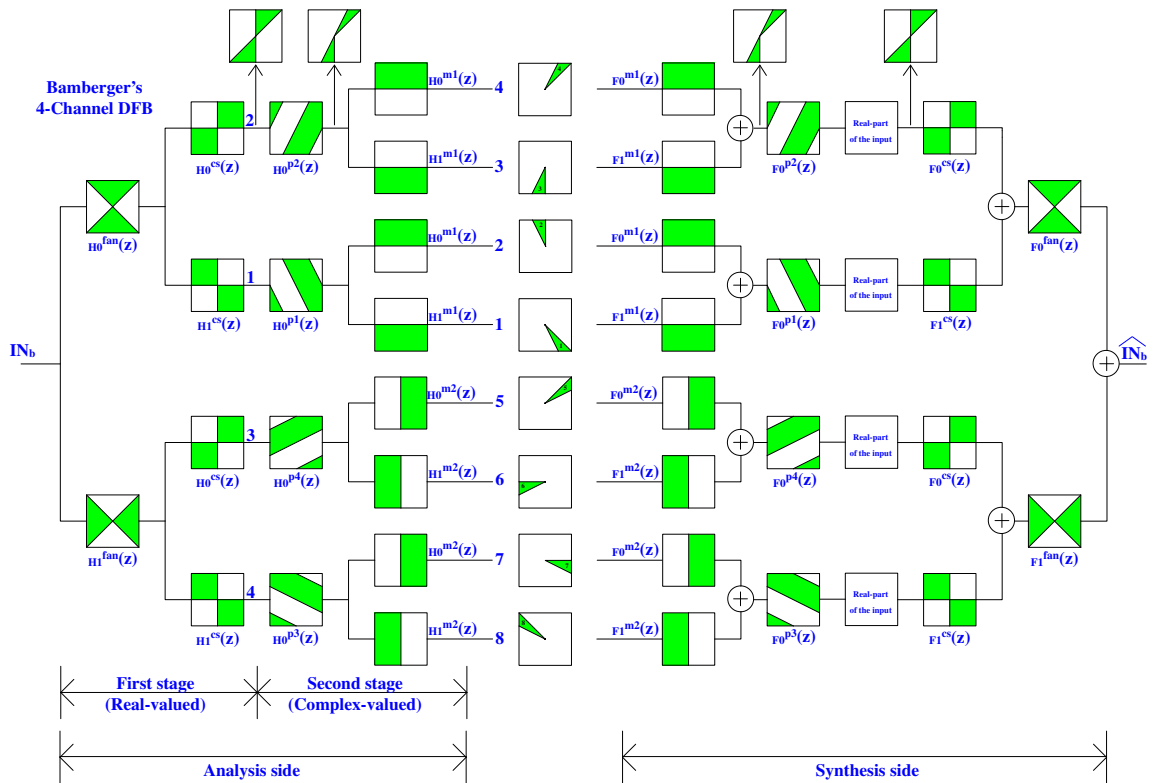
Figure 6.3: Analysis and synthesis sides of the proposed complex-valued directional filter bank (CDFB). Here the input IN_b is a bandpass filtered input image. Superscripts **fan**, **cs**, **p** and **m** represent fan-shaped, checkerboard-shaped, partition and mapping filter, respectively.

off frequencies as specified in equation (6.1). For better understanding, we have shown the resulting input and output of the partition filter $H_0^{p2}(\mathbf{z})$ in Fig. 6.3. The output of a partition filter is then passed through a two-channel mapping filter bank having appropriate half-plane frequency selectivity i.e., by using responses $H_i^{m1}(\mathbf{z})$ or $H_i^{m2}(\mathbf{z})$, $i = 0, 1$. Finally, at the output of second stage we obtain 8 *analytic* directional subbands of the proposed CDFB design. Considering the real-part coefficients of these directional subbands, we get the 2-D frequency partition as shown in Fig. 6.1(b). Synthesis side for the proposed CDFB is also shown in Fig. 6.3 and it is similar to the analysis side arranged in reversed order using synthesis filter responses. $\widehat{\text{IN}_b}$ is the final reconstructed output image.

All filters used in the CDFB design represent 2-D nonseparable FIR filters designed using *Transformations of variables* (TROV) technique proposed in [111]. TROV is a simple and flexible 1-D to 2-D mapping technique equivalent to the generalized McClellan transformation that designs filter responses of different

shapes and sampling lattices. This technique requires two inputs: linear phase filter coefficients of the 1-D wavelet and 2-D nonseparable transformation kernel which decides the passband shape of the resulting filter. Here, we have used Cohen-Daubechies-Feauveau *CDF 9-7* as 1-D wavelet filter. 2-D transformation kernel is obtained by truncating the 2-D ideal impulse response (denoted using r) of the desired filter using a 2-D window obtained from 1-D Kaiser window having length $L_w = 27$ and shape parameter $\beta = 4.5$. Higher value of L_w is used to achieve the sharp roll-off characteristics.

Fan and checkerboard-shaped filters are required to obtain Bamberger's 4-channel DFB partition as shown in Fig. 6.1(a). The ideal impulse response of the fan-shaped filter $r^{\text{fan}}(\mathbf{n})$ is obtained by modifying the ideal impulse response of diamond-shaped filter $r^{\text{diam}}(\mathbf{n})$ [111] as $r^{\text{fan}}(\mathbf{n}) = (-1)^{n_2} r^{\text{diam}}(\mathbf{n})$. Checkerboard-shaped filters can be obtained using the design procedure given in [111] or by quincunx upsampling of the fan filters [23].

In order to obtain the partition filters, we propose the following ideal impulse responses to design a group of 4 partition filters having desired passband supports and cut-off frequencies as mentioned in equation (6.1).

$$r^{\text{p1}}(\mathbf{n}) = jsinc\left(\frac{n_1\pi}{2}\right) sinc\left(n_2\pi - 0.5n_1\pi\right) sin\left(\frac{n_1\pi}{2}\right)$$
$$r^{\text{p2}}(\mathbf{n}) = jsinc\left(\frac{n_1\pi}{2}\right) sinc\left(n_2\pi + 0.5n_1\pi\right) sin\left(\frac{n_1\pi}{2}\right)$$
$$r^{\text{p3}}(\mathbf{n}) = jsinc\left(\frac{n_2\pi}{2}\right) sinc\left(n_1\pi - 0.5n_2\pi\right) sin\left(\frac{n_2\pi}{2}\right)$$
$$r^{\text{p4}}(\mathbf{n}) = jsinc\left(\frac{n_2\pi}{2}\right) sinc\left(n_1\pi + 0.5n_2\pi\right) sin\left(\frac{n_2\pi}{2}\right).$$

Our design of 2-D mapping filters which are used to obtain 8 analytic directional subbands is motivated by the 1-D mapping filter approach presented in [38]. Here, we design a pair of 2-D mapping filters which are used to select the entire positive/negative Fourier half-planes along the ω_1 and ω_2 axes. We propose their complex-valued ideal impulse responses as,

$$r^{\text{m1}}(\mathbf{n}) = jsinc\left(\frac{n_1\pi}{2}\right) sinc\left(n_2\pi\right) sin\left(\frac{n_1\pi}{2}\right)$$
$$r^{\text{m2}}(\mathbf{n}) = jsinc\left(\frac{n_2\pi}{2}\right) sinc\left(n_1\pi\right) sin\left(\frac{n_2\pi}{2}\right).$$

Figures 6.4(a) and 6.4(b) show typical analysis side lowpass frequency responses of the required filters using 3-D and 2-D plots, respectively. Impulse responses of all the designed filters are divided by $\sqrt{2}$ so that they satisfy the *Bezout identity* [23] required for nonsubsampled FB designs.
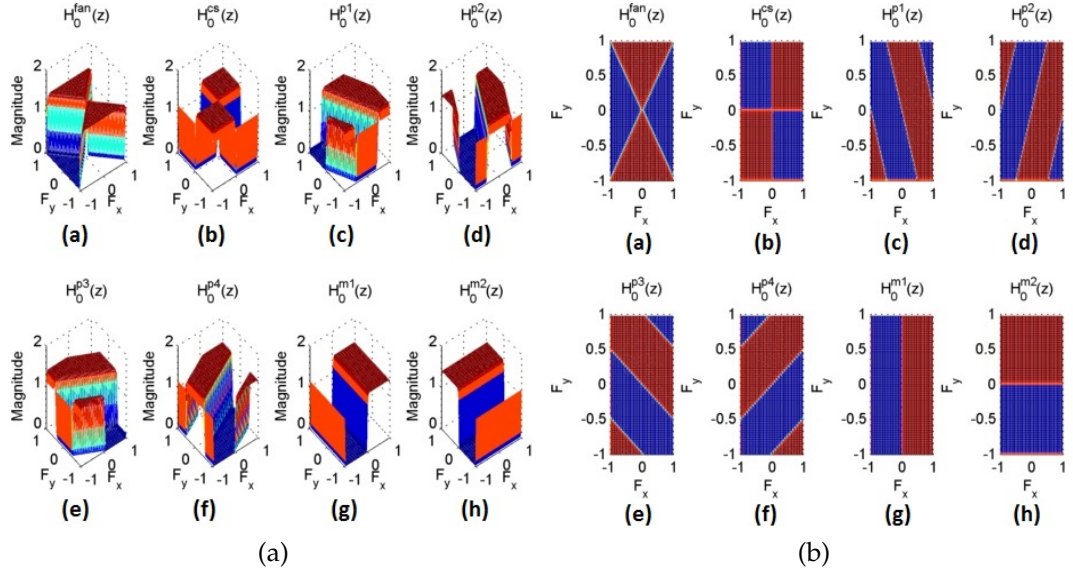
Figure 6.4: Typical analysis lowpass frequency responses of the 2-D FIR filters used in the CDFB design. These filters are obtained using TROV [111] with transformation kernel parameters $L_w = 27, \beta = 4.5$ and the CDF 9/7 wavelet filter coefficients. Here, Fig. 6.4(a) shows: 3-D plots with frequency responses for **(a)** fan-shaped filter ($H_0^{fan}(\mathbf{z})$), **(b)** checkerboard shaped filter ($H_0^{cs}(\mathbf{z})$), **(c)-(f)** a group of 4 fixed partition filters ($H_0^{pk}(\mathbf{z}), k = 1,\ldots,4$) **(g)** mapping filter ($H_0^{m1}(\mathbf{z})$) and **(h)** mapping filter ($H_0^{m2}(\mathbf{z})$). While, Fig. 6.4(b) shows: 2-D plots of the responses shown in Fig. 6.4(a).

6.2.2 Multiresolution CDFB

Figure 6.5 shows how the multiresolution (MR) stage is implemented to obtain the multiresolution CDFB and hence multiresolution in the proposed CAMDFB. For the input image IN, the MR scheme outputs one lowpass and J bandpass images for J level decomposition. Each of the jth-scale ($j = 1,\ldots,J$) bandpass image IN_b is used as input to the CDFB design shown in Fig. 6.3. Hence, multiresolution CDFB outputs one lowpass and 8 directional subbands at each scale.

We use *nonsubsampled pyramid* (NSP) scheme of [23] to obtain the multiresolution. However, we modify the NSP stage in order to have better sparsity prop-
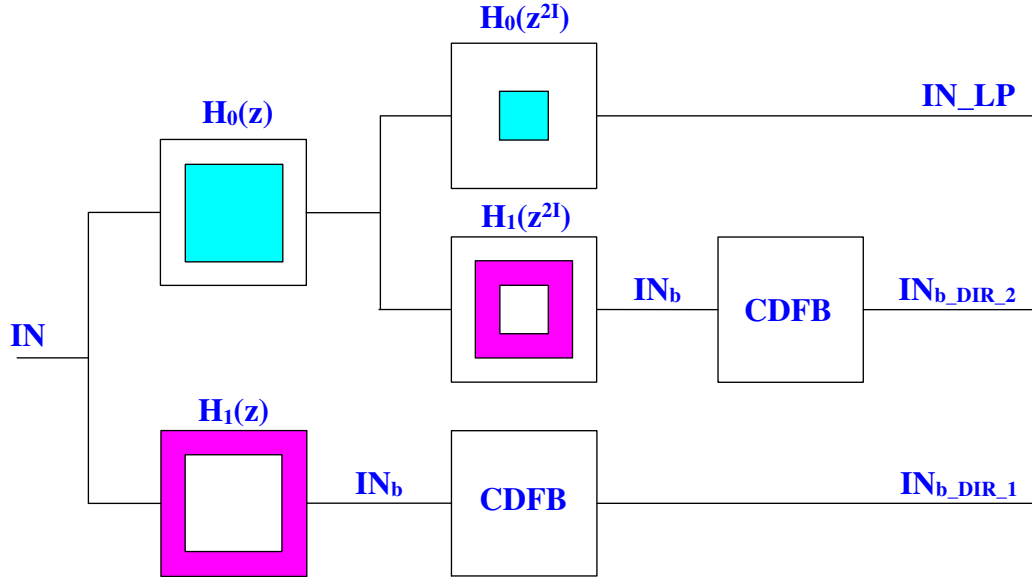
Figure 6.5: Analysis part of the multiresolution scheme used in the proposed CAMDFB design. Here 2-level decomposition scheme is shown with $H_i(\mathbf{z})$, $i = 0, 1$ representing the 2-D lowpass and highpass filter responses, respectively. $H_i(\mathbf{z^{2I}})$, $i = 0, 1$ represent the 2-D upsampled lowpass and highpass filter responses, where $\mathbf{I}$ is the 2×2 identity matrix. Here, the input image is represented by the term $\mathbf{IN}$ while the terms $\mathbf{IN_b}$ and $\mathbf{IN_{b\_DIR\_j}}$ represent the bandpass input and 8 directional subband outputs of the proposed CDFB at jth level decomposition.

erties in the transform representation. It is widely known in wavelets and filter banks research community that approximation power of wavelets depends on their *vanishing moments* [114]. Higher the number of vaninshing moments better is the lowpass approximation resulting in significantly sparse directional subbands. This concept of vanishing moments is also known as the *regularity constraints* and it is realized in practice using the digital multirate filter banks, by imposing zeros at $z = -1$ or $\omega = \pi$ [78]. In our design also we use regularity constraints on $H_0(\mathbf{z})$ in order to have high approximation power to obtain better lowpass approximation and directional subbands having better sparsity. In order to do this, we use 1-D biorthogonal wavelet filters (BWFs) having high vanishing moments along with the properties such as linear phase, near-orthogonality, better frequency selectivity and time-frequency localization due to their superior performance. We use the approach presented in [84] for designing such filters. The lengths of the analysis and synthesis lowpass filters obtained are 13 and 19, respectively. Finally, in order to impose sufficiently high *line zeros* for obtaining better frequency

response characteristics of the 2-D filters, we use the 2-D zero-phase mapping function of the form [23]:

$$F(x_1, x_2) = -1 + 2P_{K_1,L_1}(x_1)P_{K_2,L_2}(x_2). \tag{6.2}$$

Here, $x_1 = \cos(\omega_1)$, $x_2 = \cos(\omega_2)$ and $P_{K_i,L_i}(x_i)$, $i = 1,2$ is a maximally-flat halfband polynomial where values of K_i and L_i show the degree of flatness at $x_i = -1$ and $x_i = 1$, respectively. We have used $K_1 = K_2 = 3$ and $L_1 = L_2 = 6$ so as to ensure 6th order zero at $\omega_1 = \pm\pi$ and $\omega_2 = \pm\pi$. The zero-phase mapping function used is then given by

$$F(x_1, x_2) = \frac{(x_1+1)^3 (x_2+1)^3 \left(\frac{3x_1^2}{2} - \frac{9x_1}{2} + 4\right) \left(\frac{3x_2^2}{2} - \frac{9x_2}{2} + 4\right)}{32} - 1. \tag{6.3}$$

A 2-D mapping kernel of size 11×11 is obtained by substituting $x_1 = \frac{z_1 + z_1^{-1}}{2}$ and $x_2 = \frac{z_2 + z_2^{-1}}{2}$ in equation (6.3). Now, using this mapping kernel and 1-D wavelet filter coefficients, we obtain the coefficients of 2-D non-separable FIR filters $H_i(\mathbf{z})$ and $F_i(\mathbf{z})$, $i = 0, 1$ using McClellan transformation. Frequency responses of these filters are shown in Fig. 6.6.

(a)   (b)
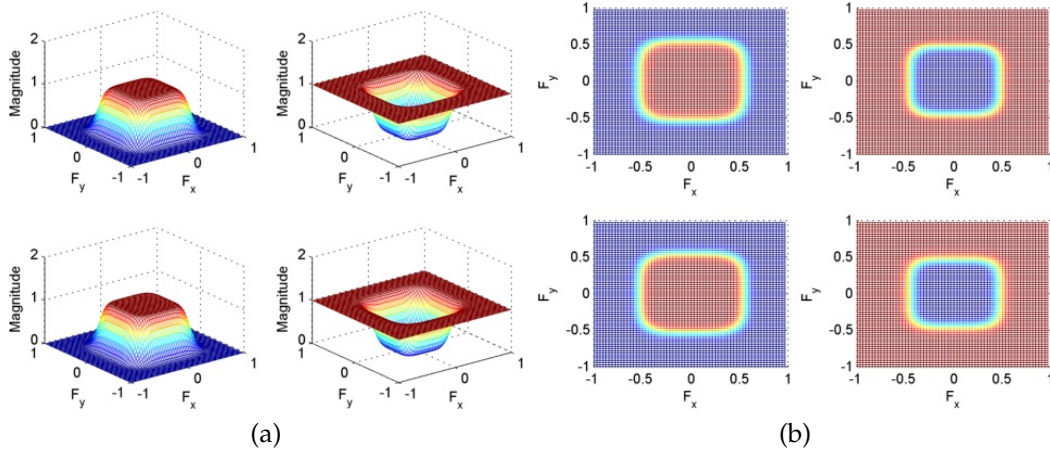
Figure 6.6: Frequency responses of the 2-D nonseparable analysis and synthesis filters designed to use in the multiresolution stages. Fig. 6.6(a) shows 3-D plots of the designed filters and Fig. 6.6(b) shows 2-D plots for the same.

We now compare the sparsity properties of the NSCT MR stage [23] and pro-

<div style="text-align:center">(a)   (b)</div>
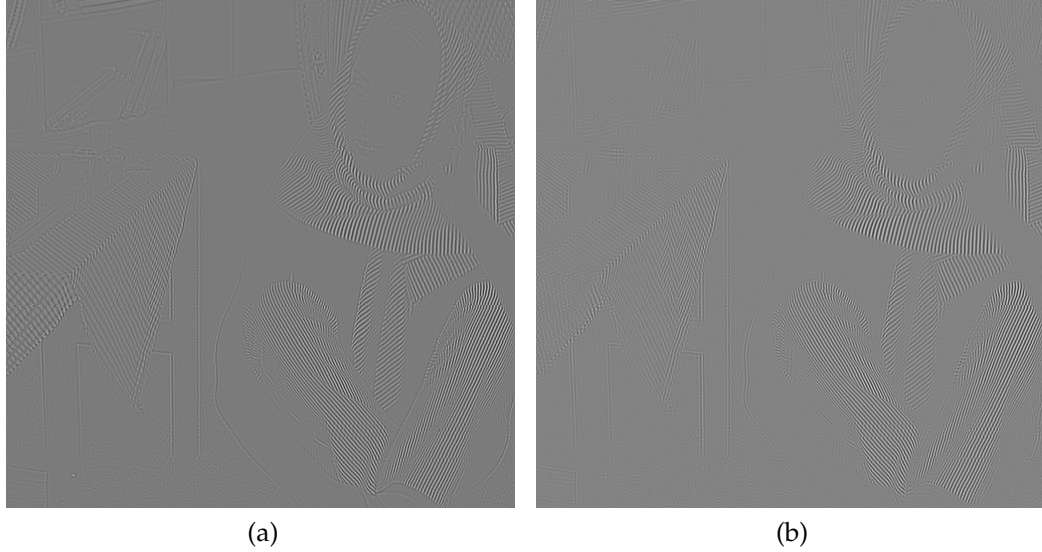
Figure 6.7: Sparsity comparison of the multiresolution stages. (a) NSCT (b) proposed

posed MR stage. In case of NSCT, CDF 9/7 wavelet filters are used with mapping kernel as given in [23]. Fig. 6.7 shows the 1-level decomposed highpass subband images for *Barbara* image using NSCT and proposed MR stage. For better comparison, we have avoided to show the original image here which can be found in Fig. 6.9(a). It is clear from Fig. 6.7 that proposed MR stage gives better sparseness when compared to NSCT. The highpass subband for the proposed MR stage has comparatively lesser image features than NSCT which can be observed especially in the facial area (lips, eyes, nose), table cloth and books in the shelf. This indicates that higher number coefficients have near zero values in case of proposed MR stage than in case of NSCT. Since highpass subband have better sparseness, lowpass information of the input image is better preserved in the lowpass subband of the proposed MR stage.

Using the modified multiresolution stage and CDFB as given in Fig. 6.5, we obtain one lowpass IN_LP and 8 high frequency directional subbands represented collectively using $IN_{b\_DIR\_j}$ for jth level decomposition. Frequency responses of the resultant filters used to obtain the $IN_{b\_DIR\_1}$ are given below and their real-

<div style="text-align:center">109</div>

part frequency responses i.e., real($H^i(\mathbf{z})$, $i = 1, \ldots, 8$) are shown in Fig. 6.8.

$$H^3(\mathbf{z}) = H_0^{\text{fan}}(\mathbf{z})H_0^{\text{cs}}(\mathbf{z})H^{p2}(\mathbf{z})H_0^{\text{m1}}(\mathbf{z})H_1(\mathbf{z}),$$

$$H^4(\mathbf{z}) = H_0^{\text{fan}}(\mathbf{z})H_0^{\text{cs}}(\mathbf{z})H^{p2}(\mathbf{z})H_1^{\text{m1}}(\mathbf{z})H_1(\mathbf{z}),$$

$$H^1(\mathbf{z}) = H_0^{\text{fan}}(\mathbf{z})H_1^{\text{cs}}(\mathbf{z})H^{p1}(\mathbf{z})H_0^{\text{m1}}(\mathbf{z})H_1(\mathbf{z}),$$

$$H^2(\mathbf{z}) = H_0^{\text{fan}}(\mathbf{z})H_1^{\text{cs}}(\mathbf{z})H^{p1}(\mathbf{z})H_1^{\text{m1}}(\mathbf{z})H_1(\mathbf{z}),$$

$$H^6(\mathbf{z}) = H_1^{\text{fan}}(\mathbf{z})H_0^{\text{cs}}(\mathbf{z})H^{p4}(\mathbf{z})H_0^{\text{m2}}(\mathbf{z})H_1(\mathbf{z}), \qquad (6.4)$$

$$H^5(\mathbf{z}) = H_1^{\text{fan}}(\mathbf{z})H_0^{\text{cs}}(\mathbf{z})H^{p4}(\mathbf{z})H_1^{\text{m2}}(\mathbf{z})H_1(\mathbf{z}),$$

$$H^8(\mathbf{z}) = H_1^{\text{fan}}(\mathbf{z})H_1^{\text{cs}}(\mathbf{z})H^{p3}(\mathbf{z})H_0^{\text{m2}}(\mathbf{z})H_1(\mathbf{z}),$$

$$H^7(\mathbf{z}) = H_1^{\text{fan}}(\mathbf{z})H_1^{\text{cs}}(\mathbf{z})H^{p3}(\mathbf{z})H_1^{\text{m2}}(\mathbf{z})H_1(\mathbf{z}).$$
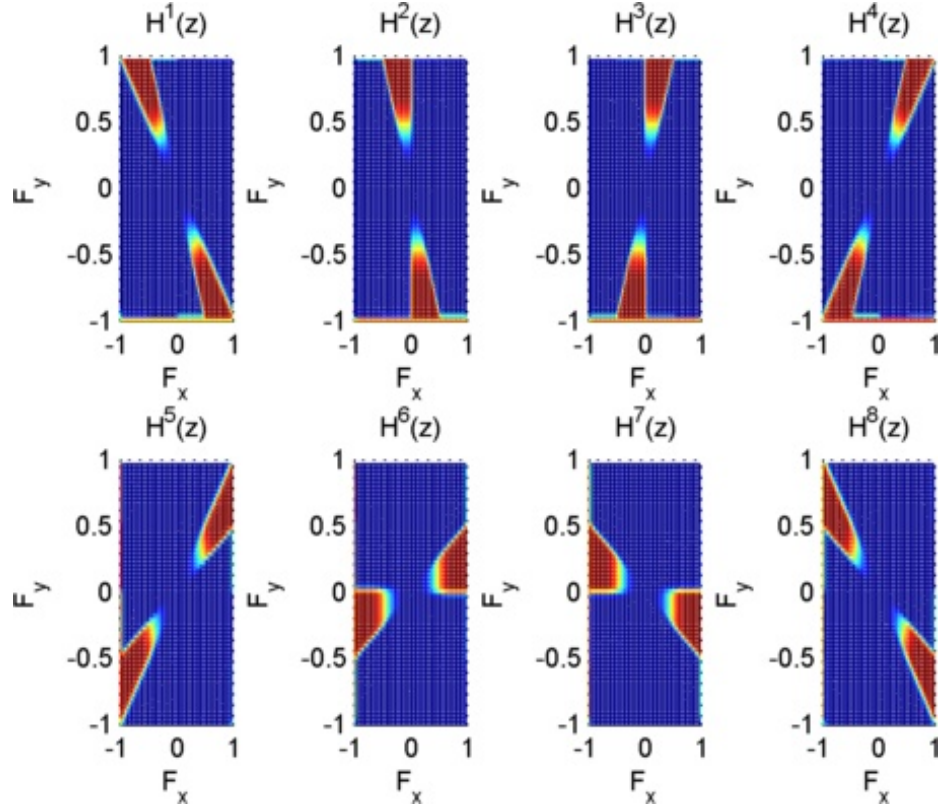
Figure 6.8: Frequency responses of the resultant analysis directional subbands of the proposed multiresolution CDFB for one level decomposition.

6.2.3 Finding N dominant directions of the input image

In order to decide the number of dominant directions N as required in our CAMDFB design, we make use of *orientation map* of an image obtained using *local orientation*

Figure 6.9: Orientation map of *Barbara* image using a block size of 8×8. (a) Original *Barbara* image (size: 512×512) (b) orientation map [35] (c) corrected orientation map.

estimation approach presented in [35]. Here, the orientation map of a given image is obtained by using the approach of multiscale principle component analysis (PCA). To do this, input image is divided into non-overlapping blocks of fixed size and local orientation of each block is computed to obtain orientation map for the entire image. We use this orientation map as an initial estimate of the dominant directions in the input image. Consider *Barbara* image shown in Fig. 6.9(a) which has the orientation map as shown in Fig. 6.9(b). One can observe in Fig. 6.9(b) that there are erroneous orientations for objects at constant depths and in the background. We correct this error simply by neglecting those orientations where block variance is below 100 thereby rejecting the insignificant geometrical features. Block variance threshold value of 100 used here is found to be suitable choice after experimenting with variety of images (natural, remote sensing etc.). The corrected orientation map is shown in Fig. 6.9(c).

The range of angles in the orientation map is between $[-90°, 90°]$. We convert this range to lie between $0°$ to $180°$ and obtain the histogram of this orientation map to decide the dominant directions present in the input image. Fig. 6.10(a) shows the histogram of the orientation map shown in Fig. 6.9(c) using an interval of $1°$ i.e., 180 bins. Fig. 6.10(b) shows the same with the 8 bins i.e., splitting the entire range into 8 intervals. The 8 bin histogram have range of orientation angles similar to range of CDFB subband angle selectivity and it roughly shows the directional significance of CDFB subbands for the input image under consideration.

111

Histogram with 180 bins is used to estimate the number of dominant directions for each CDFB suuband. Now, based on the histograms shown in Fig. 6.10, we find the partition vector of length 8 which represents the number of fine partitions required for 8 subbands of the CDFB to obtain the N dominant directions.
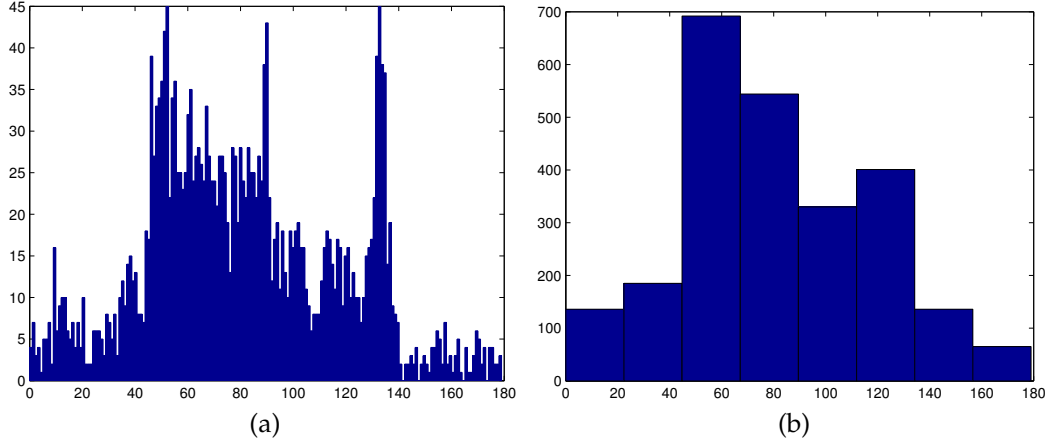
Figure 6.10: Histogram of orientation map (between $[0°, 180°]$) of *Barbara* image using (a) 180 bins (b) 8 bins.

Let, **k** and **ka** be the vectors of number of local orientations using 8 and 180 bins, respectively. Let n_a and n_b be the total number of local orientations and number of orientations set to zero because of block variance less than 100. Then the vector $\mathbf{p} = p_i, i = 1, \ldots, 8$ indicating the probabilities for orientations with 8 bins can be written as

$$\mathbf{p} = p_i = \frac{k_i}{(n_a - n_b)}, \quad i = 1, \ldots, 8. \tag{6.5}$$

Using **p**, we define a weight vector $\mathbf{w} = \mathbf{1} - \mathbf{p}$ which is used in finding the number of significant angles (directions) in each of the 8 bins which is done as follows. We consider the significance of each angle between $0°$ to $180°$ with respect to 8 bins and define an average vector as $\mathbf{av} = \frac{max(\mathbf{ka}_i)+min(\mathbf{ka}_i)}{2}$. Here, the vectors $\mathbf{ka}_i$, $i = 1, \ldots, 8$ are obtained by splitting $0°$ to $180°$ into 8 intervals i.e., we have 22 angles in each $\mathbf{ka}_i$. For example, $\mathbf{ka}_1$ is vector consisting of number of orientations in first 22 angles between $0°$ to $22°$. While, $max(\mathbf{ka}_i)$ and $min(\mathbf{ka}_i)$ indicate maximum and minimum values of number of orientations for i^{th} interval. We then have 8 such *max* and *min* values for the entire $0°$ to $180°$ range. In order to arrive at

dominant directions for each of the eight bins, we select threshold $\gamma = \gamma_i$ obtained as $\gamma = \mathbf{w} \odot \mathbf{av}$ which represents average number of occurrences of local orientations in each bin. Here, $\odot$ denotes the element-wise multiplication. Now for each $\mathbf{ka}_i$, $i = 1, \ldots, 8$ which has 22 angles, we find the number of local orientation angles exceeding γ_i and the same is represented as α_i. Here, α_i denotes the number of angles in each of the ith bin above threshold and they are considered as dominant directions. Finally, partition vector is obtained as $\mathbf{np} = np_i = \text{round}(\frac{\alpha_i}{4})$, $i = 1, \ldots, 8$ and N as $\sum_{i=1}^{8} np_i + 1$. Now, using $\mathbf{np}$ and $\mathbf{ka}_i$, we select cut-off frequencies to partition the corresponding CDFB subband. We explain this using an example. For the *Barbara* image shown in the Fig. 6.9(a), number of partitions obtained for the eight subbands are $\mathbf{np} = [0, 0, 6, 5, 1, 1, 0, 0]$. Now, CDFB subband having orientation selectivity of 45 degrees to 67.5 degrees need 6 partitions. From vector $\mathbf{ka}_3$, 6 directions having higher frequency of occurrences i.e., dominant directions are chosen. These directions are considered to be center frequencies of the finer subbands to be partitioned. Then cut-off frequencies are calculated to design the *partition filters* for finer partitioning of the appropriate CDFB subbands to incorporate adaptive direction selectivity. The filter bank design involving such partition filters is explained in the next subsection.

6.2.4   Adaptive partition filter bank stage

In order to have adaptive directional selectivity in the proposed CAMDFB, a partition filter bank stage is used as the final stage. Here, 8 directional subbands of the multiresolution CDFB are partitioned into the N finer subbands using the partition vector $\mathbf{np}$. To do this, we require nonuniform partitioning of the CDFB subbands using generalized set of 2-D directional filters having cut-off frequencies of the form

$$
\begin{aligned}
&[(-C\pi, \pi), (C\pi, -\pi)], \quad [(C\pi, \pi), (-C\pi, -\pi)], \\
&[(-\pi, C\pi), (\pi, -C\pi)], \quad [(-\pi, -C\pi), (\pi, C\pi)].
\end{aligned}
\tag{6.6}
$$

Here, C is the cut-off frequency which is different for each directional filter. Note that equation (6.1) can be obtained with $C = 0.5$. To obtain filters having arbitrary

cut-off frequencies as specified in equation (6.6), we propose a *generalized* group of 4 complex 2-D ideal impulse responses which when used in conjunction with transformation of variables (TROV) [111] technique, generate filters that have desired 2-D passband responses. These ideal impulse responses are given as

$$r^{p1}(\mathbf{n}) = jsinc\left(\frac{n_1\pi}{2}\right)sinc\left(n_2\pi - Cn_1\pi\right)sin\left(\frac{n_1\pi}{2}\right)$$
$$r^{p2}(\mathbf{n}) = jsinc\left(\frac{n_1\pi}{2}\right)sinc\left(n_2\pi + Cn_1\pi\right)sin\left(\frac{n_1\pi}{2}\right)$$
$$r^{p3}(\mathbf{n}) = jsinc\left(\frac{n_2\pi}{2}\right)sinc\left(n_1\pi - Cn_2\pi\right)sin\left(\frac{n_2\pi}{2}\right)$$
$$r^{p4}(\mathbf{n}) = jsinc\left(\frac{n_2\pi}{2}\right)sinc\left(n_1\pi + Cn_2\pi\right)sin\left(\frac{n_2\pi}{2}\right).$$

We call these 2-D directional filters simply as *partition* filters since the fixed partition filters used in the CDFB design can be obtained by using $C = 0.5$.

These designed filters are then used in the partition filter bank stage following the 8 directional CDFB stage to obtain one lowpass and N highpass directional representation of the proposed CAMDFB. This completes the analysis or decomposition side of the proposed CAMDFB. Similarly, the synthesis side of the CAMDFB is designed using all the filter bank stages present on the analysis side. These are arranged in the reverse order where analysis filters are replaced by appropriate synthesis filters thus obtaining the reconstructed image as the final output.

6.3   Pansharpening Using the Proposed CAMDFB

Pansharpening is one of the important preprocessing remote sensing tasks that makes use of spatial features of panchromatic image to obtain high spatial resolution multispectral images. To elaborate, many satellites like SPOT, QuickBird, IKONOS, etc., provide the earth information by capturing two different types of images, namely panchromatic (Pan) and multispectral (MS). Pan is a grayscale image that provides detailed spatial information of objects/features on the earth's surface i.e., it has high spatial resolution whereas MS images provide spectral information in multiple bands i.e., they have better spectral resolution. MS images

have low spatial resolution since building a sensor with high resolutions for both spatial and spectral, at the same time is hardly feasible [57]. Having better spatial information of MS images is beneficial in many remote sensing applications [88]. The goal of pansharpening is to achieve this high spatial resolution of MS images with minimum spectral distortion by using the Pan details.

Since Pan image may have arbitrary orientations of spatial features, we aim to use our adaptive transform to capture these orientations more *effectively* to pansharpen the MS images. For detailed classification and literature overview on transform-based pansharpening approaches we refer to [8] as an excellent survey paper.

6.3.1 Proposed pansharpening approach

The proposed approach for pansharpening is described by considering one of the MS bands. As a preprocessing step, Pan image is histogram matched to the each of the MS bands.

Figure 6.11 shows the block diagram of the proposed pansharpening approach using CAMDFB. First, the input MS band is upsampled to the size of the Pan image by using by using 23-tap interpolation filter [4].

We perform 2 level CAMDFB decomposition and obtain N dominant directions in each scale. This gives us one lowpass and N directional subbands represented by PAN_LP and PAN_HP$_{i,j}$ ($i = 1, 2; j = 1, \ldots, N$), respectively where i represents scale number and j corresponds to one of the N dominant directions. The upsampled MS band is also subjected to 2-level decomposition obtaining MS_LP and MS_HP$_{i,j}$. These are used as inputs to *adaptive detail injection module* (ADIM) which is based on "Amèlioration de la Rèsolution Spatialle par Injection de Structures" meaning *spatial resolution enhancement by injection of structures* (ARSIS) concept [86]. The ARSIS concept provides a reliable multiscale framework for pansharpening that carefully considers the remote sensing physics and also paves the way for introducing new concepts within the same framework [113]. The ARSIS concept is used here as an *interband structure model* (IBSM) [40] to model the relationship between approximation/detail coefficients of the MS band and Pan
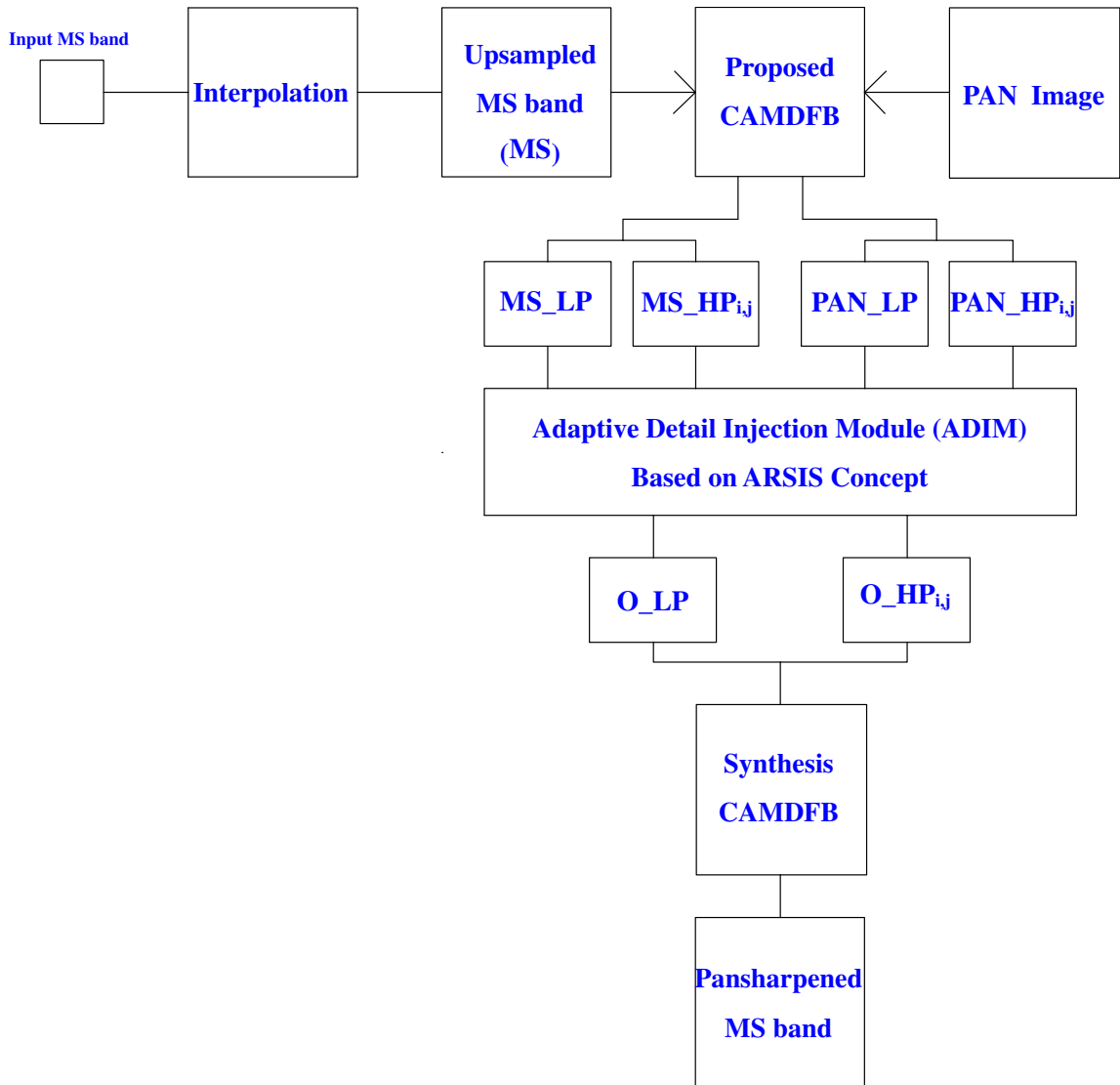
Figure 6.11: Proposed pansharpening approach using the designed CAMDFB. Here, MS_LP and PAN_LP represent the lowpass approximations of upsampled MS band i.e., MS and PAN image, respectively, while $MS\_HP_{i,j}$ and $PAN\_HP_{i,j}$ represent high frequency detail subbands of MS and PAN image when decomposed using proposed CAMDFB. O_LP and $O\_HP_{i,j}$ are lowpass and high frequency subband outputs of the ARSIS concept-based adaptive detail injection module (ADIM).

image at the same resolution. Here, the model parameters are calculated using the coarser resolution of both these images to infer the suitable injection gains (weights). In order to compute these, we use Model 2 of [86] in which IBSM is based on the relationship between detail coefficients of MS and Pan images. Since, locally adaptive injection models such as context based decision (CBD) [5] give superior results we used a local approach where weights are calculated for overlapping blocks of PAN and MS highpass details. Model parameters are estimated from 3rd scale detail coefficients of the PAN and MS images i.e., from PAN_HP$_{3,j}$ and MS_HP$_{3,j}$ which are obtained by taking one more level CAMDFB decomposition on already obtained PAN_LP and MS_LP subbands. Note that, only detail coefficients of 3rd scale are used to estimate the adaptive weights and bias values which are then used for obtaining the detail coefficients of the fused image. The outputs of the ADIM are O_LP and O_HP$_{i,j}$, respectively which are obtained using following two equations:

$$O\_LP = MS\_LP \tag{6.7}$$

$$O\_HP_{i,j} = a_j \times PAN\_HP_{i,j} + b_j \tag{6.8}$$

where, $i = 1, 2$ and $j = 1, \ldots, N$. While, a_j and b_j are N adaptive weights and bias values for every overlapping block of size 8×8 having block overlap size of 4. Overlapping blocks are used to avoid any spurious artifacts in the pansharpened band. The adaptive weights and bias values are obtained as:

$$a_j = \frac{std2(MS\_HP_{3,j})}{std2(PAN\_HP_{3,j})} \quad \text{and,}$$
$$b_j = mean2(MS\_HP_{3,j}) - a_j \times mean2(PAN\_HP_{3,j}). \tag{6.9}$$

Taking real-part of the synthesis CAMDFB output gives us the pansharpened image for the considered MS band. The same method is applied for each of the MS bands to obtain the pansharpening of all the MS bands.

Finally, we discuss the reason for using 2 levels of CAMDFB decomposition in our approach. Due to high vanishing moments used in designing the $H_0(\mathbf{z})$, lesser number of decomposition levels are required for approximating a smooth

2-D function within certain error tolerance (similar to the 1-D wavelet approximation case proven by Unser in [114]). Also, most of the spectral information present in the original low-resolution MS band is retained in its decomposed low-pass subband [93]. One may argue that for multiresolution analysis (MRA) based pansharpening approaches, lower decomposition levels result in better spectral quality but in poor spatial quality [82]. However, due to better lowpass approximation and directional selectivity used in our approach, we obtain better spectral as well as spatial details in the pansharpened outputs.

6.4 Experimental Results

In this section, we present the pansharpening results of our proposed CAMDFB-based approach and its comparison with current state-of-the-art approaches and NSCT-based approach. Experiments are conducted on imagery captured using QuickBird and IKONOS-2 satellites. QuickBird dataset images [2] used here were acquired on 4th July, 2005 capturing the sub-urban area of Boulder city, USA, while the IKONOS-2 images [1] were acquired on 22nd February, 2003 over Mount Wellington area around Hobart Tasmania. Both these datasets include co-registered raw images of 1 PAN and 4 MS bands (Blue (band 1) - Green (band 2) - Red (band 3) - Near Infrared (band 4)) captured over the mentioned areas having radiometric resolution of 11 bits. For QuickBird, PAN spatial resolution is $0.6m \times 0.6m$ while it is $2.4m \times 2.4m$ for MS images. For IKONOS-2, they are $1m \times 1m$ and $4m \times 4m$. Due to large sizes of the raw images in both these datasets, the experiments were performed by cropping suitable region of interest (ROI) having original PAN and MS images of size 1024×1024 and 256×256, respectively. Before pansharpening, these 11-bit/pixel dataset images are normalized by dividing each pixel intensity by the maximum value i.e., 2047. We display the output images using general 8-bit/pixel convention. In order to test the results quantitatively, pansharpening is done on the spatially degraded PAN and MS images obtained from their original counterparts keeping the resolution ratio and radiometric resolution same as in the originals. The pansharpened MS bands are then compared with the orig-

inal MS images which are considered as the ground truth (GT) images. In our experiments, the spatially degraded datasets are obtained by using the filtering operation on original dataset images considering the sensor modulation transfer function (MTF) responses followed by a downsampling operation with a factor of 4 (resolution ratio between PAN and MS images) along the rows and columns [5]. Hence the sizes for PAN and MS images in both the spatially degraded datasets are 256×256 and 64×64, respectively. All the pansharpening visual results provided in this section are displayed using true-color composites (bands 3-2-1) of size 256×256.

We have compared the performance of our approach with different state-of-the-art pansharpening approaches. For comparison, we have chosen three component substitution (CS) based approaches namely Gram Schmid adaptive (GSA) [6], band-dependent spatial detail algorithm (BDSD) [41] and partial replacement adaptive component substitution (PRACS) [22]. We also compare with three MRA-based (or transform-based) approaches, adaptive wavelet luminance proportional (AWLP) [77], generalized Laplacian pyramid-context based decision (GLP-CBD) [5] and nonsubsampled contourlet transform (NSCT) [23]. For NSCT, we have used the same detail injection scheme applied in our approach to validate the efficacy of proposed CAMDFB. For analyzing the improvements gained by these methods, we have also used in comparison a simple interpolated MS output obtained by using 23-tap interpolation filter [4] without spatial detail injection referred as EXP. For accurate and fair comparison, we have used the *pansharpening toolbox* made available by the authors of [121] for implementation of the above methods. For proposed and other MRA-based approaches, 2 levels of decomposition were used in all experiments. In case of proposed approach, block size of 4×4 is used to estimate the dominant directions in the degraded PAN. With this block size, the estimated dominant directions are similar to those obtained using original PAN. In case of NSCT, we have used 4 and 16 directions for the two levels, respectively.

The quantitative measures used for performance evaluation are correlation co-efficient (CC), spectral angle mapper (SAM) [55], *Erreur Relative Globale Adimen-*

sionnelle de synthèse (ERGAS) [124], Q4 index [7], universal image quality index (Q_{avg}) [130], spatial correlation coefficient (SCC) [77] and feature similarity index measure (FSIM) [135]. CC provides band-wise evaluation of spectral information difference between pansharpened and GT MS images. Ideally CC value should be 1. SAM determines the spectral similarity between two spectra by calculating the "angle" between the two spectra, treating them as vectors in a space with dimensionality equal to the number of bands [55]. SAM is a global measure for spectral distortion with ideal value 0 indicating absence of spectral distortion however radiometric distortion may be present [70]. ERGAS is a global quality index used for measuring the radiometric distortion with ideal value of 0. Q4 index proposed in [7] is a global measure for 4 band MS data as in the case of QuickBird and IKONOS datasets and accounts for *local mean bias*, *changes in the contrast*, *loss of correlation in individual bands* along with the *spectral distortion*. Q4 index is as an extension of *Universal Image Quality Index* (UIQI) proposed by Wang and Bovik [130]. Prior to Q4, an average quality measure based on UIQI known as Q_{avg} was commonly used as a global quality index measure. It models the difference between pansharpened and GT multispectral image as a combination of three factors: loss of correlation, luminance distortion and contrast distortion [77] and it is still actively used by the pansharpening research community. Both Q4 and Q_{avg} indexes are generally calculated using non-overlapping windows of fixed size such as 8×8, 16×16 etc. In our experiments, fixed window size of 32×32 is used in all calculations. Ideal value for both Q4 and Q_{avg} is 1. SCC measure accounts for the spatial quality of the pansharpened outputs. Higher value of SCC (ideal : 1) denotes spatial quality of the outputs closer to that of PAN. *Feature Similarity Index Measure* (FSIM) [135] is used here as an another measure for spatial quality assessment. We calculate the FSIM value for each pansharpened MS band as measure of spatial fidelity. Higher value (ideal:1) shows better match between the spatial features of pansharpened and GT MS band following the similar reasoning used in [77] for calculating the SCC index.

6.4.1 Pansharpening results on QuickBird dataset images

In this subsection, we consider pansharpening of MS images of simulated (spatially degraded) dataset of QuickBird satellite imagery. Fig. 6.12 and Fig. 6.13 show visual comparison of results between different pansharpening approaches tested on two regions of interest. Figs. 6.12(a) and 6.13(a) show, the interpolated MS images shown as a RGB true-color composition with bands 3, 2 and 1 and are referred as EXP. Pansharpening outputs of CS-based methods BDSD, GSA and PRACS are shown in Figs. 6.12(b)-6.12(d) and 6.13(b)-6.13(d), respectively. Similarly, outputs of MRA-based methods AWLP, GLP-CBD and NSCT are shown in Figs. 6.12(e)-6.12(g) and 6.13(e)-6.13(g), respectively. Outputs of proposed approach are shown in Figs. 6.12(h) and 6.13(h), while the available ground truth MS images are shown in Figs. 6.12(i) and 6.13(i), respectively. The magnified regions corresponding to a small square area shown with a red border in Figs. 6.12(i) and 6.13(i) are displayed at the bottom left corner of all the images.

One can observe from Fig. 6.12, Fig. 6.13 and their magnified regions, that the pansharpened outputs of proposed approach shown in Fig. 6.12(h) and Fig. 6.13(h) look visually similar to the ground truth images shown in Fig. 6.12(i) and Fig. 6.13(i), respectively when compared to other approaches. The colors of the objects in the ground truth images are better preserved in the results of proposed approach due to improved spectral content preservation. For example, different colors of the rectangular-shaped objects seen in magnified region of the ground truth MS image shown in Fig. 6.12(i) are better preserved using our approach shown in Fig. 6.12(h) which is clearly evident from the magnified region shown in the bottom left corner. Similar improvements can also be observed in the result shown in Fig. 6.13(h) where colors of the circular objects resemble more closely to that in true MS image shown in Fig. 6.13(i). One can observe from the magnified regions that the proposed approach provides better spectral content preservation than the NSCT as well as other approaches which is due to better approximation power of the lowpass filter used in our multiresolution stage. Spatial quality of the images is also better and can be confirmed by observing the amount of finer details and sharpness added in the pansharpened images. In our approach, High

Figure 6.12: RGB true-color composition 3, 2 and 1 of pansharpening results obtained from degraded QuickBird dataset images. (a) EXP (b) BDSD (c) GSA (d) PRACS (e) AWLP (f) GLP-CBD (g) NSCT (h) Proposed (i) GT.

Figure 6.13: RGB true-color composition 3, 2 and 1 of pansharpening results obtained from degraded QuickBird dataset images. (a) EXP (b) BDSD (c) GSA (d) PRACS (e) AWLP (f) GLP-CBD (g) NSCT (h) Proposed (i) GT.

vanishing moments preserve the spectral properties of the input MS band, while adptive directional selectivity gives improved spatial quality. One may see color distortion in the CS-based approaches i.e., BDSD, GSA and PRACS due to local inhomogeneity of pixel values between PAN and MS images. Although, PAN and MS bands are histogram matched and adaptive weights are considered to model their relations, local dissimilarities are due to their global nature of operations. Quality of pansharpening in these methods is heavily dependent on the accuracy of the weights used to model the PAN as a linear combination MS bands. For MRA-based methods i.e., in case of AWLP, GLP-CBD and NSCT-based approach, color distortion is less when compared to CS based approaches since the lowpass filters used in these methods are designed to maximally preserve the spectral information of the MS images. AWLP perform reasonably well in terms of spectral quality considering its simple detail injection model. Apart from proposed approach, GLP-CBD also perform better in terms of spectral content preservation in which lowpass filter response matches the MS sensor MTF. Visually, spatial quality of NSCT outputs is similar to that of proposed approach whereas their spectral quality is less than our approach. Spatial quality of AWLP method is inferior when compared to GLP-CBD, NSCT and proposed approach that use AR-SIS concept as an interband structure model which effectively tackles the local dissimilarites between PAN and MS images such as object occultation, contrast inversion etc. [113].

Table 6.1 compares the quantitative measures for the results shown in Fig. 6.12 and Fig. 6.13. Quantitative measures for EXP output are given to analyze the improvements of different methods over the resampled MS band outputs. Clearly, proposed approach outperforms the compared methods consistently. For all the 4 MS bands, CC values are closer to the ideal showing maximum spectral similarity between pansharpened and GT MS bands. SAM and ERGAS values are also closer to zero meaning that average spectral and radiometric distortion is minimum for our approach. Values for spectral quality indexes i.e., SCC and FSIM are closer to ideal showing better details and preservation of local spatial structures. Higher values of Q4 and Q_{avg} shows better spectral and spatial fidelity of

Table 6.1: Quantitative measures for the pansharpening results shown on Quick-Bird dataset.

FIGURE	METHOD	CC				SAM	ERGAS	Q4	Q_{avg}	SCC	FSIM			
		B	G	R	NIR						B	G	R	NIR
	IDEAL	1	1	1	1	0	0	1	1	1	1	1	1	1
	EXP	0.8412	0.8270	0.8423	0.8191	5.1072	5.6562	0.6857	0.6693	0.5657	0.7043	0.6779	0.6723	0.6086
	BDSD [41]	0.9033	0.9245	0.9251	0.9714	4.7268	3.4723	0.8815	0.8804	0.8649	0.8354	0.8677	0.8406	0.9425
	GSA [6]	0.9020	0.9240	0.9264	0.9680	4.5201	3.4721	0.8759	0.8678	0.8603	0.8321	0.8645	0.8404	0.9405
Fig. 6.12	PRACS [22]	0.8985	0.9161	0.9147	0.9767	4.2001	3.7041	0.8580	0.8480	0.8580	0.8050	0.8281	0.7885	0.9363
	AWLP [77]	0.8893	0.9223	0.9256	0.9694	4.6428	3.5131	0.8631	0.8572	0.8725	0.8341	0.8694	0.8590	0.9312
	GLP-CBD [5]	0.9053	0.9270	0.9287	0.9686	4.4884	3.4365	0.8795	0.8700	0.8603	0.8332	0.8656	0.8414	0.9405
	NSCT [23]	0.8945	0.9309	0.9386	0.9733	4.6284	3.3453	0.8763	0.8722	0.8698	0.8311	0.8726	0.8635	0.9270
	Proposed	0.9187	0.9430	0.9443	0.9785	4.1260	3.0353	0.8964	0.8968	0.8897	0.8532	0.8881	0.8682	0.9476
	IDEAL	1	1	1	1	0	0	1	1	1	1	1	1	1
	EXP	0.8657	0.8514	0.8544	0.8531	4.9284	5.4374	0.6843	0.6669	0.5541	0.6999	0.6789	0.6626	0.6306
	BDSD [41]	0.9157	0.9350	0.9265	0.9722	4.3065	3.3322	0.8621	0.8604	0.8560	0.8407	0.8688	0.8363	0.9350
	GSA [6]	0.9106	0.9324	0.9247	0.9692	4.2719	3.3968	0.8512	0.8474	0.8515	0.8383	0.8659	0.8354	0.9330
Fig. 6.13	PRACS [22]	0.9168	0.9376	0.9296	0.9779	3.9191	3.2787	0.8566	0.8518	0.8655	0.8323	0.8618	0.8176	0.9402
	AWLP [77]	0.8981	0.9301	0.9224	0.9711	4.2537	3.4370	0.8421	0.8331	0.8631	0.8362	0.8686	0.8466	0.9296
	GLP-CBD [5]	0.9140	0.9354	0.9273	0.9699	4.2372	3.3484	0.8582	0.8504	0.8523	0.8397	0.8679	0.8371	0.9331
	NSCT [23]	0.9017	0.9389	0.9359	0.9736	4.3638	3.2847	0.8584	0.8519	0.8604	0.8328	0.8735	0.8527	0.9200
	Proposed	0.9270	0.9502	0.9450	0.9786	3.7890	2.9363	0.8830	0.8818	0.8833	0.8585	0.8897	0.8645	0.9438

the pansharpened outputs using proposed approach. CS based methods perform competitively to the MRA-based approaches in terms of quantitative measures, whereas GLP-CBD and proposed approach provide consistent performance for both the results due to their lowpass filters and effective IBSM schemes.

6.4.2 Pansharpening results on IKONOS-2 dataset images

In order to show the performance of our approach for different images, we consider one more experiment on simulated dataset of IKONOS-2 satellite imagery. Similar to QuickBird dataset case, Fig. 6.14 and Fig. 6.15 show visual results for two different regions of interest. Figs. 6.14(a) and 6.15(a) show, the resampled MS image EXP. Outputs of CS-based methods i.e., BDSD, GSA and PRACS are shown in Figs. 6.14(b)-6.14(d) and 6.15(b)-6.15(d), respectively. Similarly, outputs of MRA-based methods AWLP, GLP-CBD and NSCT are shown in Figs. 6.14(e)-6.14(g) and 6.15(e)-6.15(g), respectively. Outputs of proposed approach are shown in Figs. 6.14(h) and 6.15(h), while the available GT MS images are shown in Figs. 6.14(i) and 6.15(i), respectively.

Close look at the outputs shown in Fig. 6.14 and Fig. 6.15, one can say that spectral distortion is minimum for the proposed approach and the pansharpened images closely match the ground truth images. Colors of the objects are better preserved using the proposed approach. One can see that green color of the cir-
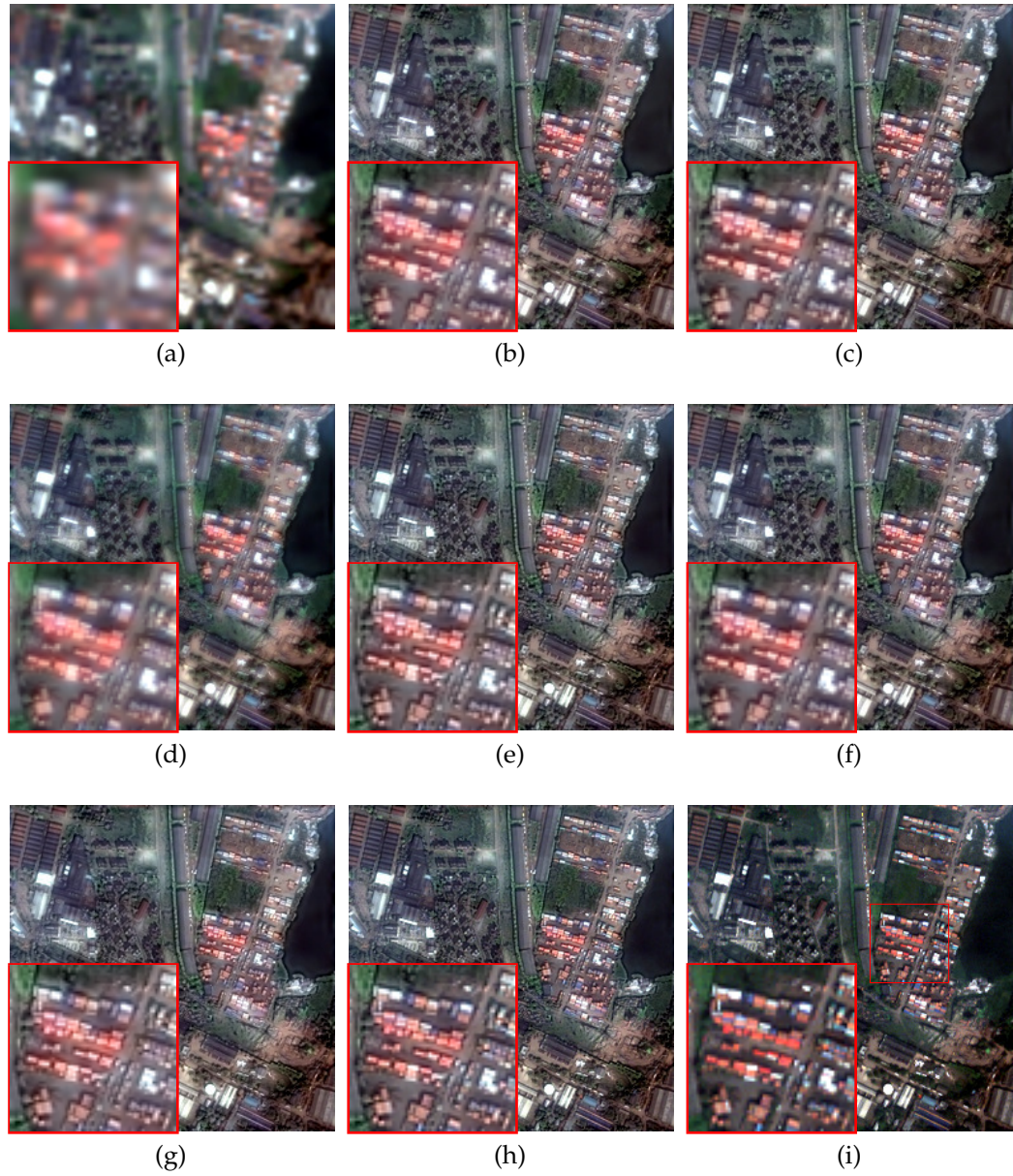
Figure 6.14: RGB true-color composition 3, 2 and 1 of pansharpening results obtained from degraded IKONOS dataset images. (a) EXP (b) BDSD (c) GSA (d) PRACS (e) AWLP (f) GLP-CBD (g) NSCT (h) Proposed (i) GT.
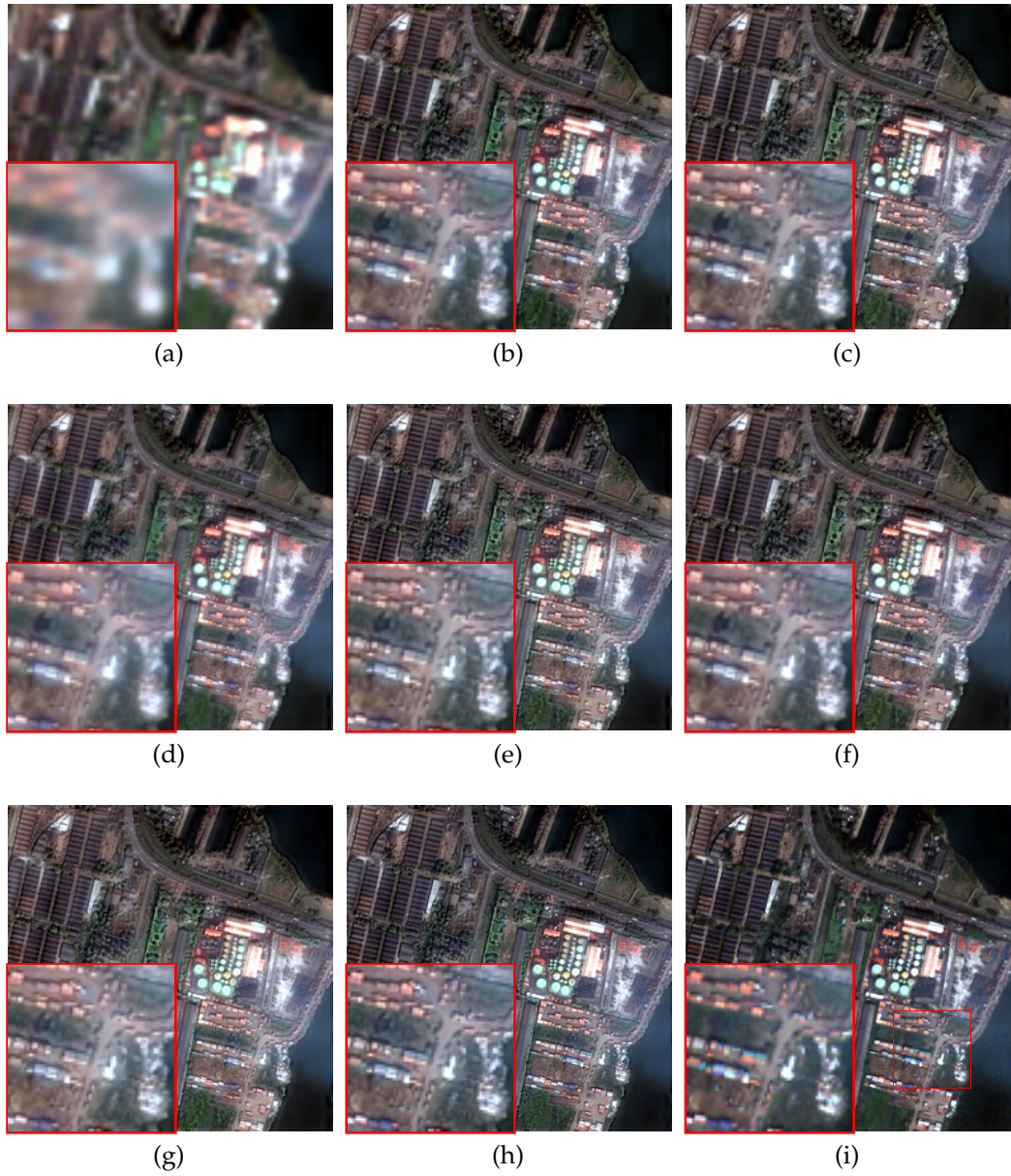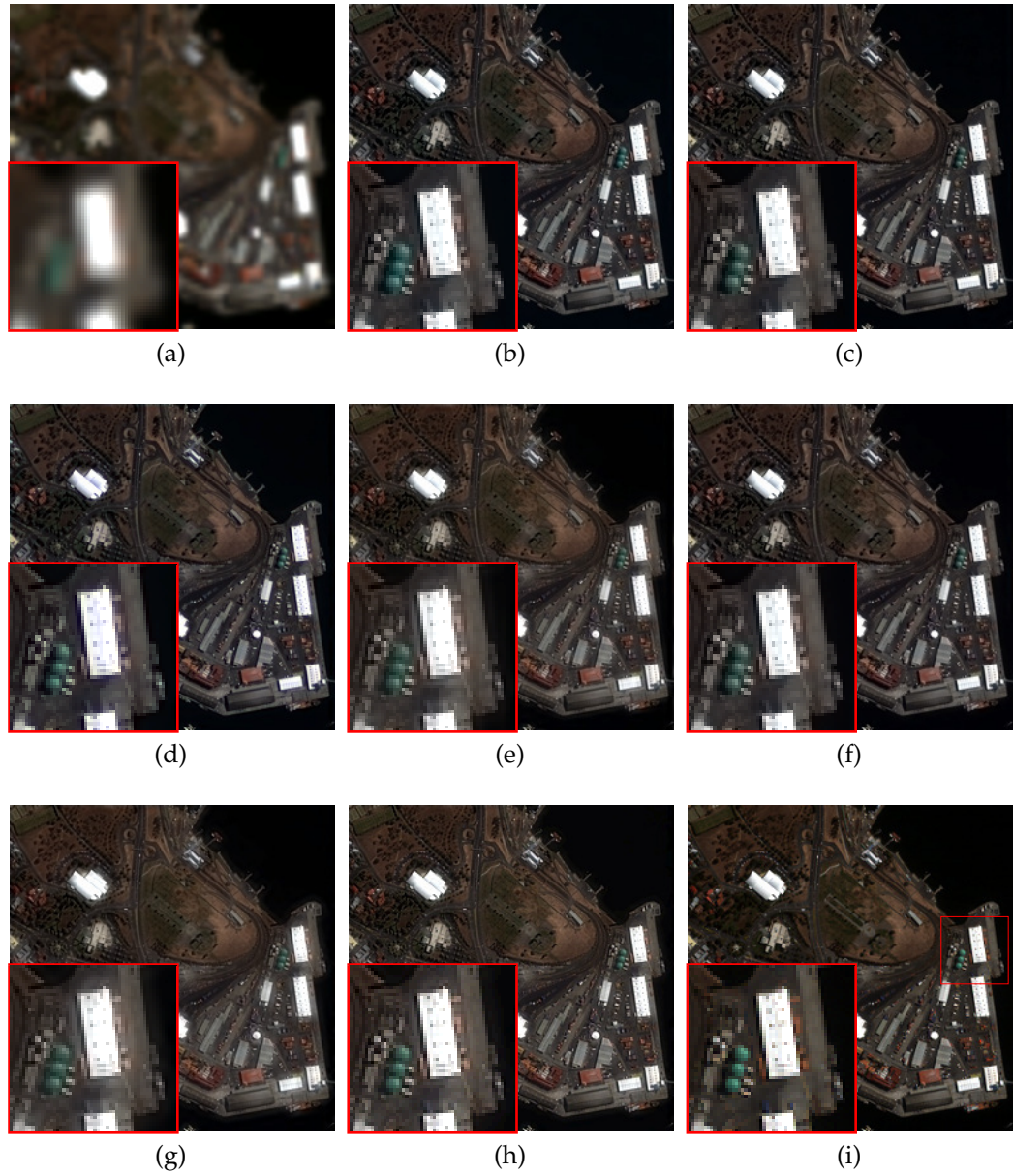
Figure 6.15: RGB true-color composition 3, 2 and 1 of pansharpening results obtained from degraded IKONOS dataset images. (a) EXP (b) BDSD (c) GSA (d) PRACS (e) AWLP (f) GLP-CBD (g) NSCT (h) Proposed (i) GT.
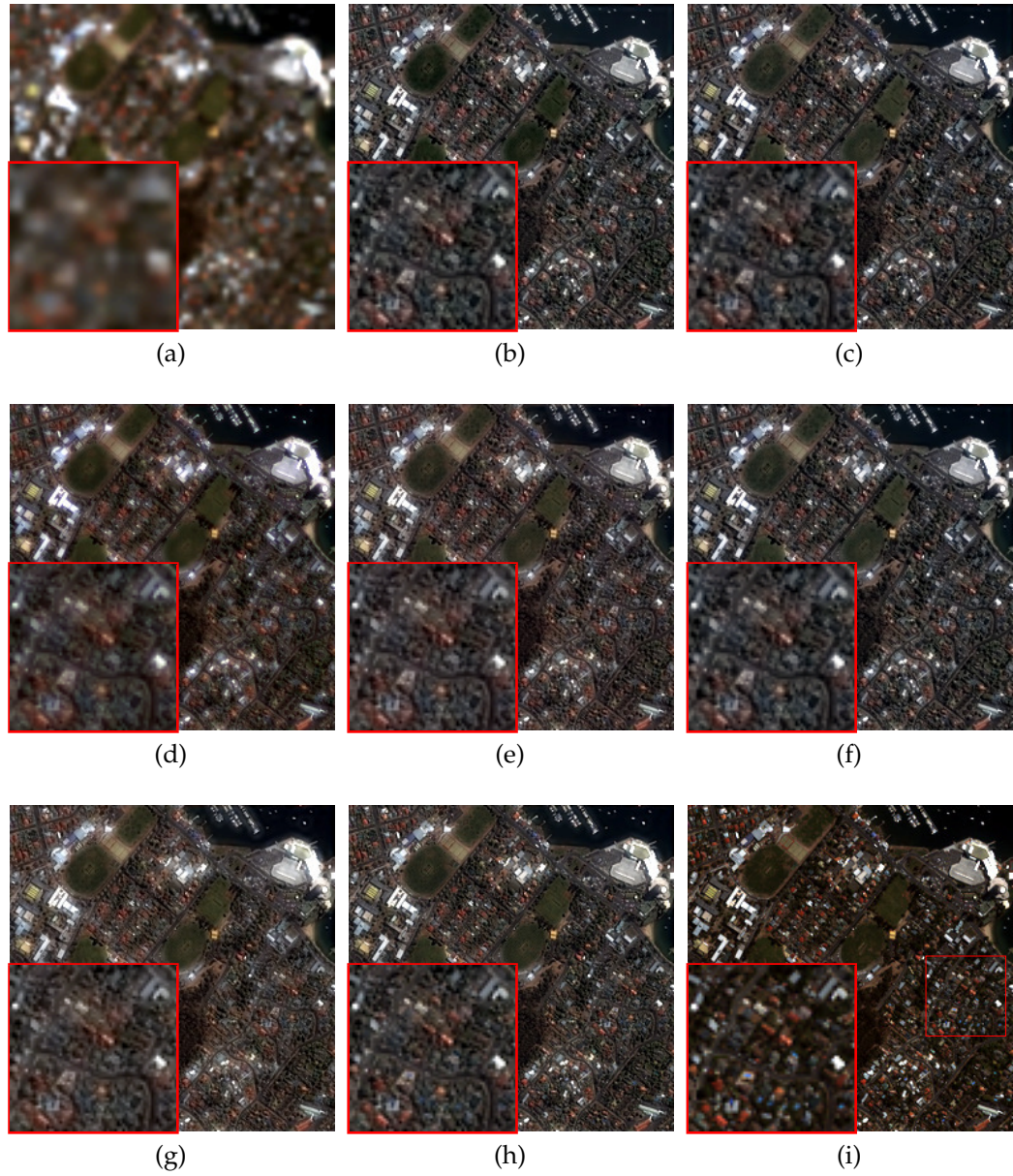
Table 6.2: Quantitative measures for the pansharpening results shown on IKONOS-2 dataset.

FIGURE	METHOD	CC				SAM	ERGAS	Q4	Q_{avg}	SCC	FSIM			
		B	G	R	NIR						B	G	R	NIR
	IDEAL	1	1	1	1	0	0	1	1	1	1	1	1	1
	EXP	0.8017	0.7917	0.7822	0.7668	5.4836	6.4824	0.5769	0.5769	0.5254	0.7515	0.7014	0.6850	0.6072
	BDSD [41]	0.9276	0.9415	0.9479	0.9226	5.3543	3.6349	0.8934	0.8920	0.8702	0.9136	0.9173	0.9285	0.8885
	GSA [6]	0.9281	0.9411	0.9479	0.9259	5.0261	3.5638	0.8892	0.8884	0.8725	0.9130	0.9170	0.9278	0.8981
Fig. 6.14	PRACS [22]	0.9113	0.9390	0.9359	0.9077	5.1680	4.2447	0.8267	0.8258	0.8614	0.8699	0.8962	0.8788	0.8239
	AWLP [77]	0.9200	0.9318	0.9345	0.9097	5.4766	3.9475	0.8546	0.8541	0.8648	0.9064	0.9019	0.9019	0.8542
	GLP-CBD [5]	0.9292	0.9424	0.9493	0.9274	5.0283	3.5277	0.8907	0.8898	0.8741	0.9135	0.9177	0.9286	0.8996
	NSCT [23]	0.9276	0.9427	0.9414	0.9260	5.0851	3.7672	0.8702	0.8693	0.8730	0.9055	0.9127	0.8989	0.8825
	Proposed	0.9443	0.9524	0.9552	0.9380	4.4938	3.3917	0.8970	0.8970	0.8965	0.9258	0.9232	0.9254	0.9018
	IDEAL	1	1	1	1	0	0	1	1	1	1	1	1	1
	EXP	0.8861	0.8805	0.8739	0.8466	4.3962	6.9879	0.6644	0.6754	0.5622	0.7830	0.7331	0.7207	0.6786
	BDSD [41]	0.9737	0.9800	0.9819	0.9683	3.7951	3.0550	0.8830	0.9123	0.9258	0.9421	0.9473	0.9573	0.9340
	GSA [6]	0.9736	0.9798	0.9819	0.9693	3.5746	2.9963	0.8790	0.9116	0.9274	0.9439	0.9479	0.9571	0.9376
Fig. 6.15	PRACS [22]	0.9726	0.9792	0.9831	0.9684	4.0004	3.1703	0.8746	0.9092	0.9258	0.9394	0.9476	0.9564	0.9249
	AWLP [77]	0.9716	0.9757	0.9754	0.9588	3.8567	3.3884	0.8665	0.9018	0.9249	0.9440	0.9420	0.9429	0.9133
	GLP-CBD [5]	0.9745	0.9807	0.9828	0.9704	3.5660	2.9336	0.8916	0.9154	0.9290	0.9447	0.9493	0.9585	0.9390
	NSCT [23]	0.9726	0.9810	0.9792	0.9650	3.9097	3.2387	0.8875	0.9091	0.9260	0.9407	0.9493	0.9425	0.9156
	Proposed	0.9793	0.9830	0.9838	0.9727	3.2950	2.9071	0.9030	0.9254	0.9407	0.9537	0.9534	0.9576	0.9388

cular structures visible in the magnified region of GT MS image shown in Fig. 6.14(i) is better preserved using proposed approach shown in Fig. 6.14(h) when compared to other approaches. Similarly red color of the tiny rectangular objects in Fig. 6.15(i) appear visually better in Fig. 6.15(h) than those in other methods which is clearly visible by observing the magnified regions. Though the CS-based approaches BDSD and GSA provide visually pleasant results with better spatial quality, spectral distortion can be seen in these approaches. MRA-based approaches perform reasonably well in terms of spatial as well as spectral quality than CS-based approaches. Using proposed approach, pansharpened images have spatial quality of the Pan image as well as spectrally they are more closer to the ground truth images.

Table 6.2 shows the quantitative comparisons for the results shown in Fig. 6.14 and Fig. 6.15. In this case also, proposed approach shows improvements in terms of band-wise and global quality measures. Values of spectral measures CC and SAM are closer to the ideal justifying better visual quality of the proposed approach. Improvements in spatial quality measures SCC and FSIM can also be observed which indicate that the spatial content of various regions is better preserved in the pansharpened output using the proposed approach. As far as the other quality measures Q4 and Q_{avg} are considered, the performance of our method is comparable to BDSD, GSA, GLP-CBD showing better spectral and

spatial quality of the pansharpened outputs.

6.4.3 Computational time

Finally, we discuss the computational time required for each method. Component substitution based methods namely BDSD, GSA, PRACS have faster execution and require less time than MRA-based approaches i.e., AWLP, GLP-CBD, NSCT and proposed approach. Among the MRA-based approaches, AWLP requires less computational time followed by GLP-CBD method. NSCT and the proposed approach require slightly high computational time because of their locally adaptive detail injection schemes processing higher number of directional subbands. Proposed approach however takes extra time than NSCT due dominant direction estimation stage which is common for any adaptive transform. However, this time is not very high and is in terms of few seconds.

6.5 Conclusion

In this chapter, we have proposed a simple yet effective multiresolution DFB design that represents the dominant directions present in the input image adaptively. Efficacy of the proposed design is tested for the pansharpening application where directional details of the PAN image are injected into the resampled MS bands using adaptive detail injection scheme. Due to better approximation power of the lowpass filter in our approach, multispectral information in the original MS bands is better preserved in the pansharpened outputs while adaptive processing of directional information adds meaningful sharpness in the spatial details. The experiments validate the use of proposed transform-based approach for pansharpening. Proposed approach maintains good trade-off between spatial and spectral quality of the pansharpened images. It can be concluded that the high approximation power and dominant directional selectivity of the proposed transform provides better fusion of Pan and MS images.

Conclusions and Future Research Directions

7.1 Summary

In this thesis, we have proposed the designs and applications of new real and complex-valued transforms having multiple directional selectivity. The main contributions of the thesis are summarized below.

- We presented designs for three real-valued transforms having higher directionality by using additional filter bank stages in conjunction with the traditional decimated and undecimated wavelet transforms. All three designs showed better adaptability to the oriented features in the input image for noise removal application based on simple thresholding approach. Application of the proposed transform having smaller redundancy with an established wavelet-based image denoising algorithm showed better performance for textural images with much less computational cost.

- Two nonsubsampled transforms belonging to a class of multiresolution directional filter banks were proposed using completely nonseparable filtering based approach. The proposed designs having simple structure and nonuniform frequency partitions offered reduced computational requirements than the nonsubsampled counterparts obtained using their original subsampled approaches. Proposed designs showed usefulness for the image denoising application due to their complete shift-invariant nature and better approximation of the directional features provided by their anisotropic directional bases.

- A well known complex-valued image representation namely dual-tree complex wavelet transform (DTCWT) was discussed with the contribution to its 1-D filter design aspect. We proposed two new approaches to design a set of biorthogonal wavelet filters of DTCWT having near-orthogonal filter response characteristics. These newly found sets of 1-D filters having symmetric wavelet bases are useful to get almost tight-frame DTCWT. The proposed approaches are based on optimization of free variables obtained through factorization of generalized halfband polynomial. Use of unconstrained optimization make these approaches simple and computationally less taxing. Associated wavelets of the filters obtained using the proposed approaches showed better analytic properties leading to improved shift invariance. We also verified improvements in the directional feature selection offered by near-symmetry of the designed wavelets using image denoising.

- We presented a 2-D complex wavelet transform having better directionality and less redundancy than the 2-D DTCWT. The extrafine directionality of the proposed transform is achieved by filtering the real-valued subbands of the finer directional wavelet transform using novel complex-valued filter bank stages. Proposed complex wavelet transform design has one lowpass and twelve directional subband representation with improved shift-invariance property. Its undecimated counterpart was also discussed. We indicated tractability of the proposed transforms for their possible separable implementations. We also showed their efficacy for image denoising using simple subband thresholding scheme.

- We proposed a simple yet effective multiresolution DFB design that represents the dominant directions present in the input image adaptively. Performance of the proposed design in this case was tested for pansharpening. Due to better approximation power of the lowpass filter in our approach, spectral information in the original MS bands is better preserved in the pansharpened output while adaptive processing of directional information adds sharpness in the spatial details. The experiments validated the use of proposed transform-based approach for pansharpening.

7.2 Future Work

In this thesis, we have proposed the transform designs using the concepts of wavelets and filter banks with the aim of having improved directional image representation. The presented works pave some new ways for further improvements and future directions such as:

- Multidimensional extensions of the proposed transforms such as RFiDWT, EFiCDWT having smaller redundancy can provide effective representation to handle the multidimensional data such as color images in a better way.

- Efficient realizations of the nonseparable filters such as ladder/lifting can help to reduce the computational complexity of the proposed transforms.

- Most of the techniques used to design DTCWT filters give irrational coefficients due to various constraints. However, having rational coefficients helps in reducing computational cost. Hence, a new optimization approach for factorization with rational coefficients is an interesting issue. Also, studying the effect of rational coefficients on the analyticity and performance of applications can be of great importance.

- Finding the accurate statistical models for the coefficients of the proposed real and complex-valued transforms can be useful for image denoising.

- Performance of the proposed transforms can be tested for various applications such as texture analysis, super-resolution, image restoration etc.

References

[1] IKONOS satellite imagery. http://www.isprs.org/data/ikonos_hobart/default.aspx. Accessed: 2014-10-05.

[2] QuickBird satellite imagery. http://www.digitalglobe.com/product-samples. Accessed: 2014-10-05.

[3] A. Abbas and T. D. Tran. Rational coefficient dual-tree complex wavelet transform: Design and implementation. *IEEE Transactions on Signal Processing*, 56(8):3523–3534, 2008.

[4] B. Aiazzi, L. Alparone, S. Baronti, and A. Garzelli. Context driven fusion of high spatial and spectral resolution images based on oversampled multiresolution analysis. *IEEE Trans. Geosci. Remote Sens.*, 40(10):2300–2312, Oct. 2002.

[5] B. Aiazzi, L. Alparone, S. Baronti, A. Garzelli, and M. Selva. MTF-tailored multiscale fusion of high-resolution MS and Pan imagery. *Photogramm. Eng. Remote Sens.*, 72(5):591–596, 2006.

[6] B. Aiazzi, S. Baronti, and M. Selva. Improving component substitution pan-sharpening through multivariate regression of MS+ Pan data. *IEEE Trans. Geosci. Remote Sens.*, 45(10):3230–3239, 2007.

[7] L. Alparone, S. Baronti, A. Garzelli, and F. Nencini. A global quality measurement of pan-sharpened multispectral imagery. *IEEE Geosci. Remote Sens. Lett.*, 1(4):313–317, 2004.

[8] I. Amro, J. Mateos, M. Vega, R. Molina, and A. K. Katsaggelos. A survey

of classical methods and new trends in pansharpening of multispectral images. *EURASIP J. Adv. Sig. Proc.*, 2011:79, 2011.

[9] N. Anantrasirichai, A. Achim, N. G. Kingsbury, and D. R. Bull. Atmospheric turbulence mitigation using complex wavelet-based fusion. *IEEE Trans. Image Process.*, 22(6):2398–2408, 2013.

[10] R. Ansari. Hdtv coding using a nonrectangular subband decomposition. In *Visual Communications and Image Processing'88: Third in a Series*, volume 1001, 1988.

[11] R. Ansari, A. E. Cetin, and S. H. Lee. Sub-band coding of images using nonrectangular filter banks. In *Applications of Digital Image Processing XI*, volume 974, pages 315–324. International Society for Optics and Photonics, 1988.

[12] R. Ansari, C. W. Kim, and M. Dedovic. Structure and design of two-channel filter banks derived from a triplet of halfband filters. *IEEE Transactions on Circuits and Systems II: Analog and Digital Signal Processing*, 46(12):1487–1496, 1999.

[13] M. Asikuzzaman, M. J. Alam, A. J. Lambert, and M. R. Pickering. Robust DT-CWT based DIBR 3D video watermarking using chrominance embedding. *IEEE Trans. Multimedia*, 18(9):1733–1748, 2016.

[14] R. H. Bamberger and M. J. T. Smith. A filter bank for the directional decomposition of images: Theory and design. *IEEE Trans. on Signal Process.*, 40(4):882–893, 1992.

[15] I. Bayram and I. W. Selesnick. On the dual-tree complex wavelet packet and M-band transforms. *IEEE Trans. Signal Process.*, 56(6):2298–2310, 2008.

[16] C. Bernard. *Wavelets and ill posed problems: optic flow and scattered data interpolation*. PhD thesis, ÉCOLE POLYTECHNIQUE, 1999.

[17] G. Bhatnagar, Q. Wu, and Z. Liu. Directive contrast based multimodal medical image fusion in NSCT domain. *IEEE Trans. Multimedia*, 15(5):1014–1024, 2013.

[18] C. S. Burrus. Bases, orthogonal bases, biorthogonal bases, frames, tight frames, and unconditional bases. https://cnx.org/contents/Es1rEfS5@4/Bases-Orthogonal-Bases-Biortho. Accessed: 2017-04-24.

[19] C.-L. Chang and B. Girod. Direction-adaptive discrete wavelet transform for image compression. *IEEE Trans. Image Process.*, 16(5):1289–1302, 2007.

[20] C. Chaux, L. Duval, and J. Pesquet. Image analysis using a dual-tree M-band wavelet transform. *IEEE Trans. on Image Process.*, 15(8):2397–2412, 2006.

[21] C. Chaux, J.-C. Pesquet, and L. Duval. 2D dual-tree complex biorthogonal M-band wavelet transform. In *2007 IEEE International Conference on Acoustics, Speech and Signal Processing-ICASSP'07*, volume 3, pages III–845. IEEE, 2007.

[22] J. Choi, K. Yu, and Y. Kim. A new adaptive component-substitution based satellite image fusion by using partial replacement. *IEEE Trans. Geosci. Remote Sens.*, 49(1):295–309, 2011.

[23] A. L. Da Cunha, J. Zhou, and M. N. Do. The nonsubsampled contourlet transform: theory, design, and applications. *IEEE Trans. on Image Process.*, 15(10):3089–3101, 2006.

[24] W. Daiwei and X. Zhang. A new class of Hilbert pairs of almost symmetric orthogonal wavelet bases. *IEICE TRANSACTIONS on Fundamentals of Electronics, Communications and Computer Sciences*, 99(5):884–891, 2016.

[25] S. Das and M. K. Kundu. A neuro-fuzzy approach for medical image fusion. *IEEE Trans. Biomed. Eng.*, 60(12):3347–3353, 2013.

[26] I. Daubechies et al. *Ten lectures on wavelets*, volume 61. SIAM, 1992.

[27] W. Ding, F. Wu, X. Wu, S. Li, and H. Li. Adaptive directional lifting-based wavelet transform for image coding. *IEEE Trans. on Image Process.*, 16(2):416–427, 2007.

[28] M. N. Do and Y. M. Lu. Multidimensional filter banks and multiscale geometric representations. *Foundations and Trends in Signal Processing*, 5(3):157–264, 2012.

[29] M. N. Do and M. Vetterli. The contourlet transform: an efficient directional multiresolution image representation. *IEEE Trans. on Image Process.*, 14(12):2091–2106, 2005.

[30] D. L. Donoho and I. M. Johnstone. Ideal spatial adaptation by wavelet shrinkage. *Biometrica*, 81(3):425–455, Aug. 1994.

[31] B. Dumitrescu, I. W. Selesnick, et al. Optimization of symmetric self-Hilbertian filters for the dual-tree complex wavelet transform. *IEEE Signal Processing Letters*, 15:146–149, 2008.

[32] G. Easley, D. Labate, and W.-Q. Lim. Sparse directional image representations using the discrete shearlet transform. *Appl. and Comput. Harm. Ana.*, 25(1):25–46, 2008.

[33] R. Eslami and H. Radha. New image transforms using hybrid wavelets and directional filter banks: analysis and design. In *IEEE Int. Conf. on Image Process., ICIP 2005.*, volume 1, pages I–733.

[34] R. Eslami and H. Radha. A new family of nonredundant transforms using hybrid wavelets and directional filter banks. *IEEE Trans. on Image Process.*, 16(4):1152–1167, 2007.

[35] X. Feng and P. Milanfar. Multiscale principal components analysis for image local orientation estimation. In *36th Asilomar Conf. on Signals, Systems and Computers,*, Pacific Grove, CA, Nov. 2002.

[36] F. C. Fernandes, I. W. Selesnick, R. L. Van Spaendonck, and C. S. Burrus. Complex wavelet transforms with allpass filters. *Signal Processing*, 83(8):1689–1706, 2003.

[37] F. C. Fernandes, R. L. van Spaendonck, and C. S. Burrus. A new framework for complex wavelet transforms. *IEEE Trans. on Signal Process.*, 51(7):1825–1837, 2003.

[38] F. C. Fernandes, R. L. van Spaendonck, and C. S. Burrus. Multidimensional, mapping-based complex wavelet transforms. *IEEE Trans. on Image Process.*, 14(1):110–124, 2005.

[39] M. Fierro, H.-G. Ha, and Y.-H. Ha. Noise reduction based on partial-reference, dual-tree complex wavelet transform shrinkage. *IEEE Trans. on Image Process.*, 22(5):1859–1872, 2013.

[40] A. Garzelli and F. Nencini. Interband structure modeling for pan-sharpening of very high-resolution multispectral images. *Inf. Fusion*, 6(3):213–224, 2005.

[41] A. Garzelli, F. Nencini, and L. Capobianco. Optimal MMSE pan sharpening of very high resolution multispectral images. *IEEE Trans. Geosci. Remote Sens.*, 46(1):228–236, 2008.

[42] O. N. Gerek and A. E. Cetin. A 2-d orientation-adaptive prediction filter in lifting structures for image coding. *IEEE Trans. Image Process.*, 15(1):106–111, 2006.

[43] R. A. Gopinath. The phaselet transform-an integral redundancy nearly shift-invariant wavelet transform. *IEEE Trans. Signal Process.*, 51(7):1792–1805, 2003.

[44] N. M. Grzywacz and D. K. Merwine. Directional selectivity. *The Handbook of Brain Theory and Neural Networks*, pages 353–358, 2003.

[45] C. Guillemot, A. E. Cetin, and R. Ansari. M-channel nonrectangular wavelet representation for 2-d signals: basis for quincunx sampled signals. In *International Conference on Acoustics, Speech, and Signal Processing*, pages 2813–2816. IEEE, 1991.

[46] H. Guo, J. E. Odegard, M. Lang, R. A. Gopinath, I. W. Selesnick, and C. S. Burrus. Wavelet based speckle reduction with application to sar based atd/r. In *ICIP*, volume 1, pages 75–79. IEEE, 1994.

[47] B. Hou, X. Zhang, X. Bu, and H. Feng. SAR image despeckling based on nonsubsampled shearlet transform. *IEEE Journal of Selected Topics in Applied Earth Observations and Remote Sensing*, 5(3):809–823, 2012.

[48] M. Z. Iqbal, A. Ghafoor, and A. M. Siddiqui. Satellite image resolution enhancement using dual-tree complex wavelet transform and nonlocal means. *IEEE Geosci. and Remote Sensing Lett.*, 10(3):451–455, 2013.

[49] L. Jacques, L. Duval, C. Chaux, and G. Peyré. A panorama on multiscale geometric representations, intertwining spatial, directional and frequency selectivity. *Signal Processing*, 91(12):2699–2730, 2011.

[50] C. W. Kim and R. Ansari. Subband decomposition procedure for quincunx sampling grids. In *Visual Communications and Image Processing'91: Visual Communications Part 2 (of 2)*. Publ by Int. Soc. for Optical Engineering, 1991.

[51] N. Kingsbury. Image processing with complex wavelets. *Philosophical Transactions of the Royal Society of London A: Mathematical, Physical and Engineering Sciences*, 357(1760):2543–2560, 1999.

[52] N. Kingsbury. A dual-tree complex wavelet transform with improved orthogonality and symmetry properties. In *ICIP*, volume 2, pages 375–378. IEEE, 2000.

[53] N. Kingsbury. Complex wavelets for shift invariant analysis and filtering of signals. *Appl. Comput. Harmon. Anal*, 10(3):234–253, 2001.

[54] N. Kingsbury. Design of Q-shift complex wavelets for image processing using frequency domain energy minimization. In *ICIP*, volume 1, pages 1010–1013. IEEE, 2003.

[55] F. Kruse, A. Lefkoff, J. Boardman, K. Heidebrecht, A. Shapiro, P. Barloon, and A. Goetz. The spectral image processing system (SIPS):interactive visualization and analysis of imaging spectrometer data. *Remote Sens. Environ.*, 44(2):145–163, 1993.

[56] M. Lang. Optimal weighted phase equalization according to the L_∞-norm. *Signal Processing*, 27(1):87–98, 1992.

[57] F. Laporterie-Déjean, H. de Boissezon, G. Flouzat, and M.-J. Lefèvre-Fonollosa. Thematic and statistical evaluations of five panchromatic/multispectral fusion methods on simulated PLEIADES-HR images. *Inf. Fusion*, 6(3):193–212, 2005.

[58] D. Le Gall and A. Tabatabai. Sub-band coding of digital images using symmetric short kernel filters and arithmetic coding technique. In *ICASSP*, pages 761–765. IEEE, 1988.

[59] H. Li, B. Manjunath, and S. K. Mitra. Multi-sensor image fusion using the wavelet transform. In *ICIP*, volume 1, pages 51–55. IEEE, 1994.

[60] S. Li, L. Fang, and H. Yin. Multitemporal image change detection using a detail-enhancing approach with nonsubsampled contourlet transform. *IEEE Geosci. and Remote Sensing Lett.*, 9(5):836–840, 2012.

[61] L. Liang, G. Shi, and X. Xie. Nonuniform directional filter banks with arbitrary frequency partitioning. *IEEE Trans. on Image Process.*, 20(1):283–288, 2011.

[62] M. Lightstone, E. Majani, and S. K. Mitra. Low bit-rate design considerations for wavelet-based image coding. *Multidimensional systems and signal processing*, 8(1-2):111–128, 1997.

[63] Y. M. Lu and M. N. Do. The finer directional wavelet transform. In *Proc. IEEE Int. Conf. Acoust. Speech and Signal Proc.*, 2005.

[64] Y. M. Lu and M. N. Do. Multidimensional directional filter banks and surfacelets. *IEEE Trans. on Image Process.*, 16(4):918–931, 2007.

[65] Y. M. Lu and M. N. Do. A mapping-based design for nonsubsampled hourglass filter banks in arbitrary dimensions. *IEEE Trans. on Signal Process.*, 56(4):1466–1478, 2008.

[66] J. Magarey and N. Kingsbury. Motion estimation using a complex-valued wavelet transform. *IEEE Trans. on Signal Process.*, 46(4):1069–1084, 1998.

[67] S. Mallat. *A Wavelet Tour of Signal Processing*. Academic Press, San Diego CA, *3rd* edition, 2009.

[68] S. Murugesan and D. B. Tay. A new class of almost symmetric orthogonal Hilbert pair of wavelets. *Signal Processing*, 95:76–87, 2014.

[69] S. Murugesan and D. B. H. Tay. On the aliasing effect of the finer directional wavelet transform. In *Proc. IEEE Int. Symp. Circuits and Syst.*, pages 2345–2348, 2012.

[70] F. Nencini, A. Garzelli, S. Baronti, and L. Alparone. Remote sensing image fusion using the curvelet transform. *Inf. Fusion*, 8(2):143–156, 2007.

[71] T. T. Nguyen and S. Oraintara. Multiresolution direction filterbanks: theory, design, and applications. *IEEE Trans. on Signal Process.*, 53(10):3895–3905, 2005.

[72] T. T. Nguyen and S. Oraintara. A class of multiresolution directional filter banks. *IEEE Trans. on Signal Process.*, 55(3):949–961, 2007.

[73] T. T. Nguyen and S. Oraintara. The shiftable complex directional pyramid–Part I: theoretical aspects. *IEEE Trans. on Signal Process.*, 56(10):4651–4660, 2008.

[74] T. T. Nguyen and S. Oraintara. The shiftable complex directional pyramid–Part II: Implementation and applications. *IEEE Trans. on Signal Process.*, 56(10):4661–4672, 2008.

[75] S. Nikolov, D. Bull, C. Canagarajah, M. Halliwell, and P. Wells. Image fusion using a 3-d wavelet transform. 1999.

[76] A. V. Oppenheim and R. W. Schafer. *Discrete-time signal processing*. Pearson Higher Education, 2010.

[77] X. Otazu, M. Gonzalez-Audicana, O. Fors, and J. Nunez. Introduction of sensor spectral response into image fusion methods. application to wavelet-based methods. *IEEE Trans. Geosci. Remote Sens.*, 43(10):2376–2385, 2005.

[78] B. D. Patil, P. G. Patwardhan, and V. M. Gadre. On the design of FIR wavelet filter banks using factorization of a halfband polynomial. *IEEE Signal Process. Letters*, 15:485–488, 2008.

[79] G. Peyré. A review of adaptive image representations. *IEEE J. Sel. Topics Signal Process.*, 5(5):896–911, 2011.

[80] J. Portilla and E. P. Simoncelli. A parametric texture model based on joint statistics of complex wavelet coefficients. *Int. J. Comput. Vis.*, 40(1):49–70, 2000.

[81] J. Portilla, V. Strela, M. J. Wainwright, and E. P. Simoncelli. Image denoising using scale mixtures of Gaussians in the wavelet domain. *IEEE Trans. on Image Process.*, 12(11):1338–1351, 2003.

[82] P. S. Pradhan, R. L. King, N. H. Younan, and D. W. Holcomb. Estimation of the number of decomposition levels for a wavelet-based multiresolution multisensor image fusion. *IEEE Trans. Geosci. Remote Sens.*, 44(12):3674–3686, 2006.

[83] H. Rabbani and S. Gazor. Video denoising in three-dimensional complex wavelet domain using a doubly stochastic modelling. *IET Image Process.*, 6(9):1262–1274, 2012.

[84] A. D. Rahulkar, B. D. Patil, and R. S. Holambe. A new approach to the design of biorthogonal triplet half-band filter banks using generalized half-band polynomials. *Signal, Image and Video Processing*, 8(8):1451–1457, 2014.

[85] Y. Rakvongthai, A. Vo, and S. Oraintara. Complex Gaussian scale mixtures of complex wavelet coefficients. *IEEE Trans. on Signal Process.*, 58(7):3545–3556, 2010.

[86] T. Ranchin, B. Aiazzi, L. Alparone, S. Baronti, and L. Wald. Image fusion - the ARSIS concept and some successful implementation schemes. *ISPRS J. Photogramm. Remote Sens.*, 58(1-2):4–18, Jun. 2003.

[87] M. P. Sampat, Z. Wang, S. Gupta, A. C. Bovik, and M. K. Markey. Complex wavelet structural similarity: A new image similarity index. *IEEE Trans. on Image Process.*, 18(11):2385–2401, 2009.

[88] R. A. Schowengerdt. *Remote sensing: models and methods for image processing*. Academic press, 2006.

[89] I. W. Selesnick. http://eeweb.poly.edu/iselesni/WaveletSoftware/. Accessed: 2014-04-08.

[90] I. W. Selesnick. Hilbert transform pairs of wavelet bases. *IEEE Signal Process. Letters*, 8(6):170–173, 2001.

[91] I. W. Selesnick. The design of approximate Hilbert transform pairs of wavelet bases. *IEEE Trans. Signal Process.*, 50(5):1144–1152, 2002.

[92] I. W. Selesnick, R. G. Baraniuk, and N. C. Kingsbury. The dual-tree complex wavelet transform. *IEEE Signal Process. Magazine*, 22(6):123–151, 2005.

[93] G. Shi, L. Liang, and X. Xie. Design of directional filter banks with arbitrary number of subbands. *IEEE Trans. on Signal Process.*, 57(12):4936–4941, 2009.

[94] H. Shi, B. Hu, and J. Q. Zhang. A novel scheme for the design of approximate Hilbert transform pairs of orthonormal wavelet bases. *IEEE Transactions on Signal Processing*, 56(6):2289–2297, 2008.

[95] H. Shi and S. Luo. A new scheme for the design of Hilbert transform pairs of biorthogonal wavelet bases. *EURASIP Journal Adv. in Signal Process.*, 2010:98, 2010.

[96] Y. Shi, X. Yang, and Y. Guo. Translation invariant directional framelet transform combined with Gabor filters for image denoising. *IEEE Trans. Image Process.*, 23(1):44–55, Jan. 2014.

[97] J.-L. Starck, J. Fadili, and F. Murtagh. The undecimated wavelet decomposition and its reconstruction. *IEEE Trans. on Image Process.*, 16(2):297–309, 2007.

[98] G. Strang and T. Nguyen. *Wavelets and Filter Banks*. Cambridge, MA: Wellesly-Cambridge Press, 1996.

[99] W. Sweldens. The lifting scheme: A custom-design construction of biorthogonal wavelets. *Appl. Comput. Harm. Ana.*, 3(2):186–200, 1996.

[100] Y. Tanaka, M. Hasegawa, S. Kato, M. Ikehara, and T. Q. Nguyen. Adaptive directional wavelet transform based on directional prefiltering. *IEEE Trans. Image Process.*, 19(4):934–945, 2010.

[101] D. Taubman. Adaptive, non-separable lifting transforms for image compression. In *ICIP*, volume 3, pages 772–776. IEEE, 1999.

[102] D. B. Tay. ETHFB: a new class of even-length wavelet filters for Hilbert pair design. In *2006 IEEE International Symposium on Circuits and Systems*, pages 4–pp. IEEE, 2006.

[103] D. B. Tay. A new approach to the common-factor design technique for Hilbert-pair of wavelets. *IEEE Signal Processing Letters*, 17(11):969–972, 2010.

[104] D. B. Tay. Direct design of phase factor in the common-factor technique for Hilbert-pairs. In *2011 IEEE International Symposium of Circuits and Systems (ISCAS)*, pages 1760–1763. IEEE, 2011.

[105] D. B. Tay. Symmetric self-Hilbertian filters via extended zero-pinning. *Signal Processing*, 92(2):392–400, 2012.

[106] D. B. Tay, N. G. Kingsbury, and M. Palaniswami. Orthonormal Hilbert-pair of wavelets with (almost) maximum vanishing moments. *IEEE Signal Processing Letters*, 13(9):533–536, 2006.

[107] D. B. Tay and S. Murugesan. A class of rational coefficients biorthogonal Hilbert-pairs. *International Journal of Circuit Theory and Applications*, 43(7):887–899, 2015.

[108] D. B. H. Tay. Rationalizing the coeffcients of popular biorthogonal wavelet filters. *IEEE Transactions on Circuits, Syst. Video Technol.*, 10(6):998–1004, 2000.

[109] D. B. H. Tay. Designing Hilbert-pair of wavelets: recent progress and future trends. In *6th International Conf. on Inform., Commun. & Signal Process.*, pages 1–5. IEEE, 2007.

[110] D. B. H. Tay. ETHFB: a new class of even-length biorthogonal wavelet filters for Hilbert pair design. *IEEE Trans. Circuits Syst. I*, 55(6):1580–1588, 2008.

[111] D. B. H. Tay and N. G. Kingsbury. Flexible design of multidimensional perfect reconstruction FIR 2-band filters using transformations of variables. *IEEE Trans. on Image Proces.*, 2(4):466–480, 1993.

[112] J.-P. Thiran. Recursive digital filters with maximally flat group delay. *IEEE Transactions on Circuit Theory*, 18(6):659–664, 1971.

[113] C. Thomas, T. Ranchin, L. Wald, and J. Chanussot. Synthesis of multispectral images to high spatial resolution: A critical review of fusion methods based on remote sensing physics. *IEEE Trans. Geosci. Sens.*, 46(5):1301–1312, 2008.

[114] M. Unser. Approximation power of biorthogonal wavelet expansions. *IEEE Trans. Signal Process.*, 44(3):519–527, 1996.

[115] P. P. Vaidyanathan. *Multirate systems and filter banks*. Pearson Education, 1993.

[116] D. I. Vaney, B. Sivyer, and W. R. Taylor. Direction selectivity in the retina: symmetry and asymmetry in structure and function. *Nature Reviews Neuroscience*, 13(3):194–208, 2012.

[117] M. Vetterli. Filter banks allowing perfect reconstruction. *Signal Processing*, 10(3):219–244, 1986.

[118] M. Vetterli and J. Kovacevic. *Wavelets and Subband Coding*. Englewood Cliffs Prentice-Hall, 1995.

[119] M. Vetterli, J. Kovačević, and D. J. Legall. Perfect reconstruction filter banks for hdtv representation and coding. *Signal Processing: Image Communication*, 2(3):349–363, 1990.

[120] M. Vetterli and D. Le Gall. Perfect reconstruction FIR filter banks: Some properties and factorization. *IEEE Transactions on Acoustics, Speech and Signal Processing*, 37(7):1057–1071, 1989.

[121] G. Vivone, L. Alparone, J. Chanussot, M. Dalla Mura, A. Garzelli, G. Licciardi, R. Restaino, and L. Wald. A critical comparison among pansharpening algorithms. *IEEE Trans. Geosci. Remote Sens.*, 53(5):2565–2586, 2015.

[122] A. Vo and S. Oraintara. Using phase and magnitude information of the complex directional filter bank for texture segmentation. In *16th European Signal Processing Conference*. IEEE, 2008.

[123] A. P. Vo, S. Oraintara, and T. T. Nguyen. Using phase and magnitude information of the complex directional filter bank for texture image retrieval. In *ICIP*. IEEE, 2007.

[124] L. Wald. Quality of high resolution synthesized images: Is there a simple criterion? *Proc. Int. Conf. Fusion Earth Data*, pages 46–61, 2000.

[125] T. Wan, N. Canagarajah, and A. Achim. Segmentation-driven image fusion based on alpha-stable modeling of wavelet coefficients. *IEEE Trans. on Multimedia*, 11(4):624–633, 2009.

[126] D. Wang and X. Zhang. IIR-based DT-CWT with improved analyticity and frequency selectivity. *IEEE Trans. on Signal Process.*, 60(11):5764–5774, 2012.

[127] D.-W. Wang and X. Zhang. Hilbert pair of almost symmetric orthogonal wavelets with arbitrary center of symmetry. In *Signal and Information Processing Association Annual Summit and Conference (APSIPA), 2013 Asia-Pacific*, pages 1–8. IEEE, 2013.

[128] J. Wang and J. Q. Zhang. A globally optimal bilinear programming approach to the design of approximate Hilbert pairs of orthonormal wavelet bases. *IEEE Transactions on Signal Processing*, 58(1):233–241, 2010.

[129] X. Wang, G. Shi, Y. Niu, and L. Zhang. Robust adaptive directional lifting wavelet transform for image denoising. *IET image process.*, 5(3):249–260, 2011.

[130] Z. Wang and A. C. Bovik. A universal image quality index. *IEEE Trans. Signal Process. Lett.*, 9(3):81–84, 2002.

[131] Z. Wang, A. C. Bovik, H. R. Sheikh, and E. P. Simoncelli. Image quality assessment: From error visibility to structural similarity. *IEEE Trans. on Image Process.*, 13(4):600–612, 2004.

[132] A. Wong and J. Scharcanski. Phase-adaptive superresolution of mammographic images using complex wavelets. *IEEE Trans. on Image Process.*, 18(5):1140–1146, 2009.

[133] R. Yu and H. Ozkaramanli. Hilbert transform pairs of orthogonal wavelet bases: Necessary and sufficient conditions. *IEEE Trans. Signal Process.*, 53(12):4723–4725, 2005.

[134] R. Yu and H. Ozkaramanli. Hilbert transform pairs of biorthogonal wavelet bases. *IEEE Trans. Signal Process.*, 54(6):2119–2125, 2006.

[135] L. Zhang, L. Zhang, X. Mou, and D. Zhang. FSIM: a feature similarity index for image quality assessment. *IEEE Trans. on Image Process.*, 20(8):2378–2386, 2011.

[136] X. Zhang. Design of Hilbert transform pairs of orthonormal wavelet bases using Remez exchange algorithm. In *2009 16th IEEE International Conference on Image Processing (ICIP)*, pages 3813–3816. IEEE, 2009.

[137] X. Zhang. Design of Hilbert transform pairs of orthonormal wavelet bases with improved analyticity. In *2011 IEEE International Conference on Acoustics, Speech and Signal Processing (ICASSP)*, pages 4384–4387. IEEE, 2011.

[138] X. Zhang. Design of Q-shift filters with improved vanishing moments for DTCWT. In *2011 18th IEEE International Conference on Image Processing*, pages 253–256. IEEE, 2011.

[139] X. Zhang. A new phase-factor design method for Hilbert-pairs of orthonormal wavelets. *IEEE Signal Processing Letters*, 18(9):529–532, 2011.

[140] X. Zhang and H. Morihara. Design of Q-shift filters with flat group delay. In *2012 IEEE International Symposium on Circuits and Systems*, pages 2337–2340. IEEE, 2012.

List of Publications

Journal

- S. S. Gajbhar and M. V. Joshi, "Design of Complex Adaptive Multiresolution Directional Filter Bank and Application to Pansharpening," in *Signal, Image and Video Processing*, vol. 11, no. 2, 259–266, February 2017.

Conferences

- S. S. Gajbhar and M. V. Joshi, "Design of Biorthogonal Wavelet Filters of DTCWT using Factorization of Halfband Polynomial," in *7th National Conference on Computer Vision, Pattern Recognition, Image Processing and Graphics (NCVPRIPG 2017)*, IIT Mandi, India, Dec. 16-19, 2017.

- S. S. Gajbhar and M. V. Joshi, "Image Denoising using Tight Frame Dual Tree Complex Wavelet Transform," in *7th National Conference on Computer Vision, Pattern Recognition, Image Processing and Graphics (NCVPRIPG 2017)*, IIT Mandi, India, Dec. 22-24, 2017.

- S. S. Gajbhar and M. V. Joshi, "Design of Extrafine Complex Directional Wavelet Transform and Application to Image Denoising," in *16th International Workshop on Multimedia Signal Processing (MMSP-2014)*, Jakarta, Indonesia, Sept. 22-24, 2014.

- S. S. Gajbhar and M. V. Joshi, "Novel Designs For Nonsubsampled Multiresolution Directional Filter Banks And An Extra Finer Directional Wavelet Transform," in *2nd IEEE China Summit and International Conference on Signal*

and Information Processing (ChinaSIP'14), Xi'an, China, July, 9-13, 2014.

- S. S. Gajbhar and M. V. Joshi, "Image Denoising Using Redundant Finer Directional Wavelet Transform," in *4th National Conference on Computer Vision, Pattern Recognition, Image Processing and Graphics (NCVPRIPG 2013)*, IIT Jodhpur, India, Dec. 19-21, 2013. (**Best Paper Award**)

Achievements

- **May 2016**

  Reviewer in Signal, Image and Video Processing

  (Invited by: The Editorial Office, Signal, Image and Video Processing).

- **April–November 2014**

  Organizing Committee Member in the 3rd ACCV Workshop on e-Heritage

  (Held conjunction with the 12th Asian Conference on Computer Vision –

  ACCV 2014).

- **December 2013**

  Best Paper Award with a prize money of Rs. 10,000 for paper in the 4th

  National Conference on Computer Vision, Pattern Recognition, Image Pro-

  cessing and Graphics (NCVPRIPG 2013) held at IIT Jodhpur, India.